Technische Universität München
Max-Planck-Institut für Plasmaphysik

Statistical Properties and Structure of Turbulent Convection

Dan Škandera

Vollständiger Abdruck der von der Fakultät für Physik der Technischen Universität München zur Erlangung des akademischen Grades eines

Doktors der Naturwissenschaften

genehmigten Dissertation.

Vorsitzender:	Univ.-Prof. Dr. Rudolf Gross
Prüfer der Dissertation:	1. Hon.-Prof. Dr. Sibylle Günter
	2. Univ.-Prof. Dr. Katharina Krischer

Die Dissertation wurde am 3.4.2007 bei der Technischen Universität München eingereicht und durch die Fakultät für Physik am 18.7.2007 angenommen.

Věnováno mým nejbližším, bez jejichž lásky, pochopení, tolerance a bezmezné podpory by tato práce nemohla vzniknout.

Abstract

This thesis presents extensive numerical studies of turbulent convection. It focuses on spectral properties of convection and its nonlinear dynamics. Within the frame of the thesis, several large-scale direct numerical simulations are performed. Four particular systems are investigated and discussed in the work, namely: two- and three-dimensional hydrodynamic and magnetohydrodynamic turbulent convection. All systems are driven by a mean horizontal temperature gradient. The numerical code uses a standard pseudospectral scheme. Special attention is paid to the comparison of various phenomenological theories of turbulence and their modifications for convective flows. Structure functions, probability density functions and intermittency effects are examined in all individual systems as well. The existence of the Bolgiano-Obukhov regime of turbulence is confirmed in the two-dimensional hydrodynamic system, whereas the three-dimensional systems are found to operate in Kolmogorov-type regimes of turbulence. The two-dimensional magnetohydrodynamic turbulent convection exhibits quasi-oscillations between two different turbulent states. It is shown that the turbulent regime of two-dimensional magnetoconvection depends on the mutual alignment between velocity and magnetic field.

Contents

Introduction

Convection represents, apart from conduction and radiation, a basic mechanism of energy transport in fluids. Turbulence is a state of flow that is characterized by chaotic and irregular variations of physical quantities, e.g. velocity, in space and time. Both phenomena play a very important role in a number of physical systems. Prominent examples are the solar convection zone and the liquid outer core of the Earth. However, the fundamental role of turbulent convection can be identified in various other systems too. The Earth's atmosphere is heated up near the surface, and resulting convective motions influence its global dynamics. Different levels of salinity in oceanic water cause convective circulations as well. Observations of all these systems demonstrate an interesting feature: the presence of convection in a natural system often leads to turbulent motions. In other words, where vigorous convection takes place, turbulence can be found as well. This fundamental linkage between convection and turbulence can be traced to underlying physical reasons. Convection, being the consequence of some kind of primary instability in the system, provides a source of energy for turbulent fluctuations. The energy injected to the system leads to increased mixing rates and efficient transport of quantities advected by the flow. Convective turbulence is usually driven by a mean temperature gradient, but other driving mechanisms exist as well, e.g. gradients of chemical substances.

Most of the visible matter in the Universe is in a plasma state. Plasma can be described — under the assumptions given in section 1.1 — as an electrically conducting fluid. In this case, convection is a ubiquitous agent involved in the generation of magnetic fields. These are dynamically important for convective turbulence, and are able to change its properties by nonlinear back-reactions noticeably. A well-known example is the turbulent dynamo, i.e. the generation of a large-scale magnetic field due to the combined action of convection and rotation. In addition, the amplification of an originally small seed magnetic field, a process called small-scale dynamo, is observed in convective systems as well.

Scientific research on turbulent convection consists of three main cornerstones: theory, experiment and numerical simulation. If there is any discrepancy between them, this should be investigated further and clarified. Only if all three parts are in mutual agreement, the phenomenon is accepted as explained. First attempts to understand and describe convection were done by Bénard and Lord Rayleigh, who investigated its properties in series of experiments with water tanks that were heated from below and cooled from above ([Ray83][Ben01] [Ray16]). Lord Rayleigh introduced a nondimensional parameter that describes

the importance of buoyancy forces for the dynamics of convective flows, the Rayleigh number. From the theoretical point of view, convection was treated at first in the frame of linear perturbation analysis (e.g. [Cha61] [DR81]). The critical Rayleigh number for the onset of convective instability was determined for several basic configurations, and linear stages of the instability were analyzed. However, linear theory was unable to explain the dynamics of the nonlinearly saturated turbulent state of convection. The first phenomenological theory of turbulent convection was proposed independently by Bolgiano and Obukhov in the late 1950s ([Bol59][Obu59]). It is based on dimensional arguments developed by Kolmogorov in the context of hydrodynamic turbulence (e.g. [Fri95][Les97] [Pop00]). Although the Bolgiano-Obukhov phenomenology was originally aimed at mechanically driven turbulent convection in flows with stable stratification, it was later experimentally found that the same phenomenology applies to convectively driven systems as well (e.g. [MY75][CCI93][MTM04]). Since then, many laboratory experiments on convective turbulence have been conducted in tanks with different shapes and different aspect ratios (e.g. [CCI93][SX01]). They confirmed the validity of the Bolgiano-Obukhov predictions. The most frequently used medium in laboratory experiments is water, but sodium, gallium and mercury with various viscosity, thermal and electrical conductivity properties are often used as well (e.g. [Sig94][MTM04]). While a three-dimensional hydrodynamic Rayleigh-Bénard configuration has been studied in laboratory quite extensively, experimental investigations of quasi-two-dimensional setups or systems with conducting fluids are rare. Such configurations are difficult to prepare and control under laboratory conditions. Experimental research on convection in plasma is largely restricted to observations of extraterrestrial systems, especially the solar convection zone which is also very often investigated numerically (e.g. [PW82][SV06]). Therefore, an experimental confirmation of the Bolgiano-Obukhov phenomenology in these systems remains yet unattainable. In addition, the relation between measured frequency spectra and spatial spectra of energy has not been clarified yet. Thus the comparison between experimental results measured predominantly in the frequency space and theoretical predictions usually given in wavenumber formulation is largely limited.

Numerical simulations of convective turbulence represent a valuable tool that provides more detailed information about examined systems compared to laboratory measurements. Moreover, they permit investigations of experimentally inaccessible configurations. In spite of a number of numerical studies, the validity of the Bolgiano-Obukhov phenomenology has been confirmed only in two-dimensional hydrodynamic convection while three-dimensional systems exhibit a Kolmogorov-type turbulence (e.g. [GL93][TS94][VC03]). Thus there is evident disagreement between laboratory measurements confirming the Bolgiano-Obukhov phenomenology and numerical results indicating a Kolmogorov behavior. Moreover, many numerical investigations of turbulent convection concentrated on modeling of particular systems, e.g. the solar convection zone, and considerably less work has been done to elucidate general physical properties of turbulent convection. Therefore, despite an increasing interest in past years, only a limited progress in clarifying the inherent physics of convective turbulence has been achieved. Thus the primary object of the presented work is the investigation of fundamental properties of turbulent convection, e.g. spectral energy dynamics or universal statistical properties that should be independent

of a particular configuration and specific boundary conditions.

More recently, several additional open questions regarding various theoretical aspects of turbulent convection have appeared, especially: the importance of the direction of spectral energy transfer for the Bolgiano-Obukhov regime of turbulent convection, the existence of the Bolgiano-Obukhov regime only in two-dimensional systems, a possible presence of a mixed regime where the temperature field exhibits the Bolgiano-Obukhov behavior in a Kolmogorov-type velocity field, the role of the orientation of a mean temperature gradient, the impact of magnetic fields on the nonlinear dynamics of turbulent convection, the validity of assumptions for spectral energy transfer in the Bolgiano-Obukhov theory of turbulent convection and others.

These open questions represent an additional motivation for the investigation presented in this work. One of the goals of this project is to test these hypotheses and to clarify the aforementioned discrepancy between laboratory and numerical results. The presented work might also improve the general understanding of turbulence and the role of the natural way of driving by a mean temperature gradient, in contrast to rather artificial energy inputs often used in numerical studies of turbulence.

The thesis is organized as follows. Chapter 1 introduces basic concepts of convective turbulence and the set of dynamical equations governing the investigated systems. Chapter 2 gives a brief overview of the numerical procedure employed to solve the equation sets, including parallelization and optimization techniques used to obtain a maximal computational performance. Several numerical tests of the code are presented as well. The following chapters are devoted to the presentation and interpretation of obtained results. In chapters 3 and 4, two- and three-dimensional hydrodynamic convective systems are investigated, respectively. Chapters 5 and 6 present results obtained from two- and three-dimensional magnetoconvection. The final part summarizes the thesis, and emphasizes the most important results of this work.

Chapter 1

Fundamentals of turbulent convection

1.1 General considerations

This section introduces basic concepts of convection with the help of a simple example. Consider a tank filled with fluid that is initially at rest. The entire tank is thermally perfectly isolated from its surroundings, except at the bottom and the upper side. The bottom plate of the tank is continuously heated, and kept at high constant temperature. The upper plate is cooled permanently, and kept at low constant temperature. The temperature difference between the plates establishes a constant vertical gradient of the temperature pointing downwards. Additionally, there is the gravitational force acting on the fluid in the downward direction. Without any perturbations the fluid stays at rest with a linear vertical temperature profile. The heat is transported by molecular conduction from the hot bottom part to the cool upper part. When the power input to the tank increases due to additional heating of the bottom plate, the conductive energy transport rate increases as well, but the fluid remains at rest. However, since the mean temperature gradient points in the same direction as gravity, this setup is thermally unstable with respect to infinitesimally small perturbations of equilibrium quantities, e.g. velocity, temperature. If the system is perturbed and the mean temperature gradient is large enough, otherwise the perturbations would be suppressed by thermal diffusion and viscosity, the convective instability sets in and the fluid starts to move. Convective instability is caused by the following fact. Fluid elements that are displaced upward and are hotter than the surrounding fluid are less dense, so they are lighter in the gravitational field, and rise further up. On the contrary, fluid elements that are displaced downward and are colder than the surrounding fluid are more dense, so they are heavier, and sink further down. At the beginning, the instability grows exponentially, but later the growth slows down, and the instability eventually saturates in the nonlinear regime (e.g. [MY75][DR81]). If the temperature gradient is only slightly supercritical, movements of the fluid are slow, and the flow can form (to some extent) regular patterns (e.g. [Cha61]). However,

with increasing temperature difference between the plates, the motion of the fluid becomes more vigorous and more irregular in space and time. At this point nonlinear interactions begin to dominate the dynamics of the system, i.e. turbulent convection starts to develop (e.g. [MY75]). Blobs of light hot fluid detach from the bottom plate and rise up while heavy cool blobs sink. The fluid tends to establish an almost isothermal central part, where the flow is uniformly turbulent, separated by narrow boundary layers from the vertical boundaries (e.g. [MY75][Les97][VC03]).

Convection in a plasma, usually called magnetoconvection, manifests itself at macroscopic scales similarly as the convective flow in the aforementioned example. The typical length associated with convective motions and the typical length of turbulent eddies are much larger than any dynamic microscopic length (e.g. the mean-free path of particles or the Debye length). For example, convective motions in the solar convection zone occur at length scales of $(10^3$–$10^7)$ m, whereas the Debye length of the solar plasma is only $\approx 10^{-4}$m. Similarly, the typical time scale of the convective flow (the buoyancy time) and the typical time scale of turbulent motions (the large-eddy turnover time) are much longer than any microscopic time scale (e.g. the collisional time or the time associated with gyro-motions). In the solar convection zone, convective motions occur at time scales of $(10^2$–$10^3)$ s, whereas the time associated with gyro-motions is only $\approx 10^{-10}$s. Therefore, convection in a plasma is usually treated in the frame of a fluid model. The fluid model is valid for convection in other systems as well, e.g. in the liquid outer core of the Earth or in stars.

For simplicity, the plasma is assumed consisting of singly charged ions and electrons only. Moreover, the collisional time between electrons and ions is very short compared to the typical time scale of convective motions, so electrons and ions can be regarded as strongly coupled, and are treated together as one electrically conducting fluid (e.g. [Mes99]). Since the mass difference between electrons and ions is very large, the mass of the plasma can be identified with the heavy ions; the light and fast electrons carry the electric current. Convective motions and the local Alfvén speed are assumed to be very slow compared to the sound speed. This implies that the plasma flow is non-relativistic and incompressible. Due to the same reason the displacement current can be neglected, and shock waves as well as hydromagnetic waves (except for Alfvén waves) are excluded. These assumptions constitute the basis of the magnetohydrodynamic (MHD) approximation for incompressible fluids. The MHD model is discussed in more detail in e.g. [Bis97][Mes99].

Additionally, it is assumed that the Boussinesq approximation holds. This approximation is based on the fact that density of many common fluids is quite insensitive to fluctuations of temperature,

$$\frac{\delta\rho}{\rho_0} = -\alpha\theta \tag{1.1}$$

where ρ_0 and $\delta\rho$ are the equilibrium fluid density and density fluctuations, respectively. Temperature fluctuations are denoted by the symbol θ. The coefficient α is the volume (thermal) expansion coefficient, which is for many fluids at moderate temperatures in the range $(10^{-3}$–$10^{-5})\,\mathrm{K}^{-1}$. Such a range of values α corresponds to a weak temperature stratification, i.e. the size of the system is

small compared to the equilibrium pressure scale height. According to the expression (1.1), moderate variations of temperature result in negligible changes of density. A Boussinesq fluid can be therefore considered as incompressible with one important exception: the gravitational force can amplify the differences of density in the fluid, and the resulting buoyancy force might assume large values compared to other forces. Fluctuations of density are therefore considered only in the buoyancy force; in other terms they are neglected. A weak temperature stratification justifies the application of the Boussinesq approximation for neutral as well as electrically conducting fluids. More detailed derivations of the Boussinesq approximation can be found in e.g. [MY75][DR81][Bis03].

1.2 Mathematical formulation

1.2.1 Boussinesq MHD equations

Based on the assumptions introduced in the previous section, the Boussinesq MHD model is described by the equations of incompressible magnetohydrodynamics, including the buoyancy force and an advection-diffusion equation for temperature. In Gaussian units they read:

$$\frac{\mathrm{d}\rho}{\mathrm{d}t} = 0, \tag{1.2}$$

$$\rho\frac{\partial \mathbf{V}}{\partial t} + \rho(\mathbf{V}\cdot\nabla)\mathbf{V} - \frac{1}{c}(\mathbf{J}\times\mathbf{B}) = -\nabla P + \rho\mathbf{g} + \mu\Delta\mathbf{V}, \tag{1.3}$$

$$\frac{\partial \mathbf{B}}{\partial t} - \nabla\times(\mathbf{V}\times\mathbf{B}) = \eta\Delta\mathbf{B}, \tag{1.4}$$

$$\frac{\partial T}{\partial t} + (\mathbf{V}\cdot\nabla)T = \kappa\Delta T, \tag{1.5}$$

$$\nabla\times\mathbf{B} = \frac{4\pi}{c}\mathbf{J}, \tag{1.6}$$

$$\nabla\cdot\mathbf{B} = 0. \tag{1.7}$$

In these equations ρ is the density, $\mathbf{V}$ is the velocity, $\mathbf{B}$ is the magnetic field, T is the temperature, P is the thermal pressure, $\mathbf{J}$ is the electric current density, $\mathbf{g}$ is the gravitational acceleration, and c is the speed of light. The operator $\mathrm{d}/\mathrm{d}t = \partial/\partial t + (\mathbf{V}\cdot\nabla)$ denotes the total derivative. Constants μ, η, κ are the viscosity, the magnetic diffusivity and the thermal diffusivity, respectively. Because the mass of the system is conserved and equation (1.2) holds, the pressure P is not an independent variable and can be computed from the divergence of (1.3)

$$\Delta P = \nabla\cdot[-\rho(\mathbf{V}\cdot\nabla)\mathbf{V} + \rho\mathbf{g} + \frac{1}{c}\mathbf{J}\times\mathbf{B}]. \tag{1.8}$$

The set of equations (1.2)–(1.7) contains physical quantities that can be divided into mean and fluctuating parts

$$\mathbf{V} = \mathbf{V_0} + \mathbf{v}, \quad T = T_0 + \theta, \quad \mathbf{B} = \mathbf{B_0} + \mathbf{b}, \quad P = P_0 + p, \quad \mathbf{J} = \mathbf{J_0} + \mathbf{j} \tag{1.9}$$

In equilibrium the fluid is at rest with a linear temperature profile in the vertical direction. It is assumed that the mean magnetic field is equal to zero. The

mass of the fluid is constant, and uniformly distributed. The velocity equation (1.3) can be expressed in terms of vorticity $\boldsymbol{\Omega}$ $(= \nabla \times \mathbf{V})$, thereby eliminating the pressure term. The system is treated as incompressible, $\rho = \rho_0$; density fluctuations are allowed only in the buoyancy term. The application of these considerations together with (1.1) finally gives the set of Boussinesq MHD equations governing the dynamics of the fluctuations in the convective system

$$\frac{\partial \boldsymbol{\omega}}{\partial t} - \nabla \times (\mathbf{v} \times \boldsymbol{\omega} + \frac{1}{c\rho_0}\mathbf{j} \times \mathbf{b}) = -\alpha \nabla\theta \times \mathbf{g} + \nu \Delta \boldsymbol{\omega}, \tag{1.10}$$

$$\frac{\partial \mathbf{b}}{\partial t} - \nabla \times (\mathbf{v} \times \mathbf{b}) = \eta \Delta \mathbf{b}, \tag{1.11}$$

$$\frac{\partial \theta}{\partial t} + (\mathbf{v} \cdot \nabla)(T_0 + \theta) = \kappa \Delta \theta, \tag{1.12}$$

$$\boldsymbol{\omega} = \nabla \times \mathbf{v}, \quad \nabla \times \mathbf{b} = \frac{4\pi}{c}\mathbf{j}, \tag{1.13}$$

$$\nabla \cdot \mathbf{v} = \nabla \cdot \mathbf{b} = 0 \tag{1.14}$$

where $\nu = \mu/\rho_0$ is the kinematic viscosity. In the equations (1.10)–(1.14) all equilibrium values have vanished, except for ρ_0 and T_0 that expresses the mean linear temperature profile, and is therefore a function of position. These equations can be further simplified using nondimensional variables.

1.2.2 Nondimensional variables

There exist different possibilities how to normalize the equations of Boussinesq convection. In Rayleigh-Bénard (RB) setups the normalization to the thermal diffusion time $t_\mathrm{d} = L_0^2/\kappa$, where L_0 denotes the size of the RB box, is used very often, but this option is not very suitable for purposes of turbulence investigations in fully periodic domains. The diffusion time plays a dynamically less important role than the typical buoyancy time, i.e. the buoyancy time at the temperature gradient scale $L = T_0/(\nabla T_0)$, $t_\mathrm{b} = (\alpha g \nabla T_0)^{-1/2}$, that represents the typical time scale of dynamic changes of the flow due to buoyancy forces. In addition, the independent handling of dissipation coefficients is preferred in turbulence studies because they allow to control the relative importance of dissipative and nonlinear processes directly. Moreover, the system is supposed to be examined in fully periodic geometry, so a normalization based on the mean temperature gradient seems to be appropriate. All these arguments support the following choice of nondimensional variables

$$t' \equiv \frac{t}{t_\mathrm{b}}, \quad \mathbf{r}' \equiv \frac{\mathbf{r}}{L}, \quad \mathbf{v}' \equiv \frac{\mathbf{v}}{t_\mathrm{b}^{-1} L}, \quad \mathbf{b}' \equiv \frac{\mathbf{b}}{b_0}, \quad \theta' \equiv \frac{\theta}{L \nabla T_0}. \tag{1.15}$$

The quantity b_0 is the magnitude of typical magnetic field fluctuations. From now on, throughout the rest of the work, the new nondimensional variables will be used without primes. This choice of the normalization transforms the set

(1.10)–(1.14) to the form

$$\frac{\partial \boldsymbol{\omega}}{\partial t} - \nabla \times (\mathbf{v} \times \boldsymbol{\omega} + S_{\mathrm{B}}\, \mathbf{j} \times \mathbf{b}) = -\nabla\theta \times \mathbf{g}_0 + \tilde{\nu}\Delta\boldsymbol{\omega}, \tag{1.16}$$

$$\frac{\partial \mathbf{b}}{\partial t} - \nabla \times (\mathbf{v} \times \mathbf{b}) = \tilde{\eta}\Delta\mathbf{b}, \tag{1.17}$$

$$\frac{\partial \theta}{\partial t} + (\mathbf{v} \cdot \nabla)\theta = \tilde{\kappa}\Delta\theta + v_{z,x}, \tag{1.18}$$

$$\boldsymbol{\omega} = \nabla \times \mathbf{v}, \quad \nabla \times \mathbf{b} = \mathbf{j}, \tag{1.19}$$

$$\nabla \cdot \mathbf{v} = \nabla \cdot \mathbf{b} = 0. \tag{1.20}$$

The free dimensionless parameters are the dissipation coefficients $\tilde{\nu}, \tilde{\eta}, \tilde{\kappa}$ and the interaction parameter $S_{\mathrm{B}} = v_{\mathrm{A}}^2/v_0^2$ where $v_{\mathrm{A}} = b_0/\sqrt{4\pi\rho_0}$ is the magnitude of the characteristic Alfvén velocity and $v_0 = t_{\mathrm{b}}^{-1}L$ (see (1.15)). The parameter S_{B} determines the relative dynamical importance of velocity compared to magnetic field, and for the rest of the work is set equal to 1. This choice implies that magnetic field is measured in units of the characteristic Alfvén velocity. The vector $\mathbf{g}_0$ is a unit vector in the direction of gravity. The dissipation coefficients are related to several dimensionless parameters that are common in the context of Rayleigh-Bénard convection

$$\tilde{\nu} = \left(\frac{\mathsf{Pr}}{\mathsf{Ra}}\right)^{1/2}, \quad \tilde{\eta} = \left(\frac{\mathsf{Pr}}{\mathsf{RaPr_m}^2}\right)^{1/2}, \quad \tilde{\kappa} = \left(\frac{1}{\mathsf{RaPr}}\right)^{1/2}. \tag{1.21}$$

Here $\mathsf{Ra}, \mathsf{Pr}, \mathsf{Pr_m}$ are the Rayleigh number, the Prandtl number and the magnetic Prandtl number, respectively. They are defined as

$$\mathsf{Ra} \equiv \frac{\alpha g \triangle T L_0^3}{\nu\kappa}, \quad \mathsf{Pr} \equiv \frac{\nu}{\kappa}, \quad \mathsf{Pr_m} \equiv \frac{\nu}{\eta} \tag{1.22}$$

where $\triangle T$ is the temperature difference over the size of the Rayleigh-Bénard box L_0. The Rayleigh number Ra is a measure for the importance of buoyancy in the system compared to inertial forces and dissipations. Typical values of the Rayleigh number are e.g. in the convection zone of the Sun $\approx 10^{22}$ and in the Earth's outer core $\approx 10^7$. The Rayleigh number influences scale separation in convective systems, i.e. the ratio of the largest and dissipation scales of turbulent fluctuations. Therefore, in numerical simulations it is limited by applied resolutions given by available computational resources (e.g. [CHQ88][Bis03]). Thus only moderate values $\mathsf{Ra} \approx 10^9$ are achieved in numerical simulations, although in laboratory experiments the Rayleigh number is usually much higher, up to $\approx 10^{17}$. In fully periodic geometry nominal values of the Rayleigh number cannot be directly compared with the ones obtained from the Rayleigh-Bénard configuration because effects of physical boundaries are not involved in the fully periodic case, so the nominal Rayleigh number takes into account different physical processes than the Rayleigh number obtained from the Rayleigh-Bénard setup.

The Prandtl number Pr is the ratio of kinematic viscosity to thermal diffusivity. It can vary significantly; typical Prandtl numbers are: 10^{-10}–10^{-3} in the solar interior, 10^{-3}–10^{-2} for liquid metals, ≈ 0.7 for air and similar gases, ≈ 1 for hot fusion plasma, ≈ 10 for water and 10^2–10^4 for oils. Thermal conduction is very

efficient in low Prandtl number systems; on the contrary, high Prandtl number systems are viscosity dominated.

The magnetic Prandtl number $\mathsf{Pr_m}$ measures the relative importance of viscous and Ohmic dissipation. Typical magnetic Prandtl numbers are: $\approx 10^{-6}$ in the solar interior, $\approx 10^{-5}$ in the Earth's liquid core, $\approx 10^{2}$ for hot fusion plasma and $\approx 10^{14}$ for the interstellar medium.

Generally, only moderate values of all governing parameters are achieved in numerical simulations, because they determine scale separation in investigated systems, and are therefore limited by applied resolutions.

In following studies both Prandtl numbers are kept close to 1, i.e. none of the dissipation processes is preferred. However, Prandtl numbers in the investigated systems are not exactly unity since the primary parameters in the equations (1.16)–(1.20) that are numerically solved are dissipation coefficients, and Prandtl numbers are only derived quantities.

The magnetic Prandtl number can be expressed with the help of two other dimensionless parameters that are of special relevance for turbulence

$$\mathsf{Pr_m} = \frac{\mathsf{Re_m}}{\mathsf{Re}} \quad \text{where} \quad \mathsf{Re} \equiv \frac{L_0 v_0}{\nu} \quad \text{and} \quad \mathsf{Re_m} \equiv \frac{L_0 v_0}{\eta}. \tag{1.23}$$

In contrast to investigations in the Rayleigh-Bénard configuration with box size L_0, in fully periodic setups the quantities L_0 and v_0 are replaced by the typical size and the typical velocity of fluctuations in the system, respectively, as described later in section 3.1. The kinetic and magnetic Reynolds numbers, Re and $\mathsf{Re_m}$, express the importance of nonlinear terms compared to kinetic and magnetic dissipation, respectively. The Reynolds number Re determines if a flow is laminar (low Re) or turbulent (high Re). The critical kinetic Reynolds number is for most flows in the range 10^2–10^3.

Very low values of the magnetic Reynolds number $\mathsf{Re_m}$ imply that magnetic dissipation dominates a flow, whereas very high $\mathsf{Re_m}$ mean that the magnetic flux through a surface moving with the fluid remains almost constant. In other words, the parameter $\mathsf{Re_m}$ quantifies the "frozen in" property of magnetic fields, i.e. how much the magnetic field is dragged by the velocity field, and how much it can slip through. It can be shown that Reynolds numbers determine the ratio of large and dissipation scales in a flow and thereby their separation (e.g. [Bis97][Pop00]). Turbulent flows are characterized by large Reynolds numbers.

In the following the meaning of several different terms in (1.16)–(1.20) is explained briefly (for more detailed analysis, see e.g. [Mof78][Bis97][Mes99]). The last term on the l.h.s. of the vorticity equation (1.16) is the Lorentz force. It represents the influence of the magnetic field on the velocity dynamics. The Lorentz force is responsible for the energy transfer from the magnetic field to the velocity field and vice versa, so it drives or suppresses velocity fluctuations.

The first term on the r.h.s. of the vorticity equation (1.16) is the buoyancy force. This force is responsible for rising and sinking of fluid elements. The motion results from the fact that the gravitational force acting on a fixed volume of the fluid that is hot is weaker than the gravitational force acting on the same volume of the fluid that is cold. Consequently, hot parts of the fluid rise, while cold

parts sink. However, the fluid is incompressible, so a movement of one fluid element simultaneously causes such motions of other fluid elements that the incompressibility constraint remains preserved. Generally, in case of unstable stratification, i.e. if the temperature gradient points in the same direction as gravity, the buoyancy term provides energy for velocity fluctuations, and thereby drives the velocity field. In case of stable stratification, buoyancy stabilizes the system, so the onset of convection is suppressed.

The last term on the l.h.s. of the magnetic field equation (1.17) is the nonlinear interaction between velocity and magnetic field which influences the evolution of magnetic field fluctuations. This term is the counterpart of the Lorentz force. However, it does not only exchange the energy between both fields, but it redistributes this energy over different spatial scales of the magnetic field as well (see later in section 6.3).

The equation for temperature fluctuations (1.18) consists of the advection-diffusion part and a source term. The energy for excitation of temperature fluctuations is provided by the source term $v_{z,x}$ which appears due to the mean temperature gradient. Indices z, x denote two different orientations of the gradient, vertical and horizontal, respectively. This issue will be discussed in more detail in section 1.4.

In Ampere's law (1.19) the displacement current is neglected in the MHD approximation, so the current density is divergence-free. The dominance of the nonlinear terms in the set (1.16)–(1.20) leads to turbulent states of the flow. This topic is discussed in the following section.

1.3 Turbulent regimes

Throughout this work, convective turbulence is described by statistical averages of physical quantities. Fully periodic boundary conditions ensure that viscous boundary layers are not present in the system, so approximate statistical homogeneity of the turbulent flow is preserved. This permits using of all points in the computational domain for evaluations of spatial averages. However, turbulent convection is not statistically isotropic because buoyancy forces act in the vertical direction only. The question of anisotropy of convection is addressed in chapters 4 and 6. All examined systems are evolved to an approximately statistically stationary state, and are then followed for several typical buoyancy times. Details of individual simulations are described in particular chapters. The spatially averaged quantities are then averaged over the time domain as well.

Strong nonlinear interactions between fluctuations at different spatial scales underlie the nonlinear dynamics of turbulent flows. This applies to turbulent convection as well. In cases where the Reynolds number is higher than the critical value for the onset of turbulence, a large separation of spatial scales takes place. Based on the seminal ideas of Richardson and Kolmogorov, this interval of scales can be divided into three characteristic ranges: large, intermediate and small scales (e.g. [Fri95][Les97]). According to this concept, large-scale eddies contain most of the energy. Moreover, the energy is usually at large

scales injected to the system, e.g. due to mean gradients. On the contrary, at small scales viscous processes are dominant, so most of the energy is dissipated there. The large separation of the largest and dissipation scales at high Reynolds numbers leads to the existence of a wide range of intermediate scales where the dynamics is independent of large- and small-scale processes. It is assumed that at intermediate scales the energy is transferred from scale to scale locally in spectral space, i.e. by interactions of eddies of a similar size. This interval of scales is called inertial range. Since the influence of large- and small-scale effects is negligible in the inertial range, the energy "cascades" to smaller scales, and is conserved during this process. The main property of the inertial range is the absence of any typical length. This implies the existence of a self-similar scaling at inertial-range scales (e.g. [Fri95][Les97][Pop00]).

Based on different physical processes governing the nonlinear dynamics, two phenomenological theories of turbulent convection are currently available. These differ in the role of temperature fluctuations and their influence on the system dynamics. The relative importance of buoyancy forces and nonlinear interactions can be estimated comparing the magnitudes of associated terms in the vorticity equation (1.10)

$$\frac{v^2}{l} \sim (\alpha g)\theta. \tag{1.24}$$

This expression suggests the existence of a scale-dependent buoyancy time $t_\mathrm{b} \sim (\alpha g\theta/l)^{-1/2}$. Moreover, there is a typical length scale at which these two effects balance, the Bolgiano length L_B. In contrast to the buoyancy time t_b which can be obtained directly from (1.24), the Bolgiano length L_B is derived using simple dimensional considerations (e.g. [MY75][Bis03]). The Bolgiano length is the only possible combination of independent quantities influencing the spectral distribution of energy, i.e. energy dissipation rates and the buoyancy parameter, that gives the dimension of length (e.g. [MY75][Bis03]). Hence the Bolgiano length and the Bolgiano time t_B, i.e. the buoyancy time at the Bolgiano scale, are given as

$$L_\mathrm{B} \sim \frac{\varepsilon_v^{5/4}}{(\alpha g)^{3/2}\varepsilon_\theta^{3/4}}\ , \quad t_\mathrm{B} \sim \left(\frac{\alpha g\theta}{L_\mathrm{B}}\right)^{-1/2} \tag{1.25}$$

where $\varepsilon_v = \tilde{\nu}\int_v \omega^2 dV$ and $\varepsilon_\theta = \tilde{\kappa}\int_v (\nabla\theta)^2 dV$ are the kinetic and the thermal dissipation rate, respectively. The derivation is analogous to the application of Kolmogorov similarity hypotheses in homogeneous turbulence (see e.g. [Fri95][Les97]). It follows from the estimate (1.24) that the buoyancy force is more important at scales larger than the Bolgiano length. On the contrary, the buoyancy force influences the nonlinear dynamics negligibly at scales smaller than the Bolgiano length. The Kolmogorov phenomenology of turbulence is therefore expected to apply at inertial-range scales smaller than the Bolgiano scale, whereas the Bolgiano-Obukhov phenomenology is appropriate for the inertial region at scales larger than the Bolgiano scale.

1.3.1 Kolmogorov phenomenology

In the frame of the Kolmogorov phenomenology the temperature can be regarded as a passive scalar (e.g. [Fri95] [RBC96][Les97][War00][Bis03]). This

means that buoyancy forces are weak, and do not influence the nonlinear dynamics of the flow. Their effect can be neglected at inertial and small scales. At these scales temperature fluctuations are only passively advected by the velocity field. However, since the mean temperature gradient dominates the dynamics at the largest scales where nonlinear and dissipative effects are negligible, the importance of temperature fluctuations increases towards larger spatial scales. Temperature fluctuations therefore represent a significant source of energy at the largest scales, which is sufficient to excite velocity fluctuations. In the stationary case, kinetic energy is transferred through the inertial range from large to small scales with a constant energy transfer rate, i.e. a constant spectral energy flux, ϵ_v. This energy is eventually dissipated by viscosity at the smallest scales with the rate ε_v. This fact can be expressed using isotropic spatially averaged velocity fluctuations at the scale l

$$v_l \equiv \sqrt{< (\mathbf{v}(\mathbf{x}+\mathbf{l}) - \mathbf{v}(\mathbf{x}))^2 >} \tag{1.26}$$

and the associated nonlinear eddy-turnover time τ_l, $\tau_l \equiv l/v_l$, as

$$\frac{v_l^2}{\tau_l} \sim \frac{v_l^3}{l} \sim \epsilon_v \sim \varepsilon_v \sim \text{const.} \tag{1.27}$$

The scaling law for velocity fluctuations is obtained directly from this expression. It reads

$$v_l \sim \varepsilon_v^{1/3} l^{1/3}. \tag{1.28}$$

The scaling law (1.28) can be transformed to Fourier space. This leads with help of the relation $v_l^2 \sim kE(k)$, where $k \sim 1/l$, to the famous Kolmogorov prediction for the isotropic spectrum of kinetic energy (e.g. [Fri95][Pop00][Bis03])

$$E_k^{\mathrm{k}} \sim \varepsilon_v^{2/3} k^{-5/3}. \tag{1.29}$$

The energy spectrum of temperature fluctuations, i.e. of a passive scalar in this picture, transported by a Kolmogorov-type turbulence can be obtained by dimensional analysis as well. It can be shown that the energy of temperature fluctuations, also called temperature energy, is proportional to the fluctuations of entropy (see [Lvo91]). The idea is based on the expansion of entropy into a series in the quantity θ. The constant and the linear part do not contribute to the entropy which can be then associated with the quadratic part of this expansion. Thus in the following, both terms refer to the same physical quantity. According to the Obukhov-Corrsin phenomenology (see e.g. [Les97][Bis03]), the temperature energy is transferred with a constant spectral flux ϵ_θ from large to small scales in a way similar to the cascade of kinetic energy. This picture leads to the relation analogous to (1.27)

$$\frac{\theta_l^2}{\tau_l} \sim \frac{\theta_l^2 v_l}{l} \sim \epsilon_\theta \sim \varepsilon_\theta \sim \text{const.} \tag{1.30}$$

The scaling prediction for temperature fluctuations is obtained by substitution from (1.28). It reads

$$\theta_l \sim \varepsilon_\theta^{1/2} \varepsilon_v^{-1/6} l^{1/3}. \tag{1.31}$$

This relation in Fourier space yields the scaling prediction for the isotropic spectrum of temperature energy

$$E_k^\theta \sim \varepsilon_\theta \varepsilon_v^{-1/3} k^{-5/3}. \tag{1.32}$$

This scaling is valid in the inertial-convective subrange where the temperature field is passively advected by a developed turbulent flow, and is not influenced by small-scale dissipative structures. More detailed discussions of passive scalar convective turbulence can be found in chapters 4, 6.

1.3.2 Bolgiano-Obukhov phenomenology

In the Bolgiano-Obukhov (BO) phenomenology the temperature is regarded as an active scalar (e.g. [Bol59] [Obu59][Bis03]). In this case buoyancy forces are not negligible, but influence the spectral transfer of kinetic energy at all scales larger than the Bolgiano scale. Temperature and velocity are strongly coupled, i.e. the back-reaction of temperature field has a significant impact on the velocity field dynamics. The spectral kinetic energy flux is no longer constant in the inertial range, but the spectral entropy flux starts to play an important role. In case of stable stratification, the turbulent heat flux $v_z\theta$ extracts in the inertial range energy from the velocity field, and thereby drives the temperature fluctuations. Therefore, a kinetic energy spectrum steeper than the Kolmogorov spectrum $\sim k^{-5/3}$ is expected in this case. The situation corresponds to forced movements of fluid elements against buoyancy forces. In other words, buoyancy forces do work against the velocity field in the inertial range. This idea was initially suggested by Bolgiano and Obukhov for the inertial-range scaling of the kinetic energy spectrum of mechanically forced convective turbulence in setups with stable stratification ([Bol59][Obu59]). The same scaling behavior has been measured later in many laboratory experiments with unstable stratification as well. Although the exact explanation of experimentally observed inertial-range scaling is still not available, most probably a mechanism similar to the case of stable stratification works in case of unstable stratification as well. The spectral kinetic energy flux at buoyancy-dominated inertial-range scales is, apart from the factor (αg), almost fully determined by the turbulent heat flux at the same scale. This fact can be expressed using dimensional considerations as

$$\epsilon_v \sim \frac{v_l^3}{l} \sim (\alpha g)\theta_l v_l. \tag{1.33}$$

The process of the entropy cascade is different from the passive scalar case. Temperature fluctuations at particular scale interact via buoyancy with velocity eddies of the same size. These eddies are unstable, break up, and form somewhat smaller eddies that conversely produce temperature fluctuations at similar scales. In this way the entropy in the system cascades to small scales in the inertial range with the flux ϵ_θ. In contrast to the passive case, the temperature influences the velocity field due to buoyancy forces at all scales larger than the Bolgiano scale. It is assumed that the transfer of entropy in the inertial range occurs locally in spectral space, and is constant. The temperature energy is eventually dissipated at the smallest scales by thermal diffusion at the rate

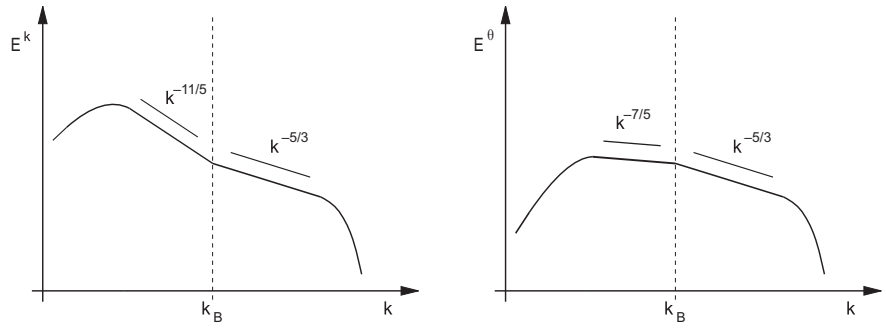

Figure 1.1: Schematic plot of two inertial subranges in the kinetic energy spectrum (left) and the entropy spectrum (right) of hydrodynamic convective turbulence. The wavenumber $k_{\rm B}$ is the mode number associated with the Bolgiano length $L_{\rm B}$.

ε_θ. This process can be expressed as

$$\frac{\theta_l^2}{\tau_l} \sim \frac{\theta_l^2 v_l}{l} \sim \epsilon_\theta \sim \varepsilon_\theta \sim \text{const.} \tag{1.34}$$

The combination of both expressions, (1.33) and (1.34), leads to the Bolgiano-Obukhov inertial-range scaling prediction for kinetic energy fluctuations

$$v_l^2 \sim (\alpha g)^{4/5} \varepsilon_\theta^{2/5} l^{6/5} \tag{1.35}$$

and for temperature energy fluctuations

$$\theta_l^2 \sim (\alpha g)^{-2/5} \varepsilon_\theta^{4/5} l^{2/5}. \tag{1.36}$$

Both relations can be transformed to Fourier space. This yields

$$E_k^{\rm k} \sim (\alpha g)^{4/5} \varepsilon_\theta^{2/5} k^{-11/5} \tag{1.37}$$

and

$$E_k^{\theta} \sim (\alpha g)^{-2/5} \varepsilon_\theta^{4/5} k^{-7/5}. \tag{1.38}$$

A general spectrum of convective turbulence consisting of both, Kolmogorov and Bolgiano-Obukhov, inertial ranges is schematically sketched in Fig 1.1. The BO scaling and the Kolmogorov scaling appear at large and small inertial-range scales, respectively. The wavenumber $k_{\rm B}$ associated with the Bolgiano scale determines the scale where both parts of the inertial range coincide.

According to the relation (1.25) the Bolgiano length depends on the kinetic dissipation rate ε_v. This fact can be related to the inertial-range dynamics as follows. If the spectral flux of kinetic energy at inertial-range scales decreases (by some unspecified physical mechanism) in the cascade on its way down to small scales, the amount of energy that has to be finally dissipated is smaller, and the kinetic dissipation rate decreases as well. The Bolgiano length therefore moves to smaller scales extending the inertial range with BO scaling further.

Scaling predictions for MHD systems are discussed later in the chapters dedicated to the investigation of magnetoconvection.

1.4 Horizontal temperature gradient

In numerical simulations of convection in fully periodic geometry difficulties with obtaining a stationary turbulent state arise. They are related to a special kind of instability, called elevator instability. This instability appears due to the presence of fully periodic boundary conditions which allow a particular unstable solution of the governing equations (1.16)–(1.20) ([CLT05]). For simplicity, only hydrodynamic convection in 2D is considered. The horizontal axis and vertical axis are denoted by x and z, respectively. In addition, the normalization to the thermal diffusion time (cf. subsection 1.2.2 and (1.22)) is used in order to allow for an easy comparison with other works. The governing equations read

$$\frac{\partial \omega}{\partial t} + (\mathbf{v}\cdot\nabla)\omega = -\mathsf{RaPr}\frac{\partial \theta}{\partial x} + \mathsf{Pr}\Delta\omega, \tag{1.39}$$

$$\frac{\partial \theta}{\partial t} + (\mathbf{v}\cdot\nabla)\theta = \Delta\theta + v_z. \tag{1.40}$$

This set of equations allows to search for a solution in the form $\omega = \omega_0 e^{(\lambda t + \mathrm{i}\mathbf{k}\cdot\mathbf{x})}$, $\theta = \theta_0 e^{(\lambda t + \mathrm{i}\mathbf{k}\cdot\mathbf{x})}$ which transforms the equations into

$$\lambda\omega_0 = \mathrm{i}k_x \mathsf{RaPr}\,\theta_0 - \mathsf{Pr}\,k^2\omega_0, \tag{1.41}$$

$$\lambda\theta_0 = -k^2\theta_0 + \frac{\mathrm{i}k_x}{k^2}\omega_0. \tag{1.42}$$

The expression for the growth rate λ follows ([CLT05]) directly as

$$\lambda = -\frac{1}{2}(\mathsf{Pr}+1)k^2 \pm \frac{1}{2}\sqrt{(\mathsf{Pr}+1)^2k^4 + 4\mathsf{Pr}\left(\mathsf{Ra}\frac{k_x^2}{k^2} - k^4\right)}. \tag{1.43}$$

The system becomes unstable if

$$\mathsf{Ra}\frac{k_x^2}{k^2} - k^4 > 0. \tag{1.44}$$

For example, for a system with box size $L = 1$ and with quantities independent of z, this condition gives the critical Rayleigh number for the onset of elevator instability $\mathsf{Ra_c} = (2\pi/L)^4 = (2\pi)^4 \approx 1559$. This implies that at Rayleigh numbers higher than $\mathsf{Ra_c}$ the excitation of the elevator instability is in z-periodic setups unavoidable. The physical picture of the instability with the most unstable mode $k_x = 1$ consists of two vertical streamers pointing up and down. This configuration is illustrated in Fig. 1.2. The flow in these streamers is accelerated by the gravitational force up to the point when the transition layer between the streamers becomes unstable. Consequently, the flow becomes turbulent, and saturates nonlinearly. Then the instability is excited again. In fact, this configuration corresponds to the magnification of the convective system around the transition between rising and sinking blobs of fluid. Other unstable modes with different k_x can be excited as well, forming a similar situation with more streamers in the horizontal direction. Both pictures show that the streamers extend over the entire vertical length of the box, and thus involve Fourier modes with $k_z = 0$. One of possible solutions to avoid the elevator instability is to put the

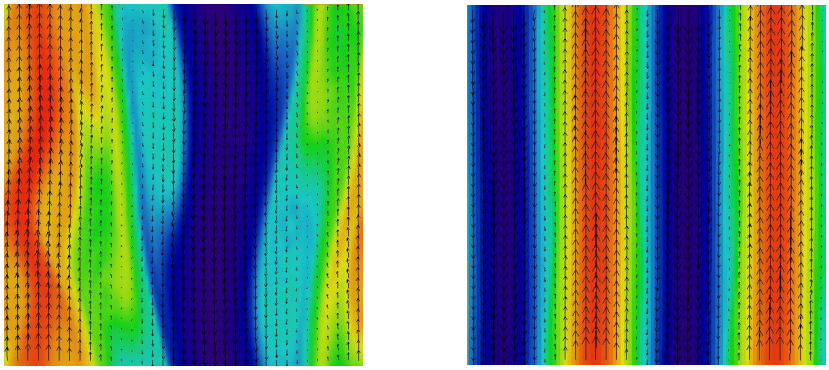

Figure 1.2: The elevator instability consisting of 2 streamers (left) and 4 streamers (right). Temperature fluctuations are denoted by color (red – high values, blue – low values). Velocity vectors are represented by arrows.

mean temperature gradient horizontally. This leads to a configuration where $\nabla T \perp \mathbf{g}$, so the instability condition takes the form

$$-\mathsf{Ra}\frac{k_x k_z}{k^2} - k^4 > 0. \tag{1.45}$$

This condition inhibits exciting of the instability with $k_z = 0$ since then $-k^4 < 0$, i.e. the condition is not satisfied independently of the Rayleigh number. This fact was empirically tested in the course of the work. Due to the action of a large-scale temperature gradient, temperature fluctuations are driven predominantly at the largest scales. Therefore, the rotation of the gradient should not modify the dynamics of the inertial range. However, it is possible that the direct drive of mechanical energy is absent in setups with horizontal temperature gradients because these do not change the potential energy of the system directly, so the flow is driven purely entropically ([LF92]). Therefore, according to [LF92] the BO scaling should fill the entire inertial interval down to the dissipation range. This idea coincides with one of the goals of this work: investigations of the Bolgiano-Obukhov regime of convective turbulence. In order to avoid the excitation of elevator instability, the mean temperature gradient is set in the horizontal direction in all performed simulations with fully periodic boundaries.

Chapter 2

Numerical code

The majority of available phenomenological theories of turbulence in fluids is based on interactions between turbulent eddies of similar size l. This view corresponds to interactions of fluctuations with similar wave numbers $k \sim 1/l$. Moreover, inhomogeneous viscous boundary layers are absent in numerical simulations of convective turbulence in fully periodic boxes, in contrast to Rayleigh-Bénard configurations with closed vertical boundaries. Approximate statistical homogeneity of convective flows is therefore preserved in fully periodic setups. Both facts motivate the application of spectral (Fourier) methods to turbulent convection. In these methods the calculation of spatial derivatives is transformed to simple multiplications with wave vectors. Furthermore, spectral methods calculate the time evolution of the governing equations directly in Fourier space, and thereby allow for a straightforward computation of spectra of various physical quantities. The drawback of spectral methods is an occurrence of the Gibbs phenomenon in simulations of compressible flows (e.g. [Bri74][CHQ88]). The Gibbs phenomenon manifests itself as characteristic oscillations of Fourier series near steep gradients. However, the Boussinesq approximation of convective turbulence excludes the formation of shocks, i.e. discontinuities of physical quantities, due to the incompressibility constraint. Spectral methods are for incompressible flows usually more accurate than finite difference schemes (e.g. [CHQ88]). In other words, spectral methods usually require less discretization points than finite difference schemes in order to achieve the same accuracy.

The set of the Boussinesq equations describing convective turbulence is solved by means of direct numerical simulations (DNS) (e.g. [CHQ88][Pop00]). The DNS approach deals with the complete set of differential equations, and avoids additional physical approximations. This point is of fundamental importance for turbulence investigations because no simplification of the nonlinear terms is employed. This is the main advantage of DNS compared to other possible approaches. On the contrary, for instance large eddy simulations (LES) focus on the evolution of the energy containing large-scale eddies, while physical processes at smaller scales are approximated by an artificial viscosity model. Also

other physical models of turbulence, e.g. EDQNM[1], involve incomplete or phenomenological descriptions of the nonlinear interactions, thereby omitting for example intermittency effects. Direct numerical simulations therefore represent a valuable tool for obtaining a detailed knowledge about the nonlinear dynamics and cascade properties. The drawback of DNS is a large computational cost caused by the necessity to resolve the wide range of spatial scales of turbulent flows.

The numerical code used in this work is based on the previously developed program package for simulations of incompressible magnetohydrodynamic turbulence ([BM00]). The original program was extended by the Boussinesq approximation to account for problems of convection.

2.1 Pseudospectral scheme

The set of equations describing the model of convective turbulence (1.16)–(1.20) is solved in Fourier space. The computational domain is a cubic box of size 2π which is uniformly discretized with N points in each direction. This corresponds to the Fourier wavenumber range $-\frac{N}{2}+1 \leq k \leq \frac{N}{2}-1$. All physical quantities are approximated by truncated Fourier series

$$\widehat{\boldsymbol{\omega}}_{\mathbf{k}}(t) = \frac{1}{N^3}\sum_{\mathbf{j}} \boldsymbol{\omega}(\mathbf{x_j},t)e^{-\mathrm{i}\mathbf{k}\cdot\mathbf{x_j}}, \quad \widehat{\theta}_{\mathbf{k}}(t) = \frac{1}{N^3}\sum_{\mathbf{j}} \theta(\mathbf{x_j},t)e^{-\mathrm{i}\mathbf{k}\cdot\mathbf{x_j}}, \quad \ldots$$
$$\text{where} \quad x_j = \frac{2\pi j}{N} \quad j = 0,\ldots,N-1 \quad \text{for each direction.} \tag{2.1}$$

Here, $\widehat{\boldsymbol{\omega}}_{\mathbf{k}}(t), \widehat{\theta}_{\mathbf{k}}(t)$ are Fourier counterparts of real-space quantities. The mode $\mathbf{k} = (0,0,0)$ of all physical quantities, i.e. their spatial average, is set equal to zero. Additionally, since the original physical quantities are real-valued functions, they satisfy additional relations of symmetry in Fourier space

$$\widehat{\boldsymbol{\omega}}_{-\mathbf{k}}(t) = \widehat{\boldsymbol{\omega}}^{\star}_{\mathbf{k}}(t), \quad \widehat{\theta}_{-\mathbf{k}}(t) = \widehat{\theta}^{\star}_{\mathbf{k}}(t), \quad \ldots \tag{2.2}$$

where * means the complex conjugate value. Thus it is necessary to calculate and store only one half of Fourier modes; the other half can be obtained from the relation (2.2). This symmetry therefore allows to reduce memory requirements and to speed up calculations. Additionally, in Fourier space all spatial derivations are replaced by multiplications with wave vectors.

Fourier transformations of the Boussinesq MHD equations underline the nature of nonlinear interactions. Different Fourier modes interact only via the nonlinear terms; in linear terms they can be treated separately. The equations (1.16)–

[1]EDQNM – Eddy-Damped Quasi-Normal Markovian approximation. A statistical model of turbulence based on two-point closures for the hierarchy of moment equations assuming that turbulence is nearly Gaussian (e.g. [Ors74][Les97]).

(1.20) transformed in Fourier space read

$$\left(\frac{\mathrm{d}}{\mathrm{d}t}+\tilde{\nu}k^2\right)\widehat{\boldsymbol{\omega}}_{\mathbf{k}} = \mathrm{i}\mathbf{k}\times[\widehat{\mathbf{v}\times\boldsymbol{\omega}}+(\mathrm{i}\mathbf{k}\times\widehat{\mathbf{b})}\times\mathbf{b}]_{\mathbf{k}}+\mathrm{i}\mathbf{k}\widehat{\theta}_{\mathbf{k}}\times\mathbf{k}_z^0, \tag{2.3}$$

$$\left(\frac{\mathrm{d}}{\mathrm{d}t}+\tilde{\eta}k^2\right)\widehat{\mathbf{b}}_{\mathbf{k}} = \mathrm{i}\mathbf{k}\times[\widehat{\mathbf{v}\times\mathbf{b}}]_{\mathbf{k}}, \tag{2.4}$$

$$\left(\frac{\mathrm{d}}{\mathrm{d}t}+\tilde{\kappa}k^2\right)\widehat{\theta}_{\mathbf{k}} = -[\widehat{\mathbf{v}\cdot\mathrm{i}\mathbf{k}\theta}]_{\mathbf{k}}+\widehat{(v_z)}_{\mathbf{k}}, \tag{2.5}$$

$$\widehat{\mathbf{v}}_{\mathbf{k}} = \frac{\mathrm{i}\mathbf{k}}{k^2}\times\widehat{\boldsymbol{\omega}}_{\mathbf{k}} \tag{2.6}$$

where $\mathbf{k}_z^0=(0,0,1)$ is a unit vector in the z direction. The last equation in the set ensures that the velocity remains divergence free at all times. All equations (2.3)–(2.6) are in algebraic form except the terms in square brackets. These terms are convolution sums arising from the nonlinearities. Their general form is

$$\widehat{[a\,b]}_{\mathbf{k}} = \sum_{\mathbf{k}=\mathbf{p}+\mathbf{q}}\widehat{a}_{\mathbf{p}}\,\widehat{b}_{\mathbf{q}} \quad \text{where} \quad |\mathbf{k}|,|\mathbf{p}|,|\mathbf{q}|\le\frac{N}{2}-1. \tag{2.7}$$

A straightforward calculation of this expression in three dimensions requires $O(N^6)$ operations (e.g. [Bri74]). This fact is unsatisfactory, and would limit the application of spectral methods to small Fourier data sets. However, there is a possibility to evaluate the convolution sum (2.7) in $O(N^3\log_2 N)$ operations (e.g. [CHQ88]). The trick is to transform variables $\widehat{a}_{\mathbf{p}},\widehat{b}_{\mathbf{q}}$ at first back to real space, perform the multiplication there, and finally transform the result to Fourier space again. This is the basic idea of pseudospectral schemes (e.g. [CHQ88]). A small inconvenience stems from the fact that the result of the pseudospectral procedure is contaminated with a so-called aliasing error caused by finite discretization. The technique applied to remove the aliasing error is discussed in the next section.

2.2 Treatment of aliasing errors

The aliasing error of the pseudospectral scheme is in the code removed by a truncation technique (e.g. [CHQ88]). This de-aliasing technique is based on calculations with extended Fourier fields of size $M\ge 3N/2$. A Fourier variable resulting from the pseudospectral procedure can be expressed as a sum of two contributions (for simplicity only a one-dimensional convolution is considered)

$$\widehat{[a\,b]}_k = \sum_{k=p+q}\widehat{a}_p\,\widehat{b}_q+\sum_{k\pm N=p+q}\widehat{a}_p\,\widehat{b}_q. \tag{2.8}$$

The first term is the result of the convolution that is required; the other term is the aliasing error. If the new size of Fourier fields $M\ge 3N/2$ is considered instead of the original size N, and if original Fourier variables are padded with zeros in the extra wavenumber range $M/2-1\ge|p|,|q|\ge N/2-1$, the second term in the expression (2.8) vanishes, and the exact result of the convolution is obtained. This de-aliasing procedure is sometimes called the 3/2 rule. However, the number of operations performed in this case is higher than in the simple

pseudospectral calculation. In one dimension the truncation technique requires about 50% more numerical operations, in more dimensions the additional computational effort is even larger. This stems from the fact that many finally discarded modes that do not carry a physical information have to be included and evaluated.

In order to obtain a better performance of the de-aliasing step, the scheme can be improved further. In three dimensions it is possible to reduce the number of extra modes introducing a spherical truncation of Fourier variables. This de-aliasing method assumes a sphere of physical Fourier modes padded to a cubic shape. The aliasing error due to the modes in this sphere was empirically found to be of the order of the discretization error, and is therefore neglected. In this way the number of additional operations in three dimensions is reduced by $\approx 70\%$ compared to the full 3/2 de-aliasing. However, the spherical truncation is not sufficiently accurate in two dimensions, produces significant deviations from exact results, and therefore cannot be applied. Hence all simulations performed in two dimensions employ the full 3/2 rule in order to remove aliasing errors.

2.3 Temporal discretization

The set of Boussinesq equations (2.3)–(2.6) is evolved in time using the leapfrog scheme. The leapfrog scheme is a fast explicit two-step algorithm that uses a constant time step. The scheme is implemented as second order accurate, and is suitable for non-dissipative problems. However, the algorithm is unstable in the presence of dissipation (e.g. [CHQ88]). An additional modification is therefore required to avoid this property. The stability of the leapfrog scheme can be achieved by using an integrating-factor technique which treats the linear diffusion term exactly (e.g. [CHQ88][MP89]). The application of this technique leads to the reformulated version of the original equations (2.3)–(2.6) (for illustration purposes only the temperature equation is shown, the other equations are modified analogously)

$$\frac{\mathrm{d}}{\mathrm{d}t}(e^{\tilde{\kappa}k^2 t}\widehat{\theta}_{\mathbf{k}}) = e^{\tilde{\kappa}k^2 t}\left(-[\widehat{\mathbf{v}\cdot\nabla\theta}]_{\mathbf{k}} + \widehat{(v_z)}_{\mathbf{k}}\right). \tag{2.9}$$

Here, the dissipation term is included implicitly, and does not appear explicitly in the equation. Moreover, now the stability and accuracy properties do not depend on the dissipation term any more, and they are given solely by the nonlinear term (e.g. [CHQ88]). Using this modification the leapfrog scheme can be easily applied. The scheme takes the explicit form

$$\widehat{\theta}^{n+1}_{\mathbf{k}} = \widehat{\theta}^{n-1}_{\mathbf{k}} e^{-\tilde{\kappa}k^2 2\triangle t} + 2\triangle t e^{-\tilde{\kappa}k^2\triangle t}\left(-[\widehat{\mathbf{v}\cdot\nabla\theta}]_{\mathbf{k}} + \widehat{(v_z)}_{\mathbf{k}}\right)^n \tag{2.10}$$

where n is a time step index and $\triangle t$ denotes time interval of one step. A solution obtained with the leapfrog scheme is very often modified by temporal oscillations with the period $2\triangle t$ (e.g. [CHQ88]). These arise due to the inaccurate approximation of time derivatives, and can be avoided by temporal averaging of the solution over every two subsequent time steps.

The time step is chosen in agreement with the Courant-Friedrichs-Lewy (CFL) condition

$$\triangle t \leq \frac{\triangle x}{v_{\max}} = \frac{\pi}{k_{\max} v_{\max}} \tag{2.11}$$

where $v_{\max}$ is the maximal speed of propagation in the system. Since incompressibility is assumed, the fast magneto-acoustic wave is excluded, and therefore a reasonable estimate for the maximal velocity is $v_{\max} \approx \sqrt{E^{\mathrm{tot}}}$. For particular simulation runs, the time step is additionally adjusted to the maximal stable value.

2.4 Initial and boundary conditions

The convective system is investigated in a fully periodic box. Fully periodic boundary conditions inhibit the formation of viscous boundary layers appearing in the often used standard Rayleigh-Bénard (RB) setup. Boundary layers introduce inhomogeneity to the system that can influence statistical averages. Furthermore, the Rayleigh-Bénard setup models a global system with closed vertical boundaries. However, this work focuses on inherent properties of convective turbulence, and therefore a zoom inside the central part of the Rayleigh-Bénard box is preferred. This magnification corresponds to fully periodic geometry. In this case, boundary layers do not influence the system, so the turbulence remains approximately statistically homogeneous. Moreover, several authors suggest an important role of viscous boundary layers because, according to them, the observed Bolgiano-Obukhov scaling appears due to the action of blobs of fluid (thermal plumes) detaching from these regions (e.g. [GL92]). The model investigated in this work avoids all these additional complications, and focuses only on the bulk of convective turbulence. However, several numerical tests of the code are performed using the RB setup with free-slip vertical boundaries. These tests, validating the functionality of the code, are presented in the last section of this chapter.

The initial states of the performed simulations are obtained by a multi-step procedure. In the hydrodynamic case, the system is initialized with small random fluctuations of the temperature field at a small resolution, typically with 32 Fourier modes in one dimension. Then the numerical evolution of the convective instability is followed until it saturates in the nonlinear state. After that, the system is evolved for several typical buoyancy times until it achieves an approximately statistically stationary state. At this stage the simulation is stopped; the resolution is increased, and the dissipation coefficients are decreased. Then the system is followed again for several typical buoyancy times during which it adjusts to the new parameter values. This procedure is repeated until the maximal possible resolution given by available computational resources is reached. The maximal resolution varies in individual simulations, and is specified in particular chapters. At this stage the system adapts to the new parameters again, and it is then evolved for several typical buoyancy times long enough for obtaining stationary statistical averages.

The initialization of the magnetic field is implemented in two different ways. One possibility is to initialize the magnetic field with small random fluctuations

at the very beginning. Then the convective instability develops, and consequently the turbulent magnetic dynamo starts to operate, increasing the level of magnetic fluctuations in the system up to the saturation level. The other possibility is to take an already established stationary hydrodynamic system and introduce random magnetic fluctuations of the order of velocity fluctuations. After that, the system reacts vigorously to the new conditions. However, a new approximately stationary state is obtained after several typical buoyancy times. In both versions the system is followed for several typical buoyancy times after the magnetic energy saturates in order to acquire an approximately stationary state. Both initializations generate turbulent states with identical statistical properties.

2.5 Parallelization and optimization

The numerical code is parallelized using the MPI library ([MPIb]). This option allows computations on large distributed memory systems as well as on shared memory machines. The parallelization is accomplished by dividing the computational box into slices in one arbitrary direction. The individual slabs are assigned to available processors. The calculation runs independently on individual processors, except for evaluations of the Fourier transformations. This is the crucial point of the computation. Generally, Fourier transformation demands all-to-all data exchange between processors which decreases the overall computational performance. Two different libraries PFFT and FFTW are used in the code for solving parallel Fourier transformation. FFTW is a public library developed at MIT ([FFT]). PFFT is a platform-dependent solution based on the ESSL library which is provided and optimized by IBM for the POWER architecture. Despite the Fourier transformations, the code exhibits a good scalability with respect to the number of used processors (see Fig 2.1). The dot-dashed line in the picture indicates ideal linear scaling. The good scaling property is preserved when the required resolution increases. Fig. 2.2 illustrates this property showing the relative speedup using 256 and 512 processors for two different data loads (resolutions 512^3 and 1024^3). Both pictures confirm the fact that the scalability of parallel codes depends on the ratio of data load to communication costs: the larger resolution and the less communication, the better scaling performance.

Two options are implemented for saving of data frames. One is the platform dependent writing of binary data which is the fastest way of doing I/O (input/output) operations. The major disadvantage is the absence of a simple way how to read/write in parallel from/to the same file on general parallel file systems (gpfs). This drawback is overcome with the other implemented possibility that uses the HDF5 format ([HDF]) and the MPI-2 standard containing parallel I/O ([MPIa]). The HDF5 is a platform independent binary format, and the MPI-2 contains a functionality that takes care of the synchronization of simultaneous accesses to a file on gpfs.

The major part of the calculations ($\approx 85\%$) consists of Fourier transformations. The rest of the code, i.e. time evolution, run-time diagnostics, etc., has a minor share of the computational time. It is therefore important to use the Fast Fourier

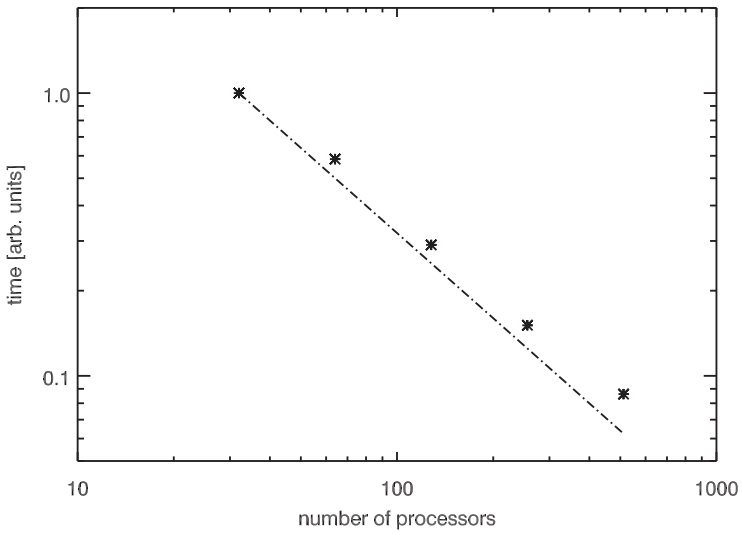

Figure 2.1: The scaling of the code with increasing number of processors. The dot-dashed line indicates a linear scaling. During the test the convective MHD system on the grid 512^3 is evolved for 100 time steps.

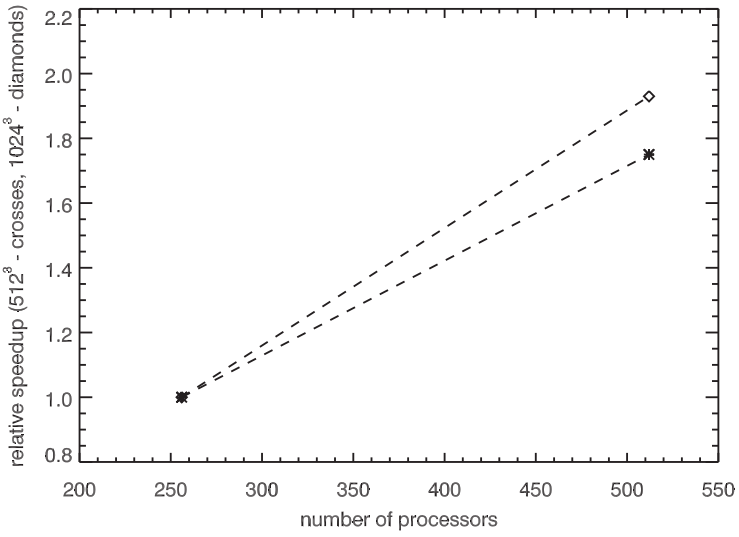

Figure 2.2: The relative speedup of the code using 256 and 512 processors. During the test the convective MHD system with resolutions 512^3 and 1024^3 is evolved for 100 time steps.

Transformation (FFT) scheme that is able to compute one three-dimensional transformation in $O(N^3 \log N)$ steps. The FFT works most efficiently with arrays of size of a power of two. Thus such resolutions are preferred. Furthermore, it is necessary to minimize the number of transformations. They are required in the pseudospectral procedure that evaluates vector products in the equations (2.3)–(2.6). An optimization of numerical codes usually faces the dilemma of memory versus speed efficiency. The memory optimized version of the code requires only 4 temporary arrays, but it computes 10 one-way transformations per nonlinearity. The speed optimized version needs 5 temporary arrays, but performs 9 one-way transformations per nonlinearity. The difference between these two options seems to be small, but it becomes important when many Fourier transformations and huge data sets are considered. Generally, a decision has to be made according to configurations of particular supercomputers. The speed optimized solution was chosen in the code since the size of memory was not a limiting factor. This option consists of 18 and 36 one-way transformations in the hydrodynamic and MHD case per cycle, respectively. The optimization is done for the IBM Regatta system at Rechenzentrum Garching with standard monitoring software tools. The performance of the parallel communication is tuned using software options for the IBM Federation network switch.

2.6 Rayleigh-Bénard tests

In order to validate the functionality of the code several three-dimensional numerical tests are performed. These tests are computed exceptionally in the Rayleigh-Bénard setup since for this configuration some analytical results exist. Free-slip boundary conditions are assumed at the upper and the lower boundary

$$v_z = \partial_z v_x = \partial_z v_y = 0 \quad \Rightarrow \quad \omega_x = \omega_y = \partial_z \omega_z = 0. \tag{2.12}$$

The system is without magnetic field, and is infinitely extended in the horizontal direction. A constant mean temperature gradient is kept in the vertical direction. This setup is convectively stable up to the critical Rayleigh number that follows from linear theory (e.g. [Cha61][DR81])

$$\mathsf{Ra_c} = \frac{27}{4}\pi^4 \approx 657,5 \quad \text{and} \quad \lambda = 2^{3/2} L_0 \approx 2.8284 L_0. \tag{2.13}$$

Here, λ is the horizontal wavelength of the most unstable mode, and L_0 is the vertical size of the Rayleigh-Bénard box. In the simulation with the resolution 64^3, the predicted value of $\mathsf{Ra_c}$ is confirmed with an error of less than 1%. The accuracy of the obtained value depends on the resolution and the numerical method.

At slightly supercritical Rayleigh numbers, the flow should display one of several analytically predicted regular patterns (e.g. [Cha61]). The specific realization depends on the values of applied parameters and the geometry of the box. In the performed test the convective flow is established in the form of pure two-dimensional rolls (see Fig. 2.3). Roll axes aligned in the x and the y direction are equally probable. The rolls are slightly asymmetric. This asymmetry grows with increasing Rayleigh number, and consequently distorts the rolls.

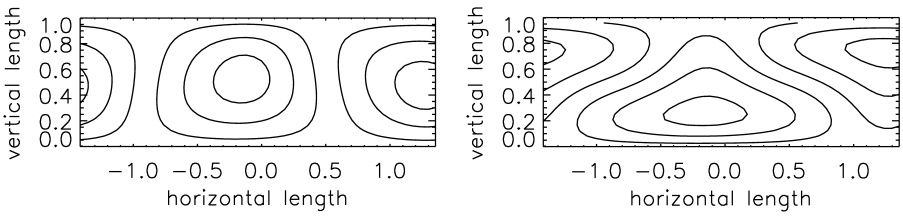

Figure 2.3: Two-dimensional rolls in 3D hydrodynamic Rayleigh-Bénard convection with $\mathsf{Ra} \approx 10\mathsf{Ra_c}$. Left: isolines of the vertical component of the velocity in a vertical slice through the computational box. Right: isolines of the temperature in the same slice.

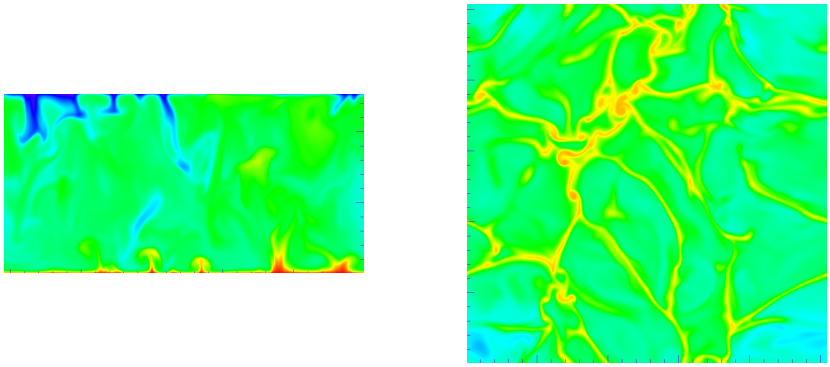

Figure 2.4: The structure of the temperature (red – high values, blue – low values) in thermal convection at $\mathsf{Ra} \approx 10^7$ with the resolution $256^2 \times 128$. Left: a vertical slice through the computational box showing thermal plumes detaching from narrow boundary layers. Right: a horizontal slice near the lower boundary showing the intermittent structure of plume footprints.

A further increase of the Rayleigh number leads to deformations and oscillations of the rolls. However, they are stable up to the point where buoyancy forces and resulting shear stresses are so strong that the regular pattern is completely destroyed, and the flow starts to be turbulent. At this stage the flow develops an almost isothermal layer of fluid in the central region separated by narrow boundary layers from vertical boundaries. This situation is demonstrated on the left hand side of Fig. 2.4 which shows the results of the simulation with $\mathsf{Ra} \approx 10^7$ and the resolution $256^2 \times 128$. The picture displays the temperature in the vertical slice through the computational box. Blobs of fluid (thermal plumes) detaching from narrow vertical boundary layers can be identified as well as the almost isothermal central region.

The right hand side of Fig. 2.4 represents a horizontal slice through the temperature field close to the lower boundary. This picture shows the intermittent arrangement of thin thermal plumes. This fine network of plume footprints is also in qualitative agreement with other works (e.g. [KH00][VY00]). The structure of footprints is not stationary, but evolves rapidly in time. Thermal plumes are fully three-dimensional objects that are subject to all irregular motions of the turbulent velocity field.

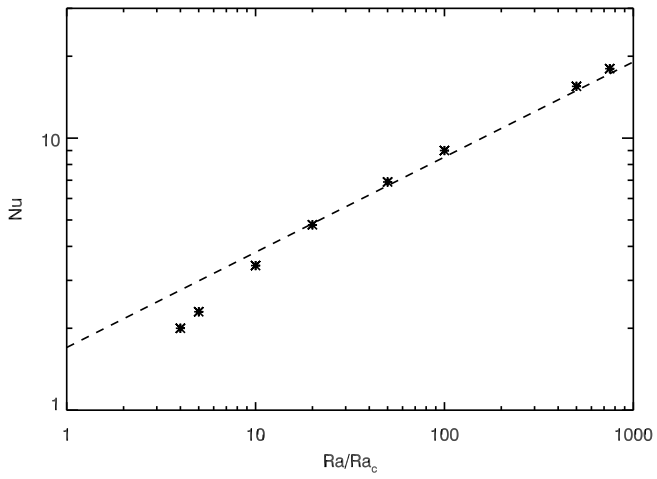

Figure 2.5: The scaling of the Nusselt number Nu as a function of $\mathsf{Ra/Ra_c}$. The dashed line represents the fit $\sim \mathsf{Ra}^{0.34}$.

An important characteristics of convective flows is the Nusselt number Nu. The Nusselt number is the dimensionless ratio of the total vertical heat flux to the vertical heat flux caused by molecular conduction only. The expression for Nu follows from the integration of the temperature equation (1.5) over z (e.g. [Sig94][BTT98][CLT05])

$$\mathsf{Nu} \equiv \frac{\overline{v_z T} - \kappa \partial \overline{T}/\partial z}{\kappa(\triangle_L T/L)} = \frac{\langle v_z \theta \rangle}{\kappa(\triangle_L T/L)} + 1 \approx \left. \frac{\langle v_z \theta \rangle}{\kappa(\triangle_L T/L)} \right|_{Ra \gg Ra_c} \tag{2.14}$$

where $\triangle_L T$ is the temperature difference over the distance L. The overbar denotes an average over a horizontal plane and time. The symbol $\langle \cdot \rangle$ denotes an average over the volume and time. The Nusselt number is always $\mathsf{Nu} \geq 1$ where the equality implies that the vertical heat flux is caused by molecular conduction only. At high Rayleigh numbers the vertical turbulent heat flux increases significantly the efficiency of the vertical heat transport in the system, so the Nusselt number is dominated by the convective part of the total vertical heat flux. The Nusselt number measures the efficiency of the vertical heat flux in the bulk of the flow, so it does not include the effect of boundary layers. Near boundaries almost the whole temperature drop takes place, i.e. almost $\triangle_L T/2$ over a boundary layer. The boundary layer Nu is usually much smaller. In nondimensional units introduced in subsection 1.2.2 the Nusselt number can be expressed as

$$\mathsf{Nu} = \frac{\langle v_z \theta \rangle}{\tilde{\kappa}} + 1 \approx \frac{\langle \varepsilon_\theta \rangle}{\tilde{\kappa}}. \tag{2.15}$$

The second expression is a useful relation coming from the integration of the temperature equation (1.18) multiplied by θ over the volume (e.g. [Sig94] [CLT05]).

The Nusselt number test consists of the calculation of the Nu as a function of the Rayleigh number. According to the scaling exponent of this function, it is possi-

ble to distinguish three regimes of convective turbulence (there is still no general agreement on this classification): a soft turbulence regime with $\mathsf{Nu} \sim \mathsf{Ra}^{1/3}$, a hard turbulence regime with $\mathsf{Nu} \sim \mathsf{Ra}^{2/7}$ and an asymptotic regime, i.e. very large Ra, with $\mathsf{Nu} \sim \mathsf{Ra}^{1/2}$ (e.g. [Kra62][CCI93] [Sig94][BTT98][VC99][KH00] [VY00][CLT05]). The result of the test computation with resolutions from 64^3 up to 256^3 for Rayleigh numbers in the range $4\mathsf{Ra_c}$–$750\mathsf{Ra_c}$ is shown in Fig. 2.5. The dashed line corresponds to the scaling $\mathsf{Nu} \sim \mathsf{Ra}^{0.34}$ which is close to the exponent $1/3$, suggesting that the system operates in the soft turbulence regime. It should be mentioned that the estimation of the Nusselt number as well as of the critical Rayleigh number depends on the used resolution, i.e. they are more accurate if the resolution increases.

The results presented in this section are used mainly as tests of the numerical code. The examination of turbulent convection in the closed Rayleigh-Bénard box is not the main purpose of this work. The subsequent chapters focus on spectral and statistical properties of turbulent convection in fully periodic geometry.

Chapter 3

2D hydrodynamic convection

Two-dimensional hydrodynamic convection is a relatively simple system that allows to test the Bolgiano-Obukhov predictions for convective turbulence. Since a strictly two-dimensional configuration cannot be examined under laboratory conditions, experimental research is restricted to investigations of convection in quasi-two-dimensional setups, for instance in thin films (e.g. [MW98][ZW02]). On the contrary, many numerical simulations have been performed in the two-dimensional Rayleigh-Bénard configuration (e.g. [GL92][VY99]), but considerably less attention has been paid to numerical studies of bulk turbulence in the fully periodic system ([TI00][BHS01]). Much higher Rayleigh and Reynolds numbers can be achieved in two dimensions (e.g. [VY00][Sig94]) than in three-dimensional numerical setups. Since high Reynolds number implies a large separation between integral and dissipation scales and thereby a broad inertial range, better scaling properties are expected in two-dimensional simulations compared to three-dimensional setups. Moreover, the nonlinear dynamics of hydrodynamic convection is less complicated than that of magnetoconvection, i.e. it does not involve effects of magnetic fields. However, there are important differences between hydrodynamic turbulent convection in two and three dimensions, mainly due to the inverse cascade of kinetic energy and the special role of enstrophy in 2D.

3.1 Energy balance

In the case of 2D hydrodynamic convection with a horizontal mean temperature gradient, the set of Boussinesq equations (1.16)–(1.20) reduces to

$$\frac{\partial \omega}{\partial t} + (\mathbf{v} \cdot \nabla)\omega = -\frac{\partial \theta}{\partial x} + \tilde{\nu}\Delta\omega, \tag{3.1}$$

$$\frac{\partial \theta}{\partial t} + (\mathbf{v} \cdot \nabla)\theta = \tilde{\kappa}\Delta\theta + v_x, \tag{3.2}$$

$$\omega = \partial_z v_x - \partial_x v_z, \quad \nabla \cdot \mathbf{v} = 0. \tag{3.3}$$

In these equations the horizontal axis and the vertical axis are denoted by x and z, respectively. Neglecting buoyancy forces, i.e. the passive scalar case, and viscosity, equation (3.1) expresses the fact that the vorticity is advected by the velocity, i.e. a constant vorticity is associated with every fluid particle. In this case two quadratic invariants exist

$$E^{\mathrm{k}} = \frac{1}{2}\int_S v^2 dS, \tag{3.4}$$

$$E^{\Omega} = \int_S \omega^2 dS \tag{3.5}$$

where E^{k} is the kinetic energy per unit mass, E^{Ω} is the enstrophy, and the symbol S denotes the surface of the fully periodic domain. Moreover, a two-dimensional flow is non-helical with velocity vectors always perpendicular to the vorticity.

On the contrary, these two quadratic invariants are not conserved in 2D turbulent convection where temperature is an active scalar. The total energy balance of fluctuations yields

$$\frac{d}{dt}\int_S \frac{1}{2}(v^2 + \theta^2) dS = \int_S (v_z\theta + v_x\theta) dS - \int_S (\tilde{\nu}\omega^2 + \tilde{\kappa}(\nabla\theta)^2) dS. \tag{3.6}$$

The r.h.s. of this equation combines sources and sinks of the total energy. The first integral consists of heat fluxes that drive the system, so it is a source of energy. The other integral on the r.h.s. of (3.6) represents the total energy dissipation rate, so it works as a sink of energy.

A two-dimensional hydrodynamic turbulent flow exhibits an inverse transfer of kinetic energy, i.e. the kinetic energy cascades in the inertial range from small to large scales in contrast to the three-dimensional case. The kinetic energy therefore tends to condensate at the largest scales of a bounded system. In order to inhibit this condensation that can influence the flow dynamics considerably, a large-scale damping in the form $\beta\nabla^{-2m}$ is added to the dissipative term on the r.h.s. of (3.1). The value of the parameter m controls the spectral distribution of the large-scale viscosity. High values of m imply a predominant damping of spectral modes at the largest scales, whereas low values of m cause that the viscosity influences a larger number of spectral modes at large scales. Values $m = 3$ and $\beta = 1$ are chosen for the simulation presented in this chapter.

The following sections discuss the numerical results of 2D hydrodynamic convection. The simulation is performed with the resolution 4096^2. The dissipation coefficients are $\tilde{\nu} = 8 \cdot 10^{-6}$ and $\tilde{\kappa} = 3 \cdot 10^{-5}$. These values are chosen in order to obtain the maximal extension of the inertial ranges of both fields. They correspond to a nominal Rayleigh number $\mathsf{Ra} \approx 4.5 \cdot 10^9$. The Reynolds number (see (1.23)) based on the typical velocity $v_0 \approx (E^{\mathrm{k}})^{1/2}$ and on the associated length $L_0 \approx (E^{\mathrm{k}})^{3/2}/\varepsilon_v$ is approximately $\mathsf{Re} \approx 7 \cdot 10^4$. The simulation is followed for 9 typical buoyancy times.

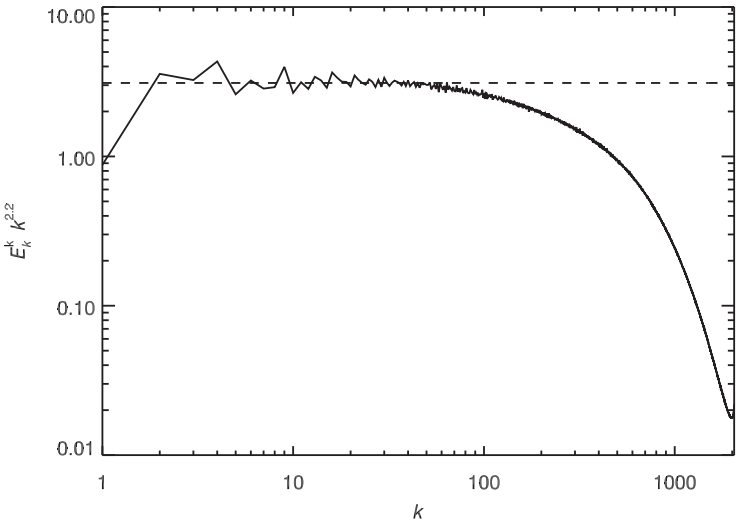

Figure 3.1: The time-averaged angle-integrated kinetic energy spectrum normalized by $\varepsilon_\theta^{2/5}$ and compensated by the scaling factor $k^{11/5}$. The horizontal dashed line indicates the BO scaling with the exponent $-11/5 = -2.2$.

3.2 Scaling of energy spectra

The angle-integrated kinetic energy spectrum

$$E^{\mathrm{k}}(k) \equiv \int_{\forall \mathbf{k}} E^{\mathrm{k}}(\mathbf{k})|_{k=k_x^2+k_z^2} d\mathbf{k} \tag{3.7}$$

obtained from the performed simulation by time-averaging over 9 typical buoyancy times is depicted in Fig. 3.1. The spectrum is normalized by the factor $\varepsilon_\theta^{2/5}$ appearing in the BO prediction (cf. (1.37)) and compensated by the BO scaling factor $k^{11/5}$. The horizontal dashed line in the plot indicates the BO scaling with the exponent $-11/5 = -2.2$. The picture shows the BO scaling of the kinetic energy spectrum in a range about one decade in wavenumber, $5 \lesssim k \lesssim 50$. The entire following part of the spectrum belongs to the dissipation range. The simulation is performed with an ordinary viscosity, i.e. no hyperviscosity is used. The kinetic energy dissipation wavenumber (e.g. [MY75][TS94])

$$k_{\mathrm{d}}^{\mathrm{k}} = \tilde{\nu}^{-5/8} \varepsilon_\theta^{1/8} \tag{3.8}$$

is found to be around $k_{\mathrm{d}}^{\mathrm{k}} \approx 1490$. The wavenumber $k_{\mathrm{d}}^{\mathrm{k}}$ indicates approximately the scale where the dissipation term and the nonlinear term have a comparable impact on the flow dynamics under the assumption of the BO scaling. The Bolgiano scale is in this simulation around the wavenumber $k_{\mathrm{B}} \approx 3100$, so it is located outside of the resolved spectral region. Thus the entire inertial range of the spectrum is dominated by buoyancy, and exhibits the BO scaling, i.e. no transition to a small-scale Kolmogorov behavior occurs. The decrease of the kinetic energy at $k = 1$ is caused by the applied large-scale damping.

Fig. 3.2 displays the time-averaged angle-integrated temperature energy spec-

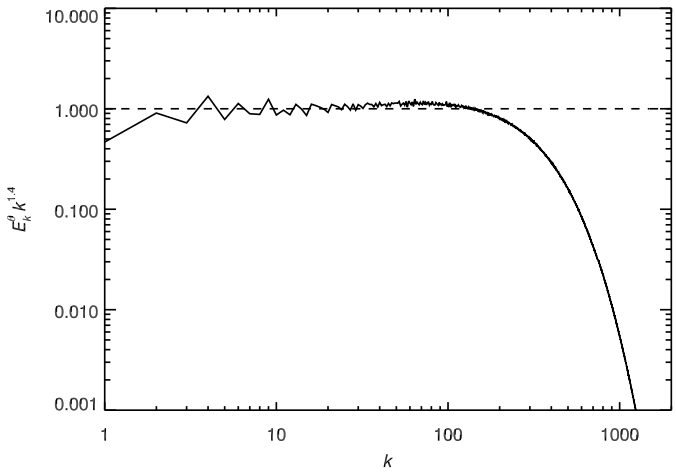

Figure 3.2: The time-averaged angle-integrated temperature energy spectrum normalized by $\varepsilon_\theta^{4/5}$ and compensated by the scaling factor $k^{7/5}$. The horizontal dashed line indicates the BO scaling with the exponent $-7/5 = -1.4$.

trum defined analogously to (3.7) and obtained from the same run. The spectrum is normalized by the factor $\varepsilon_\theta^{4/5}$ and compensated by the scaling factor $k^{7/5}$ (cf. (1.38)). The horizontal dashed line in the plot indicates the BO scaling with the exponent $-7/5 = -1.4$. The inertial range of the spectrum extends over about one and half decade in wavenumber, $3 \lesssim k \lesssim 80$, and penetrates to scales smaller compared to the spectrum of the kinetic energy. The scaling of entropy in the inertial region coincides approximately with the BO scaling indicated by the horizontal dashed line.

A small deviation of the scaling exponent ($< 5\%$) can be identified around $k \approx 80$ in front of the transition to the dissipation range. This departure is similar to a bottleneck effect found in systems with hyperviscosity (cf. [BSC98][HB06]). The bottleneck effect is caused by a higher level of dissipation compared to that provided by simple viscosity. It should be stressed that the performed simulation does not employ any kind of small-scale hyperviscosity. Furthermore, this phenomenon occurs in the energy spectra of all quantities that are subject to a direct cascade (see later). On the contrary, no such deviation can be identified in the spectrum of the kinetic energy (Fig. 3.1) which is transported by an inverse cascade. This property is detected in all simulations of hydrodynamic convection analyzed in the course of the work. It is necessary to mention that the dissipation range of the temperature energy spectrum is well resolved, i.e. $k_{\max}/k_{\mathrm{d}} \gtrsim 1.5$ (e.g. [Pop00]), since $k_{\mathrm{d}}^\theta \approx 653$ where

$$k_{\mathrm{d}}^\theta = \tilde{\kappa}^{-5/8} \varepsilon_\theta^{1/8} \tag{3.9}$$

is the entropy dissipation wavenumber. Thus $k_{\max}/k_{\mathrm{d}}^\theta \approx 3.1 > 1.5$ which implies that the entropy dissipation range is resolved sufficiently.

In the frame of the Bolgiano-Obukhov phenomenology, it is possible to predict

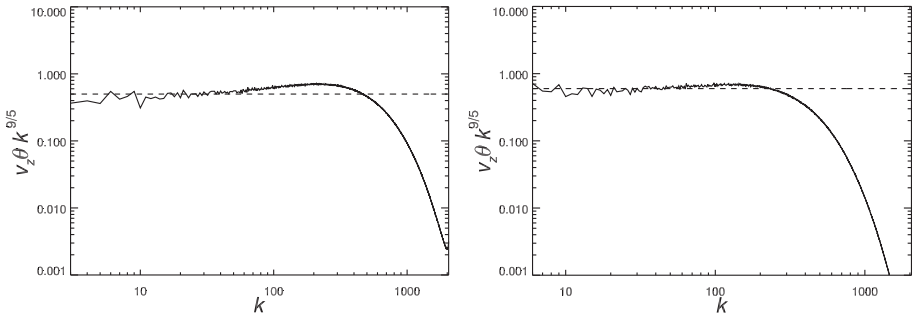

Figure 3.3: The time-averaged compensated spectrum of the vertical heat flux $v_z\theta$. Horizontal dashed lines indicate the predicted scaling $k^{-9/5}$. Left: The original spectrum obtained from the performed simulation. Right: The spectrum obtained from the same run with the thermal dissipation increased by 100%.

the scaling of the vertical heat flux $v_z\theta$ ([GL93]). Since the vertical heat flux is in the inertial range characterized by the absence of any typical length, similarly as the kinetic energy, it is expected that the vertical heat flux exhibits inertial range scaling. The value of the scaling exponent can be derived by dimensional considerations ([GL93]) from equation (1.10) multiplied by θ

$$\frac{(v_z\theta)_l v_l}{l} \sim \alpha g \theta_l^2 \quad \Rightarrow \quad (v_z\theta)_l \sim \alpha g \theta_l^2 v_l^{-1} l \tag{3.10}$$

where $(v_z\theta)_l$ denotes the vertical heat flux at scale l. This relation together with the predicted BO scaling for velocity fluctuations (1.35) and temperature fluctuations (1.36) yields ([GL93])

$$(v_z\theta)_l \sim (\alpha g)^{1/5} \varepsilon_\theta^{3/5} l^{4/5} \quad \Rightarrow \quad (v_z\theta)_k \sim (\alpha g)^{1/5} \varepsilon_\theta^{3/5} k^{-9/5}. \tag{3.11}$$

The spectrum of the vertical heat flux is shown on the l.h.s. of Fig. 3.3. The horizontal dashed line indicates the scaling with the exponent $-9/5$. Despite the fact that the scaling exponent is close to the expected value, the spectrum is in the inertial range flatter, probably due to the presence of a similar bump as in the entropy spectrum (cf. Fig. 3.2). This suggestion is supported by the picture on the r.h.s. of Fig. 3.3 that represents the same heat flux spectrum but with the thermal dissipation increased by 100%. Now the bump in the spectrum is less pronounced indicating that this effect tends to diminish with increasing thermal dissipation.

Generally, the spectra are in good agreement with the BO predictions, although small deviations from exact scaling exponents ($< 5\%$) are observed. The following section focuses on the nonlinear dynamics of the system investigating the behavior of nonlinear terms in more detail.

3.3 Nonlinear transport

3.3.1 Transfer functions

A transfer function is a very powerful tool to examine different properties of spectral transport caused by nonlinear terms (e.g. [Fri95][Pop00]). It can be obtained by considering a nonlinear energy flux, e.g. the flux of kinetic energy $\epsilon_v \sim \mathbf{v} \cdot (\mathbf{v} \cdot \nabla)\mathbf{v}$, in Fourier space. Spectral fluxes of the kinetic energy and the entropy summed from $k_{\max}$ to k result in

$$T_k^{\mathrm{EV}} = \frac{1}{2} \sum_{|k'|>k} \sum_{p,q} \delta_{k',p+q} i k'_l \left(\frac{k'_m k'_n}{k'^2} - \delta_{m,n}\right) \widehat{v}_l^{\star}(k') \widehat{v}_m(p) \widehat{v}_n(q), \tag{3.12}$$

$$T_k^{\theta} = \frac{1}{2} \sum_{|k'|>k} \sum_{p,q} \delta_{k',p+q} i k'_l \widehat{\theta}^{\star}(k') \widehat{v}_l(p) \widehat{\theta}(q), \tag{3.13}$$

where T_k^{EV} and T_k^{θ} denote the transfer function of the kinetic energy and the entropy, respectively. The symbol * stands for a complex conjugate value. Both energy fluxes, $v\frac{v^2}{2}$ and $v\frac{\theta^2}{2}$, can be recognized on the r.h.s. of the expressions (3.12) and (3.13), respectively. Since the transfer functions are for simplicity assumed to be isotropic, their particular value at some k gives the amount of energy transferred from all modes with $k' < k$ to all modes with $k' \geq k$. Thus a positive transfer function implies a direct cascade of energy to small scales.

The transfer functions T_k^{EV} and T_k^{θ} summed from $k = 0$ to $k_{\max}$ vanish by the Gauss-Ostrogradsky theorem in case of periodic boundaries because the nonlinear terms can be expressed in divergence form. This implies that the kinetic energy flux and the entropy flux separately conserve the associated energies. Therefore, the nonlinear interactions associated with advection only redistribute the energy over different Fourier modes within the individual fields. On the contrary, in case of magnetoconvection, nonlinear terms exchange the energy between velocity and magnetic fields as well.

The entropy transfer function T_k^{θ} and the absolute value of the kinetic energy transfer function $|T_k^{\mathrm{EV}}|$ obtained from the performed simulation are depicted in Fig. 3.4. They are normalized by the corresponding dissipation rates, ε_θ and $\varepsilon_\theta^{3/5}$, respectively (cf. later (3.14), (3.15)). The normalized transfer functions are denoted by the symbol $\hat{}$. Moreover, $|\hat{T}_k^{\mathrm{EV}}|$ is compensated by $k^{4/5}$ (cf. later (3.15)). The entropy transfer function is positive at all wave numbers indicating a direct cascade of the entropy to small scales. The normalized function is in the inertial region almost constant approaching a value of 1. This means that the spectral transport of temperature energy in the inertial range is not influenced by other dynamical processes that would extract or add energy. Temperature energy is neither gained nor lost in the cascade from large to small scales, and is completely dissipated at the smallest scales by thermal diffusion.

On the contrary, the kinetic energy transfer function $\hat{T}_k^{\mathrm{EV}}$ is negative from $k = 1$ to $k \approx 400$. Hence the kinetic energy in this range is subject to an inverse cascade which is well-known from studies of 2D hydrodynamic turbulence (e.g. [Les97][Pop00]). The nonlinear transfer remains direct in the dissipation range from $k \approx 400$ to $k_{\max}$; however, the dynamics in this range is dominated by

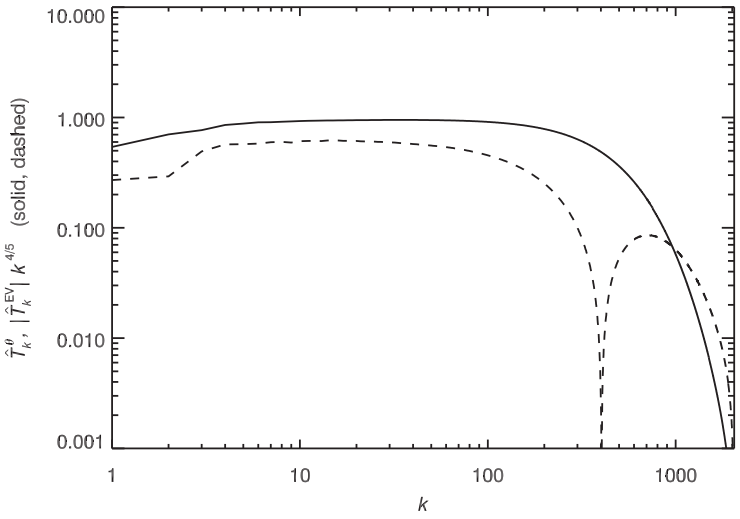

Figure 3.4: The entropy transfer function $\hat{T}_k^\theta$ (solid) and the absolute value of the kinetic energy transfer function $|\hat{T}_k^{\mathrm{EV}}|$ (dashed) which is compensated by $k^{4/5}$ (cf. (3.14), (3.15)). Both transfer functions are normalized by the corresponding dissipation rates, ε_θ and $\varepsilon_\theta^{3/5}$, respectively. For $1 \lesssim k \lesssim 400$ the transfer function $\hat{T}_k^{\mathrm{EV}}$ is negative whereas for $k \gtrsim 400$ it is positive.

dissipation. Comparing the extension of the self-similar parts of both transfer functions, the entropy cascade penetrates to smaller scales which is in agreement with the energy spectra (cf. Fig. 3.1, Fig. 3.2). Furthermore, $|\hat{T}_k^{\mathrm{EV}}|$ is not constant, but it exhibits a scaling with the exponent close to $-4/5$. This fact is in agreement with the Bolgiano-Obukhov phenomenology because (e.g. [Lvo91])

$$\epsilon_v \sim \frac{v_l^2}{\tau_l} \sim \frac{v_l^3}{l} \quad \overset{(1.35)}{\Longrightarrow} \quad T_k^{\mathrm{EV}} \sim (\alpha g)^{6/5} \varepsilon_\theta^{3/5} k^{-4/5} \tag{3.14}$$

where ϵ_v is the nonlinear kinetic energy transfer rate and τ_l denotes the nonlinear eddy turnover time. On the contrary,

$$\epsilon_\theta \sim \frac{\theta_l^2}{\tau_l} \sim \frac{\theta_l^2 v_l}{l} \quad \overset{(1.34)}{\Longrightarrow} \quad T_k^\theta \sim \text{const.} \tag{3.15}$$

as it is demonstrated in Fig. 3.4 as well.

The dependence of the spectral flux of the kinetic energy on the spatial scale suggests the existence of a mechanism that influences the cascade dynamics (in contrast to the constancy of T_k^θ). This process is the vertical heat flux caused by buoyancy. The time-averaged vertical heat flux is positive over all scales (cf. Fig. 3.3), so it injects the energy for velocity fluctuations not only at the largest scales but at inertial-range scales as well. Therefore, velocity fluctuations in the inertial range gain the energy by two distinct mechanisms: via the cascade of the kinetic energy and from the vertical heat flux directly.

This fact can be used for explaining why the transfer function of the spectral kinetic energy flux decreases faster ($T_k^{\mathrm{EV}} \sim k^{-4/5}$) than in Kolmogorov turbulence ($T_k^{\mathrm{EV}} \sim$ const.). In the investigated system the kinetic energy is subject

to an inverse cascade, i.e. it is transported from small to large scales. However, at each spatial scale the amount of transported energy increases by the contribution from the vertical heat flux. The resulting spectral kinetic energy flux is therefore not constant, but increases towards large scales. This picture corresponds to the steeper spectrum of this flux. This is a very important fact, especially for the comparison to three-dimensional hydrodynamic convection (discussed later in chapter 4).

In the course of the work it was tested that the presence of the BO regime of turbulent convection depends on the Rayleigh number. If it is small enough, buoyancy forces do not affect the nonlinear dynamics, so the system operates in the Kolmogorov regime of turbulent convection. Therefore, the fact that the enstrophy is an ideal invariant in 2D, and consequently that the kinetic energy is transported by an inverse cascade, does not necessarily lead to the presence of the BO regime of turbulent convection; a high Rayleigh number is needed as well. In addition, the BO regime does not inhibit cascades of kinetic energy and enstrophy in contrast to what is suggested for 2D Rayleigh-Taylor turbulence ([Che03]).

3.3.2 Shell to shell transfer

More detailed information about turbulent cascades can be obtained by an examination of shell to shell spectral energy transfer at inertial-range scales (e.g. [DVE01][AMP05]). In the following, energy in particular shells in Fourier space is considered. The shells are assumed to be circular, and consist of all wave vectors $\mathbf{k}$ that satisfy $K - 1/2 < k \leq K + 1/2$ where K is the label of the shell. For instance, the expression $\mathbf{v}_K$ denotes a velocity field with all Fourier modes equal to zero, except for modes in the shell K.

The nonlinear terms on the l.h.s. of the vorticity equation (3.1) and of the temperature equation (3.2) contribute to the energy change of the Fourier shell K in the form

$$T_{vv}(K) \equiv \int_S -\mathbf{v}_K \cdot (\mathbf{v}_P \cdot \nabla)\mathbf{v}_Q dS, \tag{3.16}$$

$$T_{\theta\theta}(K) \equiv \int_S -\theta_K (\mathbf{v}_P \cdot \nabla)\theta_Q dS, \tag{3.17}$$

respectively. Since the nonlinear terms conserve energy, the relations (3.16) and (3.17) express the redistribution of energy due to nonlinear interactions between different Fourier modes in the shells P, Q and K. This means that no energy is gained or lost.

However, there exist an important difference between both expressions. In the case of entropy change $T_{\theta\theta}$ (3.17), velocity modes in the shell P work only as a mediator of the entropy transport because no kinetic energy is transferred to or from the velocity field (see previous section). Thus in contrast to the change of entropy in the shell K which originates in the shell Q, the source of the change of kinetic energy in the shell K cannot be uniquely identified (e.g. [Kra59][Ors74]). This fact represents a quite important difference between the terms in (3.16) and (3.17). It is therefore reasonable to evaluate only the entropy

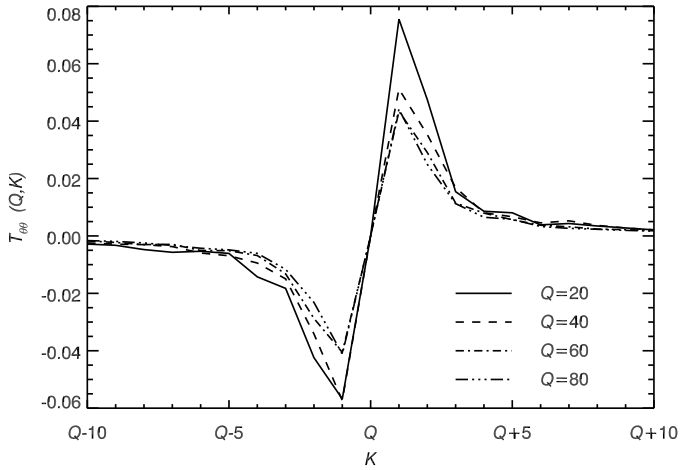

Figure 3.5: The entropy transfer $T_{\theta\theta}$ between different shells in Fourier space. The shells are chosen from the entropy inertial region, $20 \lesssim k \lesssim 80$. The entropy transport in the inertial range is essentially direct and local.

transfer $T_{\theta\theta}$ due to the shell Q mediated by the complete velocity field, i.e. all velocity shells P. The same estimate for the kinetic energy transfer would be incomplete and misleading.

The shell to shell entropy transfer in the performed simulation of 2D turbulent convection is plotted in Fig. 3.5. The transfer is evaluated for the shells $Q = 20, 40, 60, 80$. These wave numbers belong to the inertial interval of the entropy $3 \lesssim k \lesssim 80$ (cf. Fig. 3.2, Fig. 3.4). The plot shows that the entropy transport is essentially local in spectral space. For instance, due to the interaction between the velocity field and the entropy in the shell $Q = 20$, the entropy in the shell $Q = 19$ is transported to the shell $Q = 21$. The same amount of entropy is transferred from and to the shell $Q = 20$. Thus the total change of the entropy in the shell $Q = 20$ is equal to zero. Despite the fact that the transport is not strictly local, almost all of the entropy transfer due to the shell Q occurs between shells in the range from $Q - 5$ to $Q + 5$ (the simulation consists of 2047 shells). Furthermore, the transport is not exactly symmetric. This feature is difficult to interpret because the range of the modes in the shell Q (see definition above) is not exactly symmetric as well. The structure of the transfer is similar for all examined Q shells; only the amount of transported entropy decreases with increasing Q. Hence the local and direct nature of the entropy cascade in 2D turbulent convection is confirmed.

3.4 Structure functions

Structure functions are spatial two-point correlations describing the distribution of turbulent eddies (e.g. [Fri95][Les97][Pop00][Bis03]). A knowledge of struc-

ture functions of all orders is equivalent to the full statistical description of a turbulent field by probability density functions of field increments. The longitudinal velocity structure function of order p, $S_p^v(\mathbf{x}, \mathbf{l})$, is defined as an average of velocity increments of moment p

$$S_p^v(\mathbf{x}, \mathbf{l}) \equiv \left\langle \left[\mathbf{v}(\mathbf{x}+\mathbf{l}) - \mathbf{v}(\mathbf{x}) \cdot \frac{\mathbf{l}}{l} \right]^p \right\rangle \tag{3.18}$$

where $\langle \cdot \rangle$ denotes time or space average. Structure functions of other fields are defined in a similar way as two-point field increments. In turbulence that is statistically homogeneous and isotropic, i.e. statistically translational invariant and independent of direction, structure functions depend only on the increment distance, $S_p^v(l) = \langle [\delta v(l)]^p \rangle$. Turbulent convection in fully periodic geometry, i.e. without effects of physical boundaries, can be treated as an approximately statistically homogeneous turbulent flow. Moreover, since the large-scale anisotropies caused by gravity and mean temperature gradient are partially suppressed in the inertial range due to the efficient turbulent mixing, structure functions are for simplicity assumed to be isotropic.

An important property of structure functions is that they exhibit a self-similar behavior in the inertial range

$$S_p^v(l) = a_p l^{\zeta_p}. \tag{3.19}$$

Thus the knowledge of all scaling exponents ζ_p and constants a_p is sufficient to yield the full information about the statistical distribution of eddies in the inertial range. Furthermore, the structure function of the second order is in fact the real space counterpart of the one-dimensional Fourier energy spectrum (e.g. [Bis03]).

The structure functions obtained from the performed simulation of 2D hydrodynamic convection are depicted in Fig. 3.6. Since functions of odd orders can assume negative values, they are computed from absolute values of the field increments in order to avoid cancellation effects in the averaging process. All computed functions are normalized by the appropriate powers of energy

$$\hat{S}_p^{\theta,\,v}(l) \equiv \frac{S_p^{\theta,\,v}(l)}{(E^{\theta,\,\mathrm{k}})^{p/2}}. \tag{3.20}$$

The inserts show logarithmic derivatives of the corresponding structure functions, $d\ln(\hat{S}_p^{\theta,\,v})/d\ln(l)$, with horizontal dashed lines indicating the value of the most probable scaling exponents. These are determined from the shape of the logarithmic derivatives. Generally, the derivatives asymptotically form a plateau at inertial-range scales. These plateaux appear in front of a fall-off of the curves at large scales. The logarithmic derivatives approach a constant value immediately in front of this transition from inertial to large scales. This value indicates the most probable scaling exponent of the structure functions at inertial-range scales. The associated fitting procedure causes measurement errors which are estimated by the vertical extension of the plateaux.

The normalized second order velocity structure function $\hat{S}_2^v(l)$ (top left) displays a relatively large self-similar range that extends over one spatial decade from large scales down to the dissipation range. The logarithmic derivative is smooth

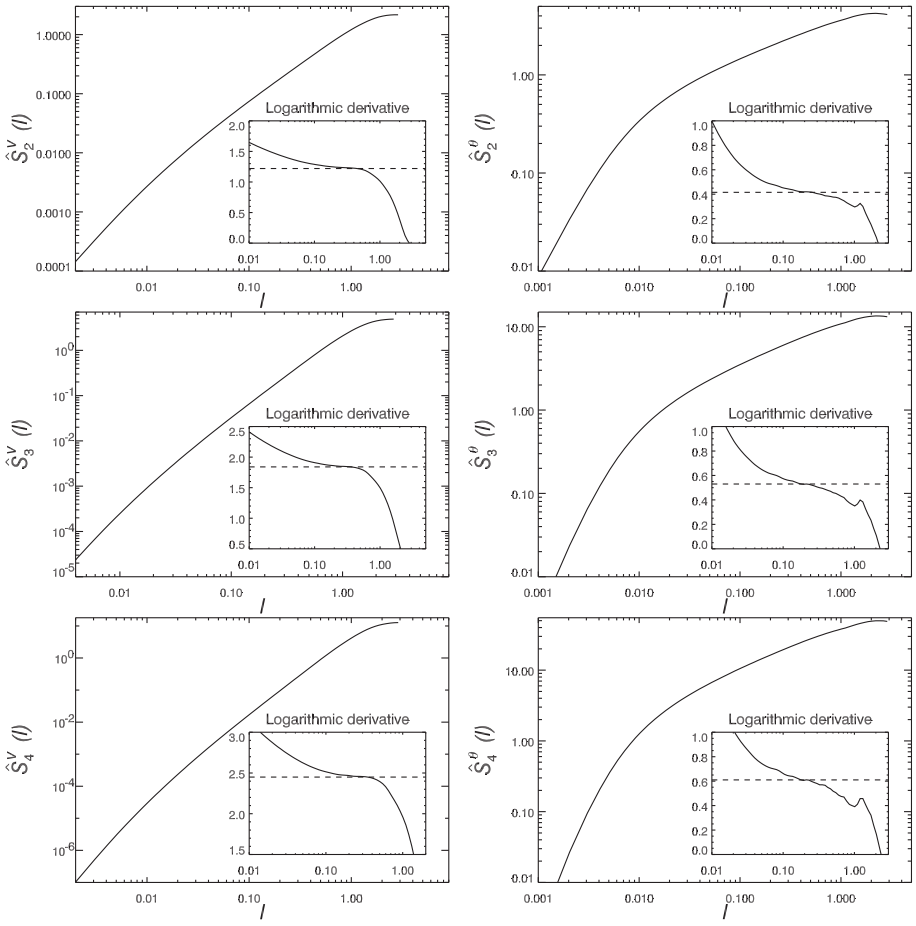

Figure 3.6: Velocity structure functions $S_p^v(l)$ (left) and temperature structure functions $S_p^\theta(l)$ (right) of order $p = 2, 3, 4$ (from top to bottom) normalized by $(E^{\theta,\,\mathrm{k}})^{p/2}$. Inserts display logarithmic derivatives of corresponding structure functions. Horizontal dashed lines indicate values of scaling exponents $\zeta_p^{v,\,\theta}$.

with a small plateau that is indicated by the horizontal dashed line. The scaling exponent is estimated to be $\zeta_2^v = 1.22 \pm 0.05$. This value is very close to the predicted BO exponent 1.2 (cf. (1.35)), and is therefore consistent with the BO scaling of the kinetic energy.

The normalized second order temperature structure function $\hat{S}_2^\theta(l)$ (top right) corresponding to the Fourier spectrum of entropy exhibits a self-similar range over one spatial decade as well. In spite of this fact, its logarithmic derivative contains a small dip at large scales. However, a small plateau indicating the most probable scaling exponent can be still identified at $0.2 \lesssim l \lesssim 0.3$ leading to $\zeta_2^\theta = 0.42 \pm 0.06$. This value is very close to the BO prediction 0.4 (cf. (1.36)), and thus suggests that the system operates in the BO regime.

The other plots show normalized velocity and temperature structure functions (left and right, resp.) of higher orders $p = 3, 4$ (middle and bottom). The functions $\hat{S}_p^v(l)$ exhibit a clear inertial range, so the scaling exponent of higher order functions can be easily determined from the inserts. They are $\zeta_3^v = 1.83 \pm 0.05$ and $\zeta_4^v = 2.45 \pm 0.07$. On the contrary, the inertial ranges of $\hat{S}_p^\theta(l)$ become shorter as the order p increases, and the logarithmic derivatives become more noisy – especially the large-scale dip is more pronounced. The scaling exponents of the temperature structure functions of orders $p = 3, 4$ are therefore determined with relatively large errors as $\zeta_3^\theta = 0.54 \pm 0.08$ and $\zeta_4^\theta = 0.61 \pm 0.1$.

Generally, it is known that due to limited sets of finite samples of data, the statistical error of calculation of structure functions increases with the order. Thus it is more difficult to determine the correct scaling exponent for higher order moments. However, these spurious features can be partially eliminated using extended self-similarity (ESS). In the next section, the concept of ESS is at first explained, and then used to determine the values of exponents of velocity and temperature structure functions more precisely.

3.5 Intermittency

Intermittency of turbulent convection is a phenomenon that affects the ideal inertial range scaling predicted by the Kolmogorov phenomenology (cf. (1.29), (1.32)) and the Bolgiano-Obukhov phenomenology (cf. (1.37), (1.38)). The original theories assume that smaller and smaller turbulent structures are space-filling and uniformly distributed in space. On the contrary, laboratory experiments and numerical simulations indicate that the distribution of small-scale structures varies rapidly in space and time (e.g. [CLM00] [BHS01][CMM02]). Small-scale structures are not space-filling, but they are spread irregularly in space. This fact inevitably leads to corrections of the inertial-range scaling predicted by both phenomenologies which assume perfect self-similarity of turbulence.

A simple way how to determine deviations from the predicted scaling is to check the behavior of higher order scaling exponents of structure functions in the inertial region. In the nonintermittent case, they scale in the inertial range as (for example velocity structure functions in the BO regime are considered)

$$S_p^v(l) \sim \langle (\delta v_l)^p \rangle \sim l^{3p/5}. \tag{3.21}$$

The departure from a nonintermittent scaling can be quantified by comparing calculated and predicted scaling exponents for individual orders p. For the estimate of higher order exponents, extended self-similarity (ESS) is widely used.

3.5.1 Extended self-similarity

Extended self-similarity is a property of structure functions to display an extended inertial range when they are plotted as functions of a reference structure function of the same field (e.g. [Fri95][Bis03]). For instance, $S_p^v(l)$ of order p can be expressed as a function of $S_q^v(l)$ of order q

$$S_p^v(l) \sim l^{\zeta_p^v} \sim \left[l^{\zeta_q^v}\right]^{\zeta_p^v/\zeta_q^v} \sim \left(S_q^v(l)\right)^{\zeta_p^v/\zeta_q^v}. \tag{3.22}$$

The most interesting observational fact is that spurious features that contaminate an inertial range are partially eliminated when applying ESS. Structure functions of the same field exhibit similar features in their shape which leads to their compensation when a high order structure function is plotted as a function of the reference structure function. Scaling exponents can be therefore more precisely determined by applying ESS. An exponent obtained by this procedure is in fact a scaling exponent relative to the reference exponent.

This feature can be further utilized when the reference scaling exponent is exactly known, e.g. from theory. In turbulent convection there is only one exact result rigorously derived from the original dynamical equations. It is Yaglom's four-thirds law that relates temperature and velocity increments in turbulent convection (e.g. [MY75][Bis03])

$$\left\langle \delta v_l (\delta\theta_l)^2 \right\rangle = -\frac{4}{3}\varepsilon_\theta l. \tag{3.23}$$

Yaglom's law is an exact relation, and describes the behavior of entropy flux. This relation is analogous to Kolmogorov's four-fifths law in hydrodynamic turbulence (e.g. [Fri95][Pop00]). The validity of Yaglom's law (3.23) in the performed simulation cannot be verified due to the limited resolution that leads to a very short self-similar range of $\left\langle \delta v_l (\delta\theta_l)^2 \right\rangle$. However, according to the obtained spectral scaling of the kinetic energy and the entropy (Fig. 3.1 and Fig. 3.2), it is possible to assume that the BO scaling holds, and relate higher order structure functions of velocity and temperature to the structure functions of the second order.

Although ESS is not rigorously proved or derived, it has been verified in a number of experimental and numerical observations (e.g. [BM00][Bis03][CCI93]).

3.5.2 Intermittency models

The relative scaling exponents of velocity structure functions ζ_p^v/ζ_2^v and temperature structure functions $\zeta_p^\theta/\zeta_2^\theta$ are determined up to the order $p = 9$ via ESS. Their values are summarized in Tab. 3.1. Fitting errors involved in the

Order p	ζ_p^v/ζ_2^v	$\zeta_p^\theta/\zeta_2^\theta$
2	1	1
3	1.48 ± 0.05	1.27 ± 0.06
4	1.94 ± 0.07	1.46 ± 0.08
5	2.39 ± 0.09	1.61 ± 0.11
6	2.82 ± 0.11	1.70 ± 0.13
7	3.23 ± 0.13	1.78 ± 0.15
8	3.65 ± 0.16	1.85 ± 0.17
9	4.10 ± 0.18	1.91 ± 0.19

Table 3.1: Relative scaling exponents of velocity and temperature structure functions in the performed simulation of 2D turbulent convection up to the order $p = 9$ obtained via ESS.

estimation of the scaling exponents are determined in an analogous way as in the case of the structure functions (see previous section). In order to obtain an estimate of importance of intermittency corrections to the nonintermittent scaling of velocity fluctuations $l^{3p/5}$ (cf. (1.35)), the relative scaling exponents of the velocity field ζ_p^v/ζ_2^v are plotted in Fig. 3.7 as a function of the order p. The measured values are denoted by diamonds. The dashed line corresponds to the nonintermittent scaling $l^{3p/5}$. Crosses are results obtained from numerical simulations of 2D turbulent convection ([BHS01], $\mathsf{Ra} \approx 10^{12}$, $\mathsf{Pr} \approx 1$).

The computed relative scaling exponents deviate only slightly from the predicted BO scaling $l^{3p/5}$, i.e. the velocity field displays only small intermittency which is significant only for values of orders $p > 6$. The calculated values coincide very well with the numerical results from [BHS01]. This fact probably originates in the similar setup of both simulations and the same applied boundary conditions. The intermittent character of the velocity field is well described with the log-Poisson model denoted by the dot-dashed line (see [Dub94]). The log-Poisson model is a phenomenological description of intermittency based on two parameters, a codimension C_0 (= (dimension of the system) − (dimension of the most intermittent structures)) and a level of intermittency β (= 1 nonintermittent, = 0 extreme intermittent case). A general expression relating the third and higher order moments in hydrodynamic turbulence is given as ([Dub94])

$$\frac{\zeta_p^v}{\zeta_3^v} = [1 - C_0(1-\beta)]\frac{p}{3} + C_0\left(1 - \beta^{p/3}\right). \tag{3.24}$$

This model with values $C_0 = 1/3$ and $\beta = 2/5$ (see [BHS01]) leads to the prediction indicated by the dot-dashed line. The numerically obtained results coincide very well with the prediction (3.24). Thus this model seems to be convenient for the description of the velocity field intermittency in 2D turbulent convection. The weakly intermittent character of the velocity field is probably a consequence of the inverse cascade of kinetic energy ([CCM04]).

The relative scaling exponents of the temperature structure functions $\zeta_p^\theta/\zeta_2^\theta$ of the performed simulation evaluated via ESS are depicted in Fig. 3.8. The measured values are denoted by diamonds. The dashed line corresponds to the nonintermittent BO scaling $l^{p/5}$ (cf. (1.36)). Crosses are results from the already mentioned work ([BHS01], $\mathsf{Ra} \approx 10^{12}$, $\mathsf{Pr} \approx 1$). Triangles stand for

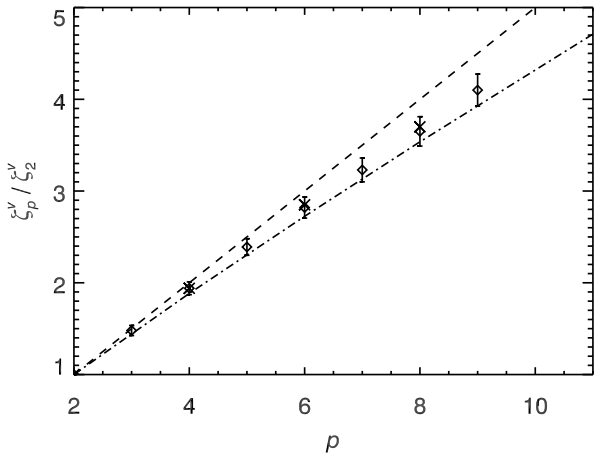

Figure 3.7: Relative scaling exponents ζ_p^v/ζ_2^v (diamonds) of velocity structure functions in the performed simulation of 2D turbulent convection. The dashed line corresponds to the nonintermittent BO scaling $l^{3p/5}$. Crosses are results from another numerical simulation of 2D turbulent convection ([BHS01]). The dot-dashed line indicates the modified log-Poisson model for hydrodynamic turbulence ([Dub94]).

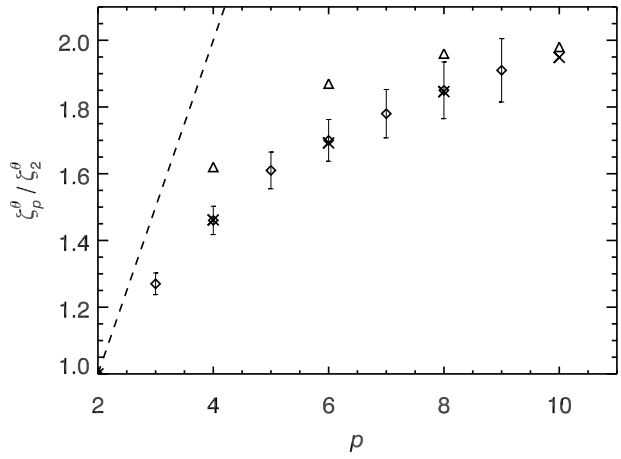

Figure 3.8: Relative scaling exponents $\zeta_p^\theta/\zeta_2^\theta$ (diamonds) of temperature structure functions in the performed simulation of 2D turbulent convection. The dashed line represents the nonintermittent scaling corresponding to $l^{p/5}$. Crosses and triangles denote results from numerical simulations of 2D turbulent convection ([BHS01] and [CMV01], resp.).

intermittency exponents obtained numerically from another simulation of 2D turbulent convection ([CMV01], $\mathsf{Ra} \approx 10^7$, $\mathsf{Pr} \approx 1$). The estimated exponents coincide well with the values given in [BHS01]. However, they differ significantly from numerical results of [CMV01] though obtained in the similar setup as in this work. The temperature field displays a far more intermittent character than the velocity field. A significant deviation from the predicted scaling is observed already for the exponent of the order $p = 3$. It seems that the higher order relative exponents tend asymptotically to a value of 2. This tendency of the computed exponents can be observed in both other numerical results as well.

The very intermittent character of the temperature field manifests itself also in the real space structure of the field. This issue is addressed in more detail in section 3.6.

3.5.3 Probability density functions

The complete set of moments of structure functions at particular scale l is statistically equivalent to the probability density function of field increments at that scale. A nonintermittent configuration of structures at scale l results in a Gaussian probability density function (pdf). On the contrary, deviations from the nonintermittent behavior can be identified as departures of pdfs from the Gaussian behavior.

In order to obtain an estimate of the departure from the Gaussian distribution, the pdfs of velocity and temperature field increments at large ($l \approx L$) and small ($l \approx 10^{-2}L$) scales are computed and plotted in Fig. 3.9. Dashed lines in all four figures denote the corresponding Gaussian pdfs with same variances. Top pictures show that the distribution of large-scale structures of both fields is almost exactly Gaussian. This means that fluctuations at different positions separated by a large distance are uncorrelated. In contrast to that, bottom pictures representing pdfs at small scales display large deviations from the Gaussian behavior, i.e. intermittently distributed small-scale fluctuations with large amplitudes are present in the flow. The computed tails of the pdfs at small scales are more pronounced in the case of temperature than in the case of velocity indicating more intermittent distribution of small-scale (dissipation) structures of temperature compared to that of velocity. This tendency is in qualitative agreement with the behavior of the relative scaling exponents in the previous section.

To obtain a quantitative view of the departures from the Gaussian behavior at all scales, the flatness (kurtosis) F of the pdfs is plotted in Fig. 3.10 as a function of scale l. The flatness is defined as the ratio of the fourth order moment to the squared second order moment

$$F(l) \equiv \frac{S_4(l)}{(S_2(l))^2}, \tag{3.25}$$

and gives peakedness and flatness of a pdf relative to the Gaussian distribution. The flatness of the Gaussian pdf is exactly $F = 3$. High values of F characterize pdfs with sharp peaks and flat tails, whereas low values identify pdfs with rounded peaks and broad shoulders. Thus the flatness F is a useful measure of intermittent features.

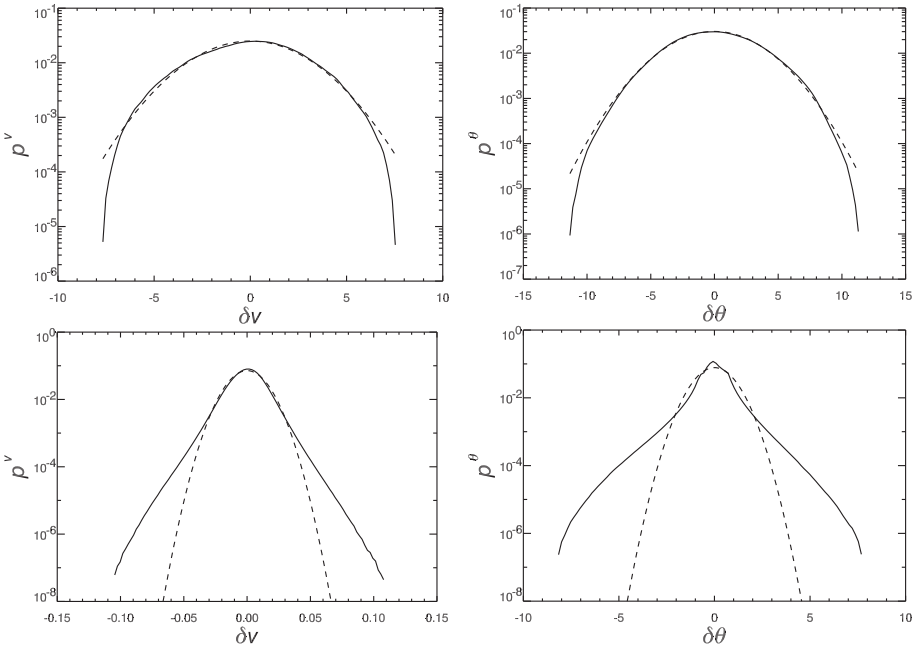

Figure 3.9: Probability density functions of velocity increments p^v (left) and temperature increments p^θ (right) at large ($l \approx L$) and small ($l \approx 10^{-2}L$) scales (top and bottom, resp.). Dashed lines denote the corresponding Gaussian pdfs with the same variance.

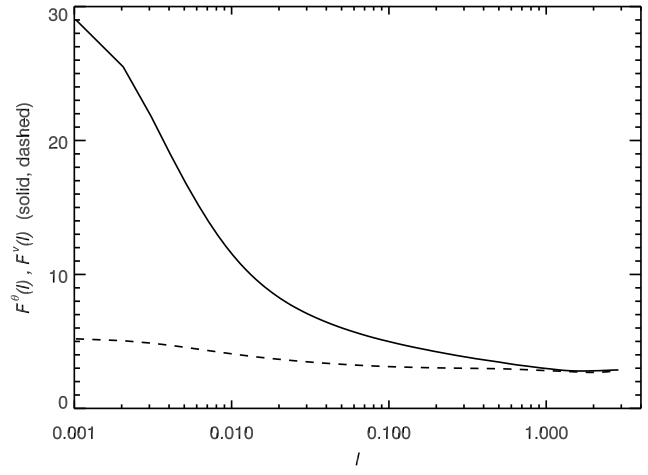

Figure 3.10: The flatness F as a function of scale l of velocity and temperature probability density functions in the performed simulation of 2D turbulent convection. The value $F = 3$ corresponds to a Gaussian distribution.

Both flatnesses $F^v(l)$ and $F^\theta(l)$ displayed in Fig. 3.10 give at large scale approximately the expected Gaussian value $F \approx 3$, but at small scales the values differ significantly. While $F^v(l)$ stays even at small scales close to the value 3, the curve of $F^\theta(l)$ deviates considerably reaching values around 30.

The computed probability density functions together with the flatness confirm the picture of increasingly sparse fluctuations with large amplitudes when going to small scales. Furthermore, the temperature field is more intermittent than the velocity field. This difference is probably caused by a distinct character of the energy cascades. While the dissipation of entropy occurs at the smallest scales, the inverse cascade of the kinetic energy tends to establish flow structures at the largest scales. This issue is further examined in the following section.

3.6 Real space structure

The real space configuration of the flow in 2D thermal convection is characterized by rising hot and descending cold parts of fluid called thermal plumes. A thermal plume is a coherent region of a fluid where the temperature is well mixed, and exhibits only small variations. This region penetrates into an area of different temperature.

Fig. 3.11 shows a characteristic snapshot of the global structure of the flow in the performed simulation. Temperature fluctuations are denoted by color (light – high values, dark – low values). The velocity is represented by vectors. On the r.h.s. of the picture two blobs of fluid can be recognized, a rising hot one in the lower part and a sinking cold one in the upper part. They move in opposite directions which results in a circular motion, partially caused by incompressibility. Generally, hot parts of the fluid tend to move upward while cold parts move downward. In contrast to fine structures of temperature fluctuations, the velocity field appears to be quite smooth. However, this is only a visual impression due to macroscopic structures; the small scales exhibit disordered motions.

This fact can be seen in the structure of the vorticity field plotted in Fig. 3.12. It displays the vorticity and the corresponding temperature field at three different levels of resolution from macroscopic to small scales. At the largest scale the vorticity appears quite uniformly distributed over the entire domain; however, the zoom reveals fine details of the field. The flow consists of moving thermal plumes. One of them can be identified in the lower right corner of the most detailed picture. The top (head) of the plume consists of two parts dominantly governed by opposite-sign vorticities.

The temperature field is very intermittent at many scales. Fig. 3.12 reveals a quite important property of the temperature field, namely ramp-and-cliff structures. Ramps are large regions of similar temperature that posses sharp contours called cliffs; in other words ramps are separated by very narrow cliffs. These sharp gradients of the temperature field are formed by shear motions of the velocity field. Due to incompressibility, shearing motions in the direction perpendicular to the local temperature gradient lead to the subsequent steeping of this gradient. In this way the sharp contours develop. This process can be observed in the bottom pictures of Fig. 3.12. For example, the sharp gradient

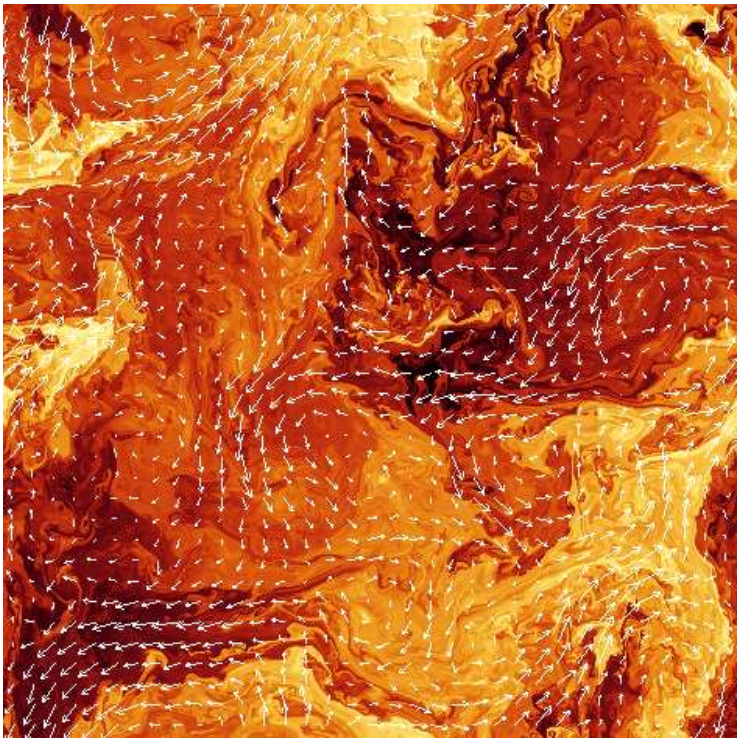

Figure 3.11: Global structure of the flow in the performed simulation of 2D turbulent convection with 4096^2 modes. Temperature fluctuations are denoted by color (light – high values, dark – low values). The velocity is represented by vectors.

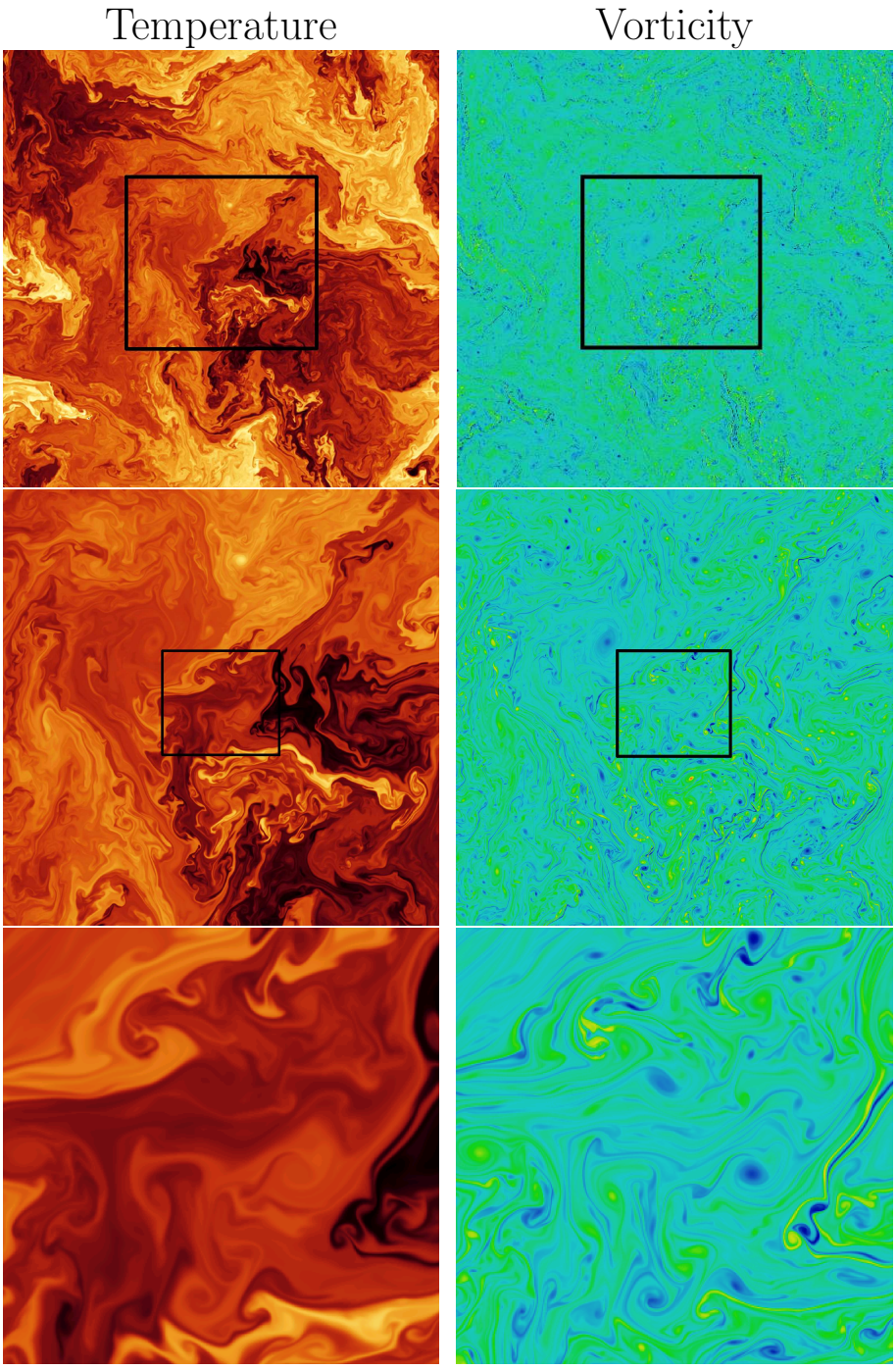

Figure 3.12: Series of zooms revealing fine structures of the temperature (left) and the vorticity field (right) in the performed simulation of 2D turbulent convection with 4096^2 modes. Values of both fields are denoted by color (light – high values, dark – low values). The most detailed pictures (bottom) demonstrate the ramp-and-cliff structure of the temperature field associated with layers of vorticity.

of the temperature close to the right border is associated with the narrow layer of the increased vorticity, i.e. with the shear motion of the flow.

The ramp-and-cliff character of temperature field was originally suggested for a passive scalar carried by a turbulent velocity field. This phenomenology seems to be more general accounting for active scalar fields as well. Thus as was suggested in several other works (e.g. [CCM04]), small-scale structures of the temperature field do not exhibit a strong dependence on the particular form of driving, e.g. by mean temperature gradient, passive advection, etc.

Chapter 4

3D hydrodynamic convection

Numerical simulations of 3D hydrodynamic convection in fully periodic domains represent a possibility to test the Bolgiano-Obukhov phenomenology directly, i.e. results of these simulations can be directly compared with theoretical predictions as well as with experimental measurements in a bulk of convective turbulence. Although the validity of the BO scaling predictions is verified in many laboratory experiments that have been conducted in tanks of various shapes, with different liquids and using different measuring techniques (e.g. [SX01][MTM04] [CCI93]), up to now the BO scaling in numerical simulations of 3D turbulent convection has not been found. This discrepancy is quite striking since the main parameter, the Rayleigh number Ra, achieved in experiments and simulations differs no more than by one or two orders of magnitude (simulations $\mathsf{Ra} \lesssim 10^9$, experiments $\mathsf{Ra} \gtrsim 10^{11}$). This situation has led to subsequent theoretical investigations, e.g. a concept of thermal plume driving ([GL92]), that would explain the observed disagreement. In addition, reliability and universality of experimental results has been discussed regarding a relation between frequency and spatial measurements, the impact of a large-scale circulation formed in laboratory tanks or influences caused by individual experimental setups and diagnostic methods. Thus results of numerical simulations that could clarify the disagreement are of special importance. Already performed 3D simulations provide only little evidence of the BO regime, which is possibly detected in boundary layers of a Rayleigh-Bénard box ([CTT02][GL91]). Several numerical works report on a discrepancy between scaling of velocity and temperature field as well (e.g. [VC03]). The purpose of the work presented in this chapter is to simulate the bulk of three-dimensional convective turbulence in fully periodic geometry, far from boundaries and without all additional modifications, e.g. hyperviscosity, and to try to detect the BO regime directly by increasing the Rayleigh number to the maximal possible value given by the applied resolution.

4.1 Ideal invariants

A system of 3D hydrodynamic convection driven by a mean horizontal temperature gradient is described by the set of dimensionless Boussinesq equations (1.16)–(1.20) reduced to the form

$$\frac{\partial \boldsymbol{\omega}}{\partial t} - \nabla \times (\mathbf{v} \times \boldsymbol{\omega}) = - \nabla\theta \times \mathbf{g}_0 + \tilde{\nu}\Delta\boldsymbol{\omega}, \tag{4.1}$$

$$\frac{\partial \theta}{\partial t} + (\mathbf{v} \cdot \nabla)\theta = \tilde{\kappa}\Delta\theta + v_x, \tag{4.2}$$

$$\nabla \cdot \mathbf{v} = 0, \quad \boldsymbol{\omega} = \nabla \times \mathbf{v}. \tag{4.3}$$

The structure of the equation governing dynamics of temperature fluctuations (4.2) is the same as in two dimensions (cf. (3.2)). On the contrary, the nonlinearity in the vorticity equation (4.1) contains a vortex-stretching term $(\boldsymbol{\omega} \cdot \nabla)\mathbf{v}$ that modifies the nonlinear transport of kinetic energy. The vorticity field is stretched in the direction parallel to velocity gradients. This process together with incompressibility and angular momentum conservation leads to the increase of vorticity. Hence the vortex-stretching term is responsible for the amplification of vorticity in three-dimensional hydrodynamics. In thermal convection, this is not the only source of vorticity since it can be generated also by temperature gradients (the first term on the r.h.s. of (4.1)) in the same way as in two dimensions, leading to the increase of vorticity at the sharp fronts of thermal plumes. Thus enstrophy (see (3.5)) is not conserved in the limit of negligible viscosity. Also the kinetic helicity $\int_V \mathbf{v} \cdot \boldsymbol{\omega} dV$, where V is the volume of the fully periodic domain, is not conserved in the case of 3D turbulent convection in contrast to the non-dissipative limit of pure hydrodynamics.

Two ideal invariants can be found by neglecting dissipation effects in the set of equations (4.1)–(4.3): the total entropy of the system and the total mechanical energy. The conservation of the total entropy $\int_V T^2 dV$, where $T = T_0 + \theta$ and T_0 is the background linear temperature profile, follows from the temperature equation (4.2) in the case of zero thermal diffusivity, remembering that the source term of temperature fluctuations originates in the mean temperature gradient (cf. (1.12), (1.5)). The total mechanical energy $\int_V \rho_0 \left(\frac{1}{2}v^2 + \mathbf{g} \cdot \mathbf{r}T\right) dV$ is in the case of zero viscosity conserved as well. The second term in this expression represents the potential energy of the system (e.g. [Lvo91]).

The Bolgiano-Obukhov phenomenology predicts a self-similar inertial-range scaling of velocity and temperature fluctuations. These expectations are based on the conservation property characteristic for the nonlinear interactions in the inertial range. The nonlinear interactions are the main agent responsible for the cascade of the kinetic and temperature energy. The additional terms on the r.h.s. of (4.1)–(4.3) represent sources of fluctuations, so they do not participate directly in the nonlinear interactions.

Results presented in the following sections are obtained from the simulation of the system (4.1)–(4.3) in a periodic cubic domain with the resolution 1024^3. Dissipation coefficients are chosen as $\tilde{\nu} = 6 \cdot 10^{-4}$ and $\tilde{\kappa} = 9 \cdot 10^{-4}$ in order to obtain the maximal extension of both inertial ranges. The nominal Rayleigh number of this run is $\mathsf{Ra} \approx 2 \cdot 10^7$, and the Reynolds number achieved in the

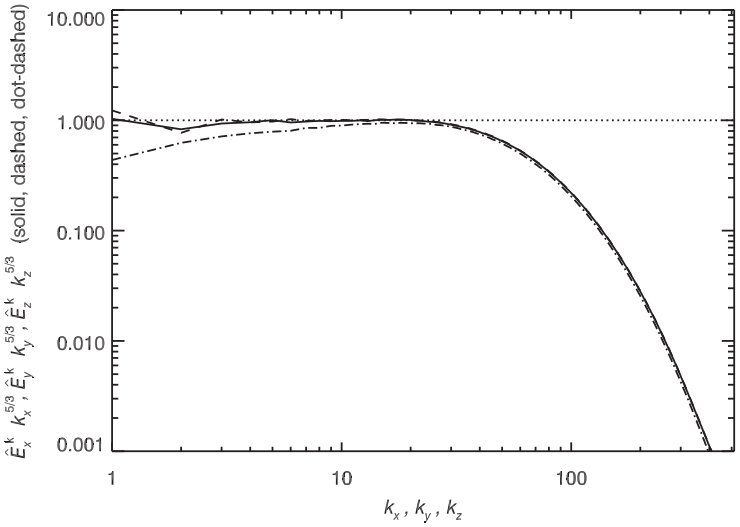

Figure 4.1: Time-averaged one-dimensional kinetic energy spectra $E^{\mathrm{k}}_{x,y,z}$ normalized by $\varepsilon_v^{2/3}$ and compensated by the factor $k^{5/3}$. The horizontal dotted line indicates Kolmogorov scaling $k^{-5/3}$. The spectra exhibit the Kolmogorov scaling for about one decade in wavenumber. The vertical kinetic energy spectrum is somewhat flatter, i.e. the system displays a slight anisotropy.

simulation is $\mathsf{Re} \approx 2 \cdot 10^3$. The system is evolved for approximately 6.6 typical buoyancy times.

4.2 Energy spectra

The one-dimensional kinetic energy spectra (y,z directions analogously)

$$E^{\mathrm{k}}_x(k_x) \equiv \int_{\forall k_y,\, k_z} E^{\mathrm{k}}(\mathbf{k}) dk_y dk_z \tag{4.4}$$

obtained from the performed simulation by time-averaging over 6 typical buoyancy times are depicted in Fig. 4.1. The spectra are normalized by $\varepsilon_v^{2/3}$ (cf. (1.29)) and compensated by the scaling factor $k^{5/3}$. The horizontal dotted line indicates Kolmogorov scaling $k^{-5/3}$. The spectra display an inertial interval of approximately one decade in wavenumber. The horizontal spectra in both directions coincide well with the Kolmogorov scaling. The vertical kinetic energy spectrum is slightly flatter in the inertial range, i.e. a small level of anisotropy introduced by gravity penetrates through the inertial range though reduced, up to the beginning of the dissipation range ($k \approx 25$) where isotropy is restored again. The nonlinear turbulent mixing in the inertial region reduces the large-scale anisotropy introduced at the largest scales.

The detected Kolmogorov scaling suggests that despite the large numerical resolution (1024^3) and the relatively high Rayleigh number achieved ($\mathsf{Ra} \approx 2 \cdot 10^7$), the system operates in the Kolmogorov regime that is typical for hydrodynamic

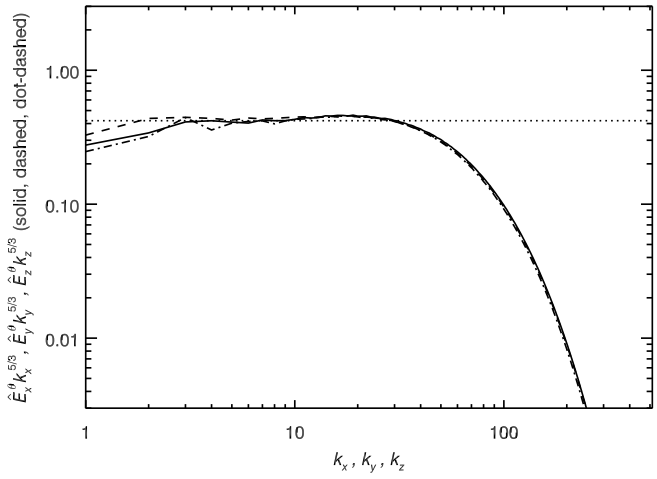

Figure 4.2: Time-averaged one-dimensional temperature energy spectra $E^{\theta}_{x,y,z}$ normalized by $\varepsilon_\theta \varepsilon_v^{-1/3}$ and compensated by the factor $k^{5/3}$. The horizontal dotted line indicates the scaling $k^{-5/3}$. The inertial interval extends over approximately one decade.

turbulence and turbulent convection with low and moderate Rayleigh numbers. This fact is in agreement with the computed Bolgiano wavenumber that determines the scale where the transition between the Kolmogorov and the BO regime occurs. The evaluated Bolgiano wavenumber $k_\mathrm{B} \approx 1.5$ is located approximately at the largest resolved scale.

The Bolgiano scale is given by the kinetic and the temperature dissipation rates (cf. (1.25)). This fact explains the observed difference between scaling properties of convective systems in 2D and 3D. While the kinetic energy in 2D undergoes an inverse cascade in the inertial range, and consequently the small-scale energy dissipation rate is relatively low, the kinetic energy in 3D is transferred from large to small scales, so the energy dissipation rate is much higher. The temperature energy is in both cases subject to a direct cascade, and the thermal dissipation rates assume in both performed simulations a similar value. Therefore, the Bolgiano wavenumber in the 3D simulation is located at larger spatial scales than in the 2D simulation. The dissipation range is well resolved since $k_\mathrm{d} \approx 243$ where k_d is the Kolmogorov dissipation wavenumber defined as (cf. (3.8))

$$k_\mathrm{d} = \left(\frac{\varepsilon_v}{\tilde{\nu}^3}\right)^{1/4}. \tag{4.5}$$

The time-averaged one-dimensional temperature energy spectra obtained from the same run are depicted in Fig. 4.2. The spectra are normalized by the factor $\varepsilon_\theta \varepsilon_v^{-1/3}$ (cf. (1.32)) and compensated by the scaling factor $k^{5/3}$. The horizontal dotted line indicates the scaling $k^{-5/3}$. The inertial interval extends over approximately one decade. In contrast to the kinetic energy spectra shown in Fig. 4.1, the temperature energy spectra are in the inertial interval rather

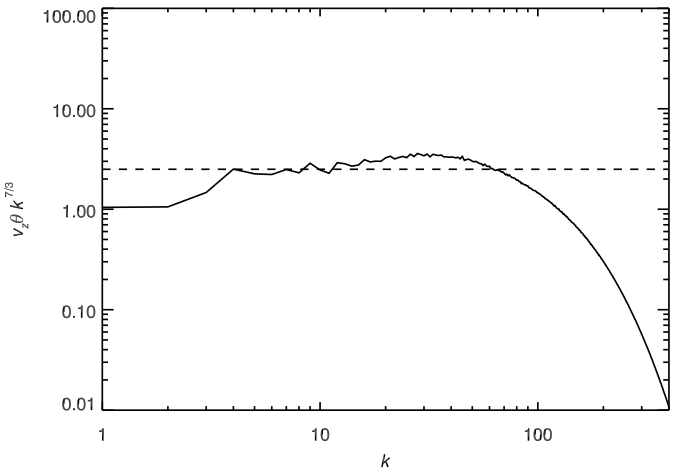

Figure 4.3: The time-averaged spectrum of the vertical heat flux $v_z\theta$ compensated by the scaling factor $k^{7/3}$. The spectrum is normalized by the factor $\varepsilon_\theta \varepsilon_v^{-2/3}$ (cf. (4.7)). The horizontal line indicates the scaling $k^{-7/3}$. The vertical heat flux spectrum displays a similar bump as in the 2D case (Fig. 3.3).

isotropic. The detected Kolmogorov-like scaling exponent, typical for spectra of passively advected scalars (e.g. [Les97][Bis03]), confirms that the system operates in the Kolmogorov regime of turbulent convection.

The second half of the inertial range exhibits a small bump that deteriorates the scaling slightly. The shape of this part is very similar to the bump in the temperature energy spectrum of the two-dimensional run (Fig. 3.2) that displays a similar pattern. The system experiences a bottleneck-like effect at the transition between the inertial and the dissipation range although no hyperviscosity is used. The same tendency can be observed in the vertical heat flux spectrum shown in Fig. 4.3. The system is adequately resolved with the temperature dissipation wavenumber $k_\mathrm{d}^\theta = (\varepsilon_v/\tilde{\kappa}^3)^{1/4} \approx 187$ (e.g. [Bis03]) which is relatively close to the kinetic energy dissipation scale k_d. This configuration is a result of the Prandtl number $\mathsf{Pr} = \tilde{\nu}/\tilde{\kappa} \approx 0.66$ being close to 1. It is interesting that a similar bump was also observed in energy spectra obtained from numerical simulations that use a distinct numerical solver based on finite differences ([HB06]). Thus the presence of the bump seems to be independent of applied numerical schemes. Furthermore, this effect is less pronounced in one-dimensional spectra compared to angle-integrated spectra. Thus the bump might be either a physical phenomenon or a generic feature caused by limited resolutions applied in numerical simulations. The discretization onto computational grid restricts interactions between turbulent fluctuations to limited number of spectral modes compared to many degrees of freedom available in real turbulent flows.

In Fig. 4.3 the time-averaged spectrum of the vertical heat flux is shown. The spectrum is compensated by the scaling factor $k^{7/3}$ and normalized by $\varepsilon_\theta \varepsilon_v^{-2/3}$ (see later (4.7)). The horizontal line indicates the scaling $k^{-7/3}$. In this case,

the identification of an inertial region is more difficult and unclear than in the previous spectra. The scaling $k^{-7/3}$ is only the best fit for the wavenumber range $4 \lesssim k \lesssim 12$, but it can be justified following similar arguments as in the 2D case (cf. (3.10) and [GL93]) leading to

$$(v_z\theta)_l \sim \alpha g \theta_l^2 v_l^{-1} l. \tag{4.6}$$

In the Kolmogorov regime of convection, this relation together with scaling predictions for velocity and temperature fluctuations at inertial-range scales (see (1.28), (1.31)) gives ([GL93])

$$(v_z\theta)_l \sim (\alpha g)\varepsilon_\theta \varepsilon_v^{-2/3} l^{4/3} \quad \Rightarrow \quad (v_z\theta)_k \sim (\alpha g)\varepsilon_\theta \varepsilon_v^{-2/3} k^{-7/3}. \tag{4.7}$$

It is pointed out ([GL93]) that in the Kolmogorov regime the vertical heat flux should depend on the buoyancy factor (αg), otherwise the picture would be inconsistent with the case $(\alpha g) \to 0$. The presence of the bump in the spectrum is probably related to the same feature in the entropy spectrum (Fig. 4.2).

Another numerical work ([VC03]) also reports about similar difficulties by identification of scaling exponents of the entropy spectrum. The discrepancy of the scaling behavior due to the presence of a bottleneck-like bump is interpreted there as the BO scaling of entropy fluctuations $k^{-7/5}$ (this exponent is close to the Kolmogorov value $-5/3$, the difference is only $5/3 - 7/5 = 4/15 \approx 0.27$), leading to a new mixed regime where velocity field and temperature field follow Kolmogorov and Bolgiano-Obukhov predictions, respectively. In this work it is suggested that both entropy spectra (Fig. 4.2 and in [VC03]) are well explained by Kolmogorov scaling to which the large-scale part of the inertial interval tends. This view is supported not only by the computed spectra of the entropy and the vertical heat flux, but also by the estimated Bolgiano length ($k_\mathrm{B} \approx 1.5$) and other results, e.g. by measured relative exponents of structure functions (see later in section 4.4). This interpretation keeps the picture of turbulent convection consistent with available phenomenological predictions.

It is worth mentioning that a very similar bottleneck-like effect is also found in one of the largest simulations of homogeneous hydrodynamic turbulence ([KIY03]). However, there the dissipation fall-off of the kinetic energy spectrum is only about one decade. This implies that the energy content of the smallest eddies is around 10% of energy of inertial-range eddies. According to the behavior of the bump in the presented simulations (cf. Fig. 3.3), it is supposed that such a dissipation fall-off is too small. A bottleneck-like bump in a spectrum can result in a slightly steeper slope of that spectrum at larger inertial-range scales.

4.3 Nonlinear transport

4.3.1 Transfer functions

An analysis of the nonlinear transport of the kinetic energy and the entropy by a computation of transfer functions can help to identify if the system indeed operates in the Kolmogorov regime of turbulent convection or not. The kinetic

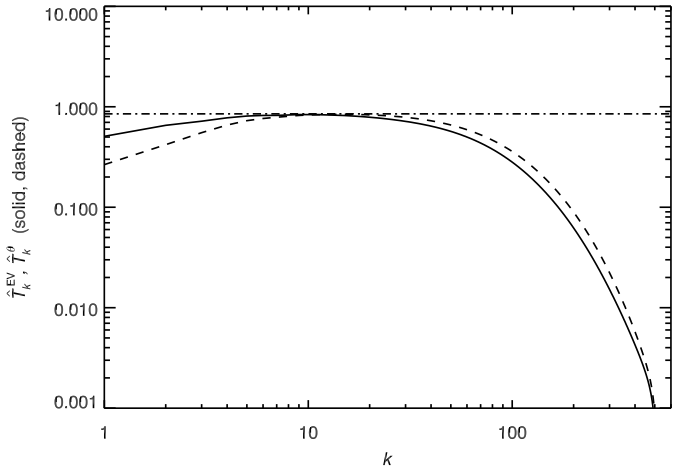

Figure 4.4: The kinetic energy transfer function $\hat{T}_k^{\mathrm{EV}}$ (solid) and the entropy transfer function $\hat{T}_k^{\theta}$ (dashed) in the Kolmogorov regime of turbulent convection. Both transfer functions are normalized by the corresponding dissipation rates, ε_v and ε_θ (cf. (4.8) and (4.9)).

energy and the entropy transfer function, $\hat{T}_k^{\mathrm{EV}}$ and $\hat{T}_k^{\theta}$ (cf. (3.12), (3.13)), are depicted in Fig. 4.4. They are normalized by the corresponding dissipation rates, ε_v and ε_θ. Both transfer functions are positive at all scales, i.e. the kinetic energy and the entropy are transported by direct cascades from large to small scales. In the inertial region, where neither sources nor sinks of energy are important, both transfer functions approach the constant value of 1. This means that the whole amount of the transported quantity is eventually dissipated by small-scale viscosity and thermal diffusivity. This fact is in agreement with the Kolmogorov picture because

$$\epsilon_v \sim \frac{v_l^2}{\tau_l} \sim \frac{v_l^3}{l} \quad \overset{(1.28)}{\Longrightarrow} \quad T_k^{\mathrm{EV}} \sim \text{const.} \tag{4.8}$$

and

$$\epsilon_\theta \sim \frac{\theta_l^2}{\tau_l} \sim \frac{\theta_l^2 v_l}{l} \quad \overset{(1.31)}{\Longrightarrow} \quad T_k^{\theta} \sim \text{const.} \tag{4.9}$$

Both inertial ranges in the plot are very short, confirming difficulties with resolving inertial-range scales of the three-dimensional flow sufficiently. The difficulties with applied resolution are caused by limited computational resources and consequently by the moderate values of the Reynolds number, $\mathsf{Re} \approx 2 \cdot 10^3$, compared to real turbulent flows, $\mathsf{Re} \gg 10^3$. A more detailed examination reveals that the kinetic energy cascade begins at larger scales than the entropy cascade while the entropy cascade penetrates to smaller scales compared to the kinetic energy cascade.

According to the presented results, the system operates in the Kolmogorov regime of convection, i.e. temperature fluctuations are only passively advected by the velocity. However, it is possible to demonstrate by simple considerations

a few implications that would be caused by the BO regime of 3D turbulent convection. In 3D hydrodynamic convection, the kinetic energy is subject to a direct cascade, and is transferred from large to small scales. Additionally, the vertical heat flux drives convective motions at many scales, i.e. it supplies the energy to the kinetic energy cascade. This implies that the kinetic energy flux should increase towards small scales (cf. section 3.3). This situation corresponds to an increasing spectrum of the kinetic energy flux, i.e. a spectrum with a positive exponent. However, this is a contradiction to the derived scaling of the kinetic energy flux in the frame of the BO phenomenology (see (3.14)). The predicted scaling (3.14) is derived only by dimensional arguments, and is verified in 2D simulations and 3D Rayleigh-Bénard laboratory experiments. The other possibility is that the vertical heat flux assumes negative values in the inertial range, whereas its total amount remains positive, i.e. it still drives convective motions. This fact leads to a setup where the vertical heat flux in the inertial range extracts energy from the kinetic cascade, and thus has a stabilizing effect. Also this configuration seems to be physically improbable, or at least has not been indicated by laboratory or numerical experiments. Therefore, it is still not clear which mechanisms cause the experimentally observed BO regime of 3D hydrodynamic convection (cf. [Bra92][GL93]).

4.3.2 Shell to shell transfer

Similarly to the 2D case, it is possible to observe in detail if the entropy transport occurs locally in spectral space, or is influenced by nonlocal interactions. The detailed shell to shell entropy transfer in the inertial region is shown in Fig. 4.5. The definition of the transfer function is analogous to the 2D case (see (3.17)). The picture represents the spectral transfer for four different shells in Fourier space, $Q = 20, 30, 40, 50$, that are chosen close to the inertial interval, $3 \lesssim k \lesssim 30$. The plot suggests that the entropy is transferred by a direct cascade from large to small scales. The majority of the entropy is transported locally between neighboring shells. However, contributions to the transfer due to the shells $K \leq Q - 10$ and $K \geq Q + 10$ are not as small as in the 2D case, so they cannot be neglected. Thus nonlocal contributions to the spectral transfer of entropy in the Kolmogorov regime of thermal convection play a minor but still not negligible role.

A similar analysis for the kinetic energy transport would not be easy to interpret due to the same reason as in the 2D case, i.e. it is not possible to identify source shells uniquely in detailed nonlinear interactions of the velocity field (see section 3.3).

4.4 Structure functions

Structure functions offer a valuable insight into scaling properties of turbulent fields. Their particular form used in this work has been already introduced in section 3.4. Structure functions of the velocity $\hat{S}_p^{\mathrm{v}}(l)$ and of the temperature field $\hat{S}_p^{\theta}(l)$ of orders $p = 2, 3, 4$ obtained from the performed simulation of 3D turbu-

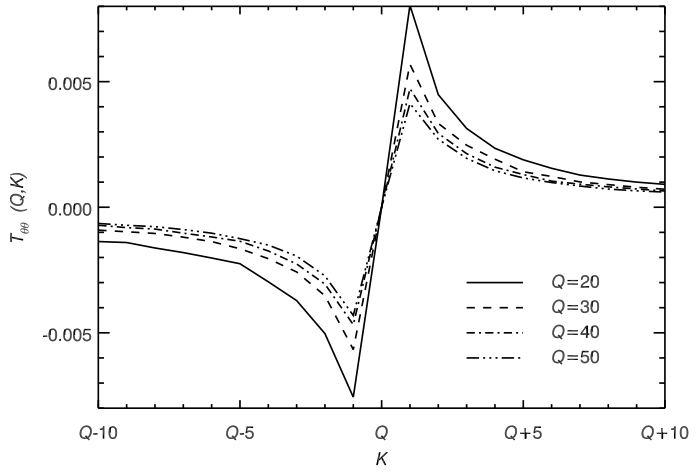

Figure 4.5: The entropy transfer $T_{\theta\theta}(Q, K)$ between different shells in Fourier space. The shells are chosen from the entropy inertial region. The entropy in the Q shell is redistributed during the interaction with the velocity field over neighboring K shells. The spectral transfer of entropy in the Kolmogorov regime of thermal convection is direct and predominantly local.

lent convection exhibit a self-similar interval at inertial-range scales. They are depicted in Fig. 4.6. The structure functions are computed by time-averaging over 6 typical buoyancy times. Moreover, they are normalized according to relation (3.20). The structure functions of odd orders are computed from absolute values of increments, e.g. $\langle|\delta v(l)|^p\rangle$. Inserts in individual figures display the corresponding logarithmic derivatives. Horizontal dashed lines indicate values of the most probable scaling exponents $\zeta_p^{v,\,\theta}$ (cf. section 3.4).

The velocity structure function of second order $\hat{S}_2^{\rm v}(l)$ exhibits a self-similar behavior over about one spatial decade. Its logarithmic derivative is smooth, and displays a wide plateau at intermediate scales. The horizontal dashed line indicates the best fit to the flat part, and yields the scaling exponent $\zeta_2^v = 0.73{\pm}0.03$. This is slightly more than the expected Kolmogorov exponent 0.66, but the estimated error range (cf. section 3.4) allows to exclude the BO value 1.2.

The second order temperature structure function $\hat{S}_2^\theta(l)$ shows a self-similar behavior as well. Although the extension of the plateau in the plot of the logarithmic derivative is somewhat shorter, the scaling exponent can be determined quite accurately leading to $\zeta_2^\theta = 0.6 \pm 0.06$. In contrast to ζ_2^v, this value is little bit smaller than the expected exponent 0.66. However, the value 0.66 is very close to the estimated error range. Hence the second order structure functions are in qualitative agreement with observed scaling of the kinetic and the temperature energy, so they confirm that the investigated system operates in the Kolmogorov regime of turbulent convection.

The scaling exponents of orders $p = 3, 4$ of velocity structure functions can be evaluated as well. They are estimated as $\zeta_3^v = 1.06 \pm 0.06$ and $\zeta_4^v = 1.38 \pm$

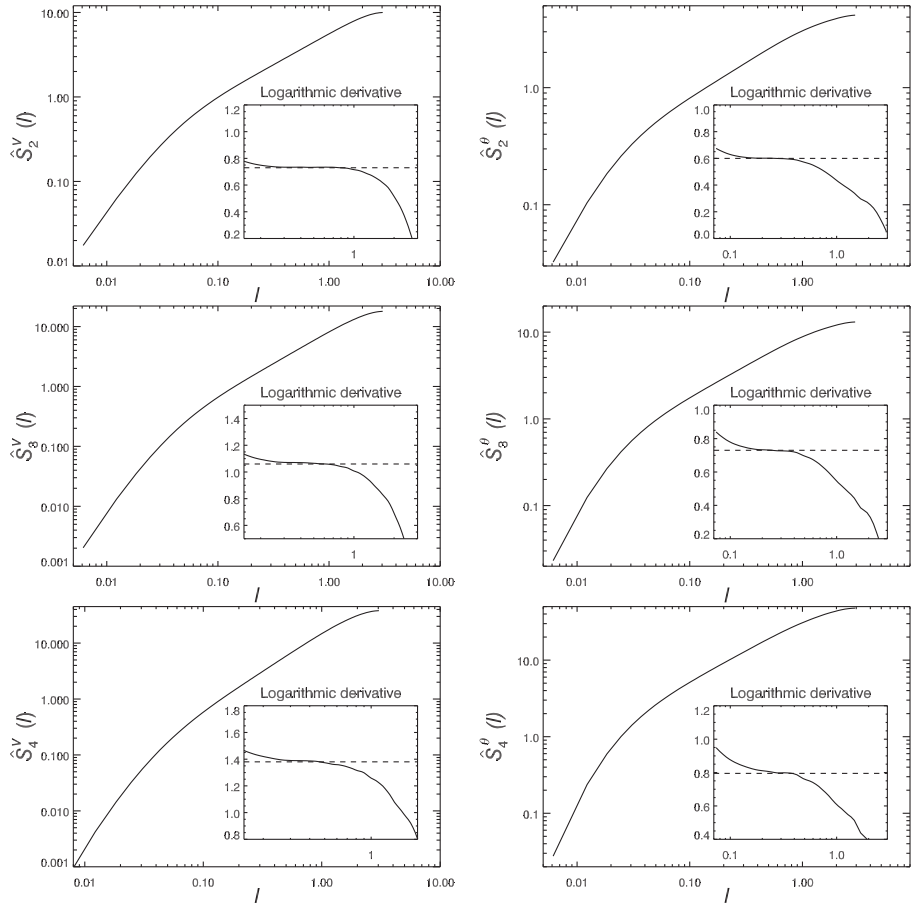

Figure 4.6: Velocity structure functions $\hat{S}_p^{\rm v}(l)$ (left) and temperature structure functions $\hat{S}_p^{\theta}(l)$ (right) of order $p = 2, 3, 4$ (from top to bottom) in the Kolmogorov regime of 3D turbulent thermal convection. Structure functions are normalized by appropriate powers of energies, $(E^{\rm k,\,\theta})^{p/2}$. Inserts show their logarithmic derivatives. Dashed lines indicate the most probable value of scaling exponents $\zeta_p^{v,\,\theta}$.

Order p	ζ_p^v/ζ_2^v	$\zeta_p^\theta/\zeta_2^\theta$
2	1	1
3	1.46 ± 0.05	1.25 ± 0.07
4	1.91 ± 0.06	1.39 ± 0.08
5	2.29 ± 0.08	1.53 ± 0.10
6	2.68 ± 0.11	1.61 ± 0.13

Table 4.1: Relative scaling exponents of the velocity and the temperature structure functions in the performed simulation of 3D turbulent convection up to the order $p = 6$ obtained via ESS.

0.08. The logarithmic derivatives of temperature structure functions despite the considerably shorter plateaux allow to determine the scaling exponents of $\hat{S}_3^\theta(l)$ and $\hat{S}_4^\theta(l)$ as $\zeta_3^\theta = 0.73 \pm 0.07$ and $\zeta_4^\theta = 0.78 \pm 0.1$, respectively.

The comparison of higher orders scaling exponents of the velocity and the temperature field suggests that the exponents ζ_p^θ increase slower than ζ_p^v, indicating more intermittent character of the temperature field. This topic is addressed in the following section.

4.5 Intermittency

4.5.1 Intermittency models

In order to obtain an estimate of intermittency effects in 3D convective turbulence, relative scaling exponents of the structure functions up to the sixth order are determined. The relative exponents are obtained using extended self-similarity (ESS) introduced in subsection 3.5.1. ESS is verified to hold and helps to determine higher order scaling exponents of the structure functions more accurately. Values of the computed relative exponents are listed in Tab. 4.1.

In Fig. 4.7 the relative scaling exponents ζ_p^v/ζ_2^v of the velocity structure functions are plotted as a function of order p. They are denoted by diamonds. The dashed line represents the nonintermittent scaling corresponding to the Kolmogorov prediction $l^{p/3}$ (cf. (1.28)). The exponents plotted in the picture deviate from the nonintermittent scaling. This behavior is known from studies of homogeneous hydrodynamic turbulence (e.g. [Fri95][Les97]). Since the convective system operates in the Kolmogorov regime, it is reasonable to assume that the intermittency of the velocity field can be described by the hydrodynamic She-Lévêque model (e.g. [Bis03])

$$\zeta_p^{\mathrm{SL}} = \frac{p}{9} + 2\left[1 - \left(\frac{2}{3}\right)^{p/3}\right]. \tag{4.10}$$

The prediction of the She-Lévêque model is represented in the plot by the dot-dashed line. The plot shows that this prediction is in acceptable agreement with the obtained values, indicating that the velocity field in 3D turbulent convection with low and moderate Reynolds number exhibits a similar level of intermittency

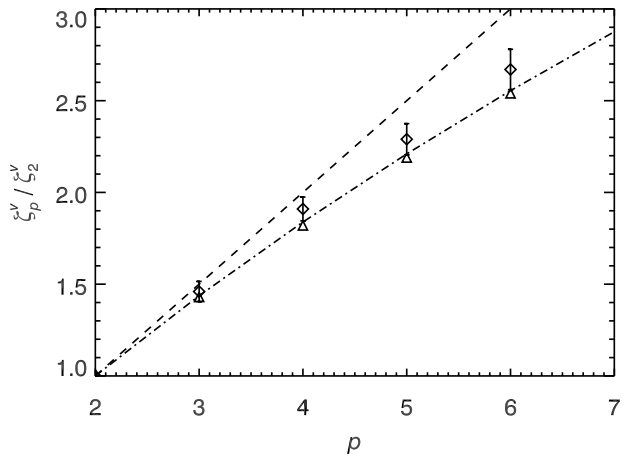

Figure 4.7: Relative scaling exponents ζ_p^v/ζ_2^v (diamonds) of the velocity structure functions obtained from the simulation of 3D convective turbulence up to the sixth order as a function of order p. The dashed line corresponds to the nonintermittent scaling $l^{p/3}$ (cf. (1.28)). The dot-dashed line indicates the prediction of the hydrodynamic She-Lévêque model. Triangles denote measurements in wind tunnel turbulence ([RBC96]).

as in homogeneous hydrodynamic turbulence despite the specific way of driving. The mean temperature gradient does not influence the nonlinear dynamics of the Kolmogorov regime of turbulent convection. Nonlinear interactions dominate the cascade process, i.e. buoyancy is negligible at inertial-range scales ($k_\mathrm{B} \approx 1.5$). This picture is supported by the fact that the obtained exponents coincide approximately with measurements in wind tunnel turbulence ([RBC96], $\mathsf{Re} \approx 4.5 \cdot 10^5$, $\mathsf{Pr} \approx 1$) denoted in the plot by triangles.

The relative scaling exponents $\zeta_p^\theta/\zeta_2^\theta$ of the temperature structure functions are depicted in Fig. 4.8. The dashed line corresponds to the nonintermittent passive scalar scaling $l^{p/3}$ (cf. (1.31)). Crosses denote measurements of temperature fluctuations advected by a wind tunnel turbulence ([RBC96], $\mathsf{Re} \approx 4.5 \cdot 10^5$, $\mathsf{Pr} \approx 1$). Triangles refer to numerical results of randomly advected passive scalar field ([CK98], $\mathsf{Re} \approx 10^5$, $\mathsf{Pr} \approx 1$). In spite of large differences between the numerically obtained exponents, all of them deviate strongly from the nonintermittent scaling. According to the estimated error ranges, the values computed in this work suggest the largest intermittency deviations. An interesting question is a comparison of these results with the intermittency of the active scalar in 2D convection (Fig. 3.8 and Tab. 3.1). The relative exponents approach a value of 2 in the 2D active scalar case. The exponents obtained numerically in [CK98] are larger than this value, whereas the exponents obtained in this work and in the wind tunnel measurements tend to this value. However, this should be understood only as an approximate relation between the exponents since a direct comparison of both cases is problematic due to different physical processes underlying 2D and 3D turbulent convection.

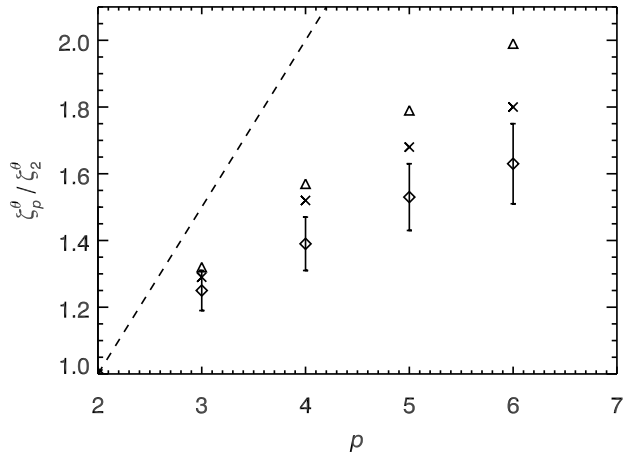

Figure 4.8: Relative scaling exponents $\zeta_p^\theta/\zeta_2^\theta$ (diamonds) of the temperature structure functions obtained from the simulation of 3D convective turbulence up to the sixth order as a function of order p. The dashed line corresponds to the nonintermittent passive scalar scaling $l^{p/3}$ (cf. (1.31)). Crosses denote temperature fluctuations measurements in wind tunnel turbulence ([RBC96]). Triangles stand for numerical results of 3D passive scalar advection ([CK98]).

4.5.2 Probability density functions

Intermittency of 3D turbulent convection can be analyzed by comparing probability density functions (pdfs) at different scales. The upper pictures in Fig. 4.9 show pdfs of velocity and temperature increments at large scales ($l \approx L$). The curves coincide well with the corresponding Gaussian pdfs with the same variance denoted by dashed lines, except for small deviations in tails that are more pronounced in the case of the temperature field. They are caused by the averaging process. The investigated system is evolved for approximately 6.6 typical buoyancy times which is not sufficient to eliminate all statistical fluctuations at large scales. Convective flows exhibit fluctuations at large scales which are related to the formation and the evolution of large-scale thermal plumes, and therefore these flows need to be evolved longer than e.g. isotropically forced homogeneous turbulent systems.

The small-scale ($l \approx 10^{-2}L$) probability density functions are depicted in the bottom part of Fig. 4.9. The pdfs of both fields deviate from the Gaussian profiles considerably. The deformation of the tails of the pdfs is more pronounced in the case of the temperature field. This fact is in agreement with the character of the measured scaling exponents.

The flatness parameter (3.25) defined in section 3.5.3 is used to quantify the deviation of the pdfs from Gaussian distribution ($F = 3$) at different spatial scales. The flatness for both fields is plotted in Fig. 4.10. The values of F are close to 3 at large scales, indicating Gaussian character of both fields, i.e.

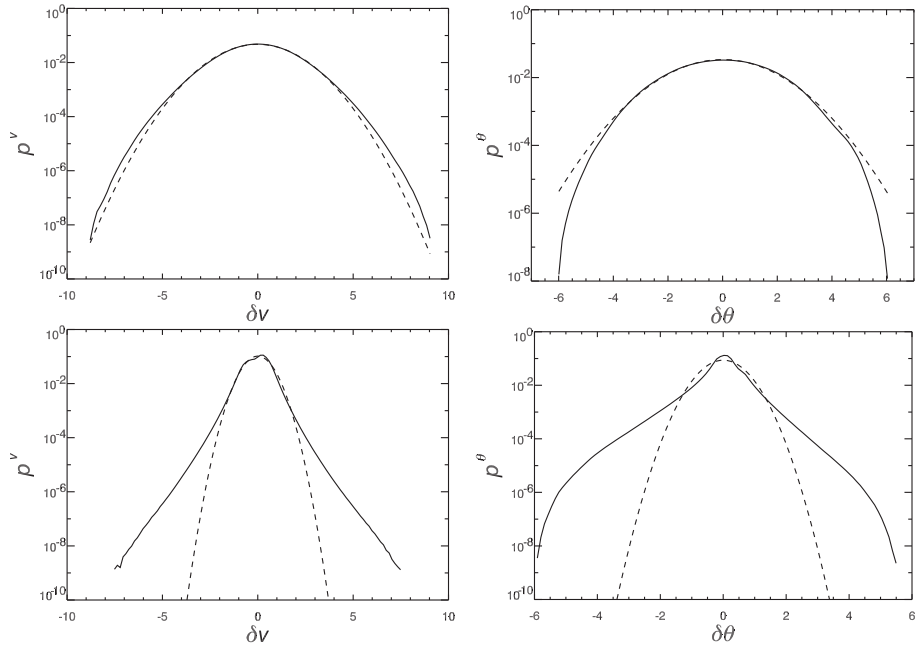

Figure 4.9: Probability density functions p^v (left) and p^θ (right) of velocity increments and temperature increments, respectively, at large ($l \approx L$) and small ($l \approx 10^{-2}L$) scales (top and bottom, resp.) obtained from the simulation of 3D turbulent convection. Dashed lines denote the corresponding Gaussian pdfs with the same variance.

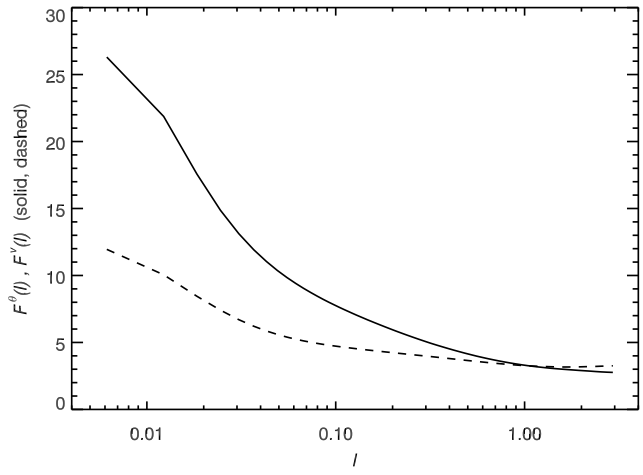

Figure 4.10: The flatness F as a function of scale l of velocity and temperature probability density functions in the simulation of 3D turbulent convection. The flatness of the pdfs of both fields approaches at large scales the Gaussian value ($F \approx 3$).

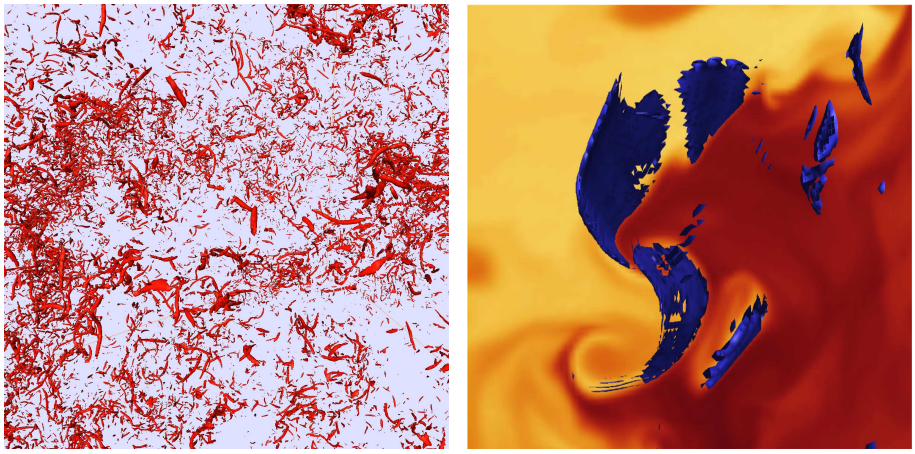

Figure 4.11: Left: Isosurfaces of the most intense vorticity in the form of quasi-one-dimensional filaments. Right: Three-dimensional picture of high thermal dissipation associated with sharp transitions between regions of significantly different temperatures. The background slice displays the structure of temperature fluctuations (light – high values, light – low values). The three-dimensional blue isosurfaces indicate places of intensive thermal dissipation.

fluctuations at large scales are spatially uncorrelated and uniformly distributed. The difference between both fields at small scales is evident. While the velocity field is only slightly intermittent ($F^v \approx 12$), the flatness of the temperature field is very large ($F^\theta \approx 27$), suggesting a strongly irregular distribution of temperature fluctuations with large amplitudes at small scales. Comparing these curves with the flatnesses in the 2D case (cf. Fig. 3.10), the velocity field is in the 3D case more intermittent, which is caused by the direct character of the kinetic energy cascade and larger small-scale dissipation. The active temperature field in the 2D case exhibits approximately the same level of intermittency as the passive temperature field in the 3D case, suggesting a robust character of the entropy cascade, i.e. an independence on other dynamical processes, e.g. the kinetic energy cascade.

4.5.3 Dissipative structures

The scaling of the relative exponents of the velocity field, which is in approximate agreement with the hydrodynamic She-Lévêque model (see Fig. 4.7), suggests that dissipative eddies of the velocity field have a similar spatial shape and structure as in homogeneous hydrodynamic turbulence, i.e. in real space they are in the form of one-dimensional vortex filaments. This fact can be verified by analyzing isosurfaces of high real space vorticity which are associated with places where intensive dissipation of kinetic energy occurs. Isosurfaces of high vorticity in a vertical slice through the computational box are displayed in Fig. 4.11 (left). As expected, the dissipative structures have the form of quasi-one-dimensional filaments, which are irregularly distributed over the entire volume. All presented dissipative structures are chosen as representative

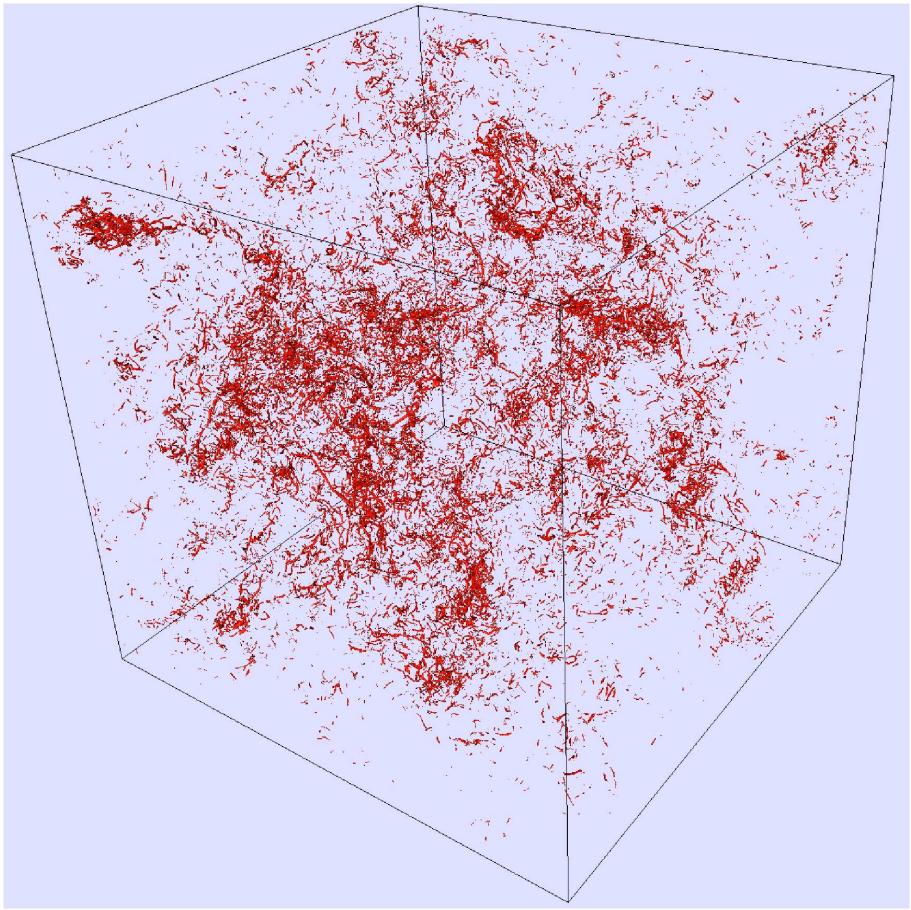

Figure 4.12: Global view of isosurfaces of high vorticity, which are associated with places where the most intensive dissipation of kinetic energy occurs, in the performed simulation of 3D thermal convection.

for the whole simulation run.

The relative scaling exponents of the temperature field structure functions indicate a more intermittent character of the temperature than that of the velocity field. Thus dissipative structures of entropy are expected to exhibit a different spatial pattern. Since thermal dissipation is associated with large temperature gradients, it occurs at the sharp transitions between individual regions of significantly different temperatures, and appears in the form of quasi-two-dimensional sheets. This fact can be seen in Fig. 4.11 (right) showing a zoom of several isosurfaces of the intensive entropy dissipation together with the underlying two-dimensional slice through the temperature field.

A global view of dissipative structures of the kinetic energy and the entropy is displayed in Fig. 4.12 and Fig. 4.13. These pictures demonstrate the qualitative difference between small-scale structures of the temperature and that of the velocity field.

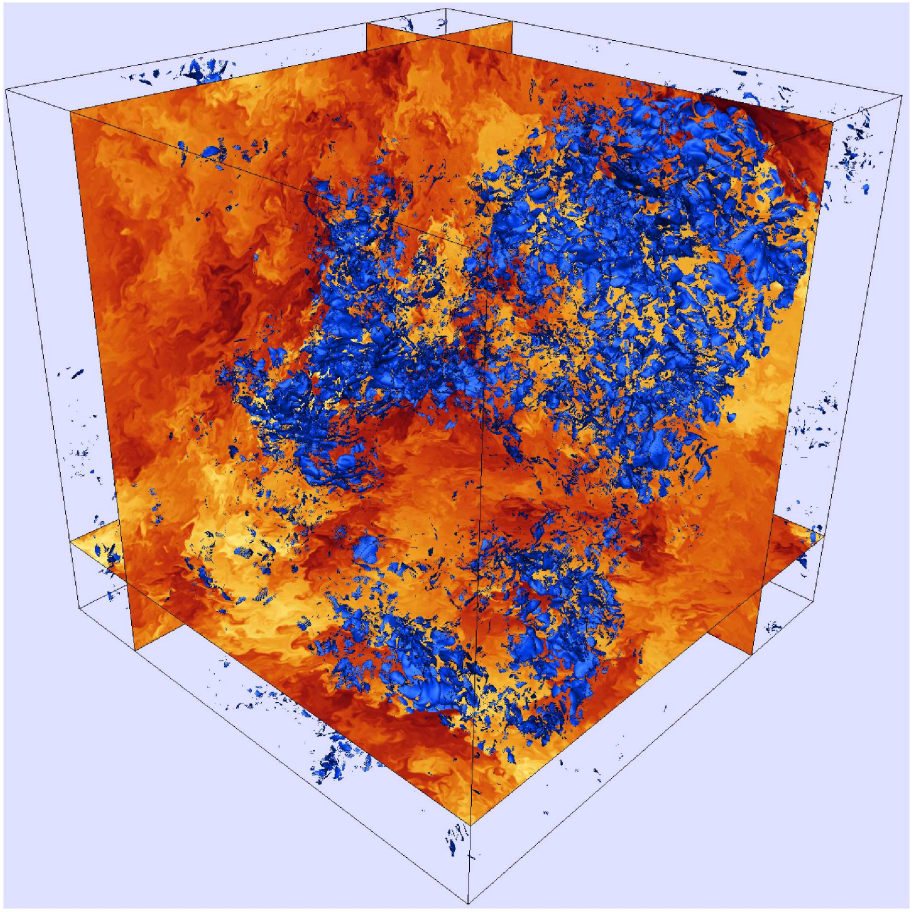

Figure 4.13: Global view of isosurfaces of high thermal dissipation in the performed simulation of 3D thermal convection (blue isosurfaces). Three two-dimensional slices show the structure of temperature fluctuations (light – high values, dark – low values).

Chapter 5

2D magnetohydrodynamic convection

Two-dimensional magnetohydrodynamic convection, also called magnetoconvection, is probably the simplest model, apart from shell models and other physical approximations, that provides an opportunity to study the impact of magnetic fields on the nonlinear dynamics of turbulent convection. Plasma dynamics in two dimensions can be seen as an approximation to fully three-dimensional systems with strong mean magnetic fields where the turbulent dynamics is largely restricted to two-dimensional planes perpendicular to the mean field in the third direction. The Lorentz force influences plasma motions, and at the same time the fluctuating velocity affects the evolution of magnetic fields. The system is considered as periodic in all directions, so it represents magnetohydrodynamic convection in a bulk of a turbulent flow. Surprisingly, no previous investigations of this setup have been found in the available literature. The focus is put on two-dimensional simulations without mean magnetic field because such a field would introduce additional anisotropy, and therefore complicate the analysis of buoyancy effects. Due to the absence of dynamo action in 2D magnetohydrodynamics (e.g. [Zel57][Cow55]) that would continuously supply energy to the magnetic field, it is necessary to drive magnetic field fluctuations separately, otherwise the magnetic energy would decay in time. However, if the magnetic Reynolds number is high enough and the magnetic field is almost "frozen" in the velocity field (e.g. [Mof78][Mes99]), this decay is a very slow process on the resistive time scale $\tau_{\mathrm{D}} = L^2/\eta$, so the magnetic energy can be considered as quasi-stationary on the time scale t that is longer than the typical buoyancy time and much shorter than the resistive time, $t_{\mathrm{b}} < t \ll \tau_{\mathrm{D}}$. A two-dimensional magnetoconvective system is a very useful numerical laboratory because reduced computational requirements allow to achieve high numerical resolutions and consequently relatively high Rayleigh numbers. Thus a numerically simulated 2D magnetoconvective system could operate in a buoyancy dominated Bolgiano-Obukhov-like regime (BO-like regime). At the same time, this system exhibits dynamic properties similar to three-dimensional systems, e.g. the total (kinetic and magnetic) energy is transported by a direct cascade to small scales as well as total energy in three-dimensional systems (e.g. [Mof78][Bis97]). Hence

physical processes involved also in 3D magnetoconvection might be detected. In addition, one of the open questions (see Introduction), namely: the importance of inverse cascade of energy for the formation of the BO regime of convection (e.g. [Bra92]), can be investigated by a comparison between two-dimensional magnetohydrodynamic and hydrodynamic systems.

5.1 Properties of 2D MHD

If the system of equations governing 3D magnetoconvection ((1.16)–(1.20)) is reduced in one horizontal dimension, the equations can be recast into the form

$$\frac{\partial \omega}{\partial t} + \mathbf{v}\cdot\nabla\omega - \mathbf{b}\cdot\nabla j = -\partial_x\theta + \tilde{\nu}\Delta\omega, \tag{5.1}$$

$$\frac{\partial \mathbf{b}}{\partial t} - (\mathbf{b}\cdot\nabla)\mathbf{v} + (\mathbf{v}\cdot\nabla)\mathbf{b} = \tilde{\eta}\Delta\mathbf{b}, \tag{5.2}$$

$$\frac{\partial \theta}{\partial t} + (\mathbf{v}\cdot\nabla)\theta = \tilde{\kappa}\Delta\theta + v_{z,x}, \tag{5.3}$$

$$\omega = \partial_z v_x - \partial_x v_z, \quad j = \partial_z b_x - \partial_x b_z, \tag{5.4}$$

$$\nabla\cdot\mathbf{v} = \nabla\cdot\mathbf{b} = 0 \tag{5.5}$$

where x and z are the horizontal direction and the vertical direction, respectively. Vorticity and current density are now scalar functions resembling the y-component of the originally three-dimensional vector fields. The magnetic field in 2D MHD is usually expressed in terms of one scalar function ψ that corresponds to the magnetic vector potential that is perpendicular to the xz-plane. Thus instead of the equation (5.2), the following equation for the evolution of this scalar function is used

$$\frac{\partial \psi}{\partial t} + (\mathbf{v}\cdot\nabla)\psi = \tilde{\eta}\Delta\psi. \tag{5.6}$$

The magnetic field and the current density are related to ψ, $\mathbf{b} = \nabla\psi \times \mathbf{e}_y$ and $j = -\Delta\psi$, respectively. The expression (5.6) is an advection-diffusion equation for an active scalar since ψ influences via the Lorentz force the time evolution of the velocity field. It follows from the structure of (5.6) and from the absence of any driving term that ψ decays in time, so the magnetic energy is eventually dissipated as well. Therefore, there is no dynamo action in 2D MHD ([Zel57], see also [Cow55]). However, it is possible to amplify the magnetic energy during the initial phase when ψ-field is distorted by the velocity field, and may form very steep gradients.

Analogously to 2D MHD, the ideal 2D magnetoconvective system, i.e. without dissipative effects, conserves the mean-square magnetic potential

$$A = \int_S \psi^2 dS. \tag{5.7}$$

The total (kinetic and magnetic) energy of the system is not constant in contrast to ideal 2D MHD, but it is driven by the vertical heat flux that provides energy for the excitation of velocity fluctuations

$$\frac{d}{dt}E^{\mathrm{tot}} = \frac{d}{dt}(E^{\mathrm{k}} + E^{\mathrm{m}}) = \frac{d}{dt}\int_S \frac{1}{2}(v^2 + b^2)dS = \int_S \theta v_z dS. \tag{5.8}$$

The cross-helicity H^{C}, which is an ideal invariant in 2D MHD, is of a special importance in 2D magnetoconvection as it turns out later. If dissipative effects are neglected, its time evolution is given as

$$\frac{d}{dt}H^{\mathrm{C}} = \frac{d}{dt}\int_S \mathbf{v}\cdot\mathbf{b}dS = \int_S \theta b_z dS. \tag{5.9}$$

Hence the cross-helicity is not conserved in ideal 2D magnetoconvection, and at the same time this is the first indication that the term θb_z might play an important role in the dynamics of turbulent convection under the influence of magnetic fields. All three quantities are subject to a nonlinear transport in spectral space. In 2D MHD turbulence the total energy and the cross-helicity are transferred from large to small scales by a direct cascade, whereas the mean-square magnetic potential is subject to an inverse cascade, and accumulates at the largest scales of a bounded system (e.g. [KM80][BS01][Bis03]).

5.2 Elsässer fields

It is useful from the theoretical point of view to rewrite the equations governing velocity and magnetic field in terms of the Elsässer variables (e.g. [Els50][Bis97] [LG03])

$$\mathbf{z}^{\pm} = \mathbf{v} \pm \mathbf{b}. \tag{5.10}$$

The Elsässer variables are well suited for analyses of nonlinear dynamics because the velocity and magnetic field equations in the Elsässer variables possess an almost symmetric form

$$\frac{\partial \mathbf{z}^{\pm}}{\partial t} + \mathbf{z}^{\mp}\cdot\nabla\mathbf{z}^{\pm} = -\nabla P + \frac{1}{2}\left(\tilde{\nu}+\tilde{\eta}\right)\Delta\mathbf{z}^{\pm} + \frac{1}{2}\left(\tilde{\nu}-\tilde{\eta}\right)\Delta\mathbf{z}^{\mp} + \theta\mathbf{e}_z, \tag{5.11}$$

$$\nabla\cdot\mathbf{z}^{\pm} = 0 \tag{5.12}$$

where $P = p + B^2/2$ is the total pressure. In configurations with a mean magnetic field, these equations without the buoyancy term $\theta\mathbf{e}_z$ can be solved, and lead to exact solutions in the form of counter-propagating Alfvén waves $\mathbf{z}^-$ and $\mathbf{z}^+$ traveling in the same and in the opposite direction along the mean field, respectively. The nonlinear dynamics in the Elsässer picture is therefore represented by an ensemble of interacting Alfvén wave packets. It follows from the structure of the nonlinear term that only counter-propagating wave packets interact. In systems without mean magnetic field, it is supposed that the wave packets propagate along a large-scale magnetic field that plays the role of a guide field. The other important quantities can be related to the $\mathbf{z}^{\pm}$ fields as

$$E^{\mathrm{tot}} = \frac{1}{4}\int_S (z^{+2} + z^{-2})dS, \tag{5.13}$$

$$H^{\mathrm{C}} = \frac{1}{4}\int_S (z^{+2} - z^{-2})dS. \tag{5.14}$$

Thus it is possible to work solely within the Elsässer framework (e.g. [Bis03]). Both Elsässer energies

$$E^+ = \frac{1}{2}\int_S {z^+}^2 dS, \tag{5.15}$$

$$E^- = \frac{1}{2}\int_S {z^-}^2 dS \tag{5.16}$$

are subject to a spectral transfer. They cascade from large to small scales where they are eventually dissipated by viscous processes.

5.3 Iroshnikov-Kraichnan phenomenology

The Iroshnikov-Kraichnan (IK) phenomenology of magnetohydrodynamic turbulence (e.g. [Iro64][Kra65][Bis97]) can be easily explained in the framework of the Elsässer description. The essential assumptions of this phenomenology are: a) constancy and isotropy of spectral fluxes $\epsilon^\pm$ of the Elsässer energies which are assumed to be comparable, $E^+ \approx E^-$, b) interactions between Alfvén wave packets (eddies) are of random nature. Moreover, a large number of these interactions is necessary to distort an eddy and transfer the energy from one scale to another.

Two counter-propagating Alfvén wave packets interact during the Alfvén crossing time $\tau_\mathrm{A} \approx l/v_\mathrm{A}$ (for the definition of v_A see subsection 1.2.2). However, since $\tau_\mathrm{A} \ll \tau_\pm$, where $\tau_\pm \approx l/z^\mp$ is the dynamical time of an eddy of size l, the amplitudes of the Alfvén wave packets during one interaction change only slightly. Therefore, $N = (\tau_\pm/\tau_\mathrm{A})^2$ of elementary interactions (random walk analogy) are required to produce a significant distortion of an eddy. The nonlinear time of the spectral transfer of $E^\pm$ between wave packets can be thus expressed as

$$\tau^\pm_\mathrm{IK} = N\tau_\mathrm{A} = \left(\frac{\tau_\pm}{\tau_\mathrm{A}}\right)^2 \tau_\mathrm{A} = \left(\frac{\tau_\pm}{\tau_\mathrm{A}}\right)\tau_\pm. \tag{5.17}$$

The spectral energy fluxes are given as

$$\epsilon^\pm \sim \frac{E^\pm}{\tau^\pm_\mathrm{IK}} \sim \frac{E^+E^-\tau_\mathrm{A}}{l^2} \approx \frac{E^+E^-}{v_\mathrm{A}l}. \tag{5.18}$$

The energy fluxes $\epsilon^\pm$ are equal since the expression for them is symmetric in E^+ and E^- and moreover $E^+ \approx E^-$ (see above). Both energies are transferred with the constant transfer rates $\epsilon^\pm$ from large to small scales where they are eventually dissipated with the rates $\varepsilon^\pm$, i.e. $\epsilon^\pm = \varepsilon^\pm = \varepsilon$. Since it is assumed that $E^+ \approx E^-$, the scaling predictions for $E^\pm$ in the inertial range can be obtained from (5.18). They read

$$E^\pm(l) \sim (\varepsilon v_\mathrm{A})^{1/2} l^{1/2}. \tag{5.19}$$

In contrast to (5.13)–(5.16), here the energy is considered as a scale-dependent quantity that is related to turbulent fluctuations at scale l. Because the total energy E^tot is the sum of E^+ and E^-, it scales in the inertial range analogously

$$E^\mathrm{tot}(l) = C_\mathrm{IK}(\varepsilon_\mathrm{tot} v_\mathrm{A})^{1/2} l^{1/2}. \tag{5.20}$$

Here $\varepsilon_{\rm tot} = \tilde{\nu}\int_S \omega^2 dS + \tilde{\eta}\int_S j^2 dS$ is the total energy dissipation rate. The constant $C_{\rm IK}$ was determined numerically, $C_{\rm IK} \approx 1.8$ (e.g. [Bis03][BS01]). The derivation of the scaling relation (5.20) in the IK phenomenology does not formally depend on the dimension of the system, so it should be valid also in the 3D case. On the contrary, results of high-resolution numerical simulations of isotropic 3D MHD turbulence (e.g. [BM00][MB00]) suggest different scaling behavior, namely $E^{\rm tot} \sim l^{2/3}$. However, in two dimensions the validity of the IK phenomenology is confirmed by a number of numerical simulations (e.g. [BW89][BS01]). A plausible explanation for the difference between scaling exponents of total energy spectra in 2D and 3D MHD turbulence is provided by several authors (e.g. [Bol06][Gog06]).

The magnetic potential A exhibits an inertial-range scaling as well. The scaling relation for A is derived assuming that the mean-square potential flux is constant. In case of a large-scale energy input, the magnetic potential in the inertial range scales as (see [Pou78][Bis03])

$$A(l) \sim E(l) l^2 \sim l^{5/2}. \tag{5.21}$$

This relation has been verified in numerical simulations of closure equations ([Pou78]).

In the following, numerical results from a simulation of 2D magnetoconvection are reported. The simulation is performed with the resolution 2048^2, and the system is evolved for 15 typical buoyancy times. The dissipation coefficients are set to $\tilde{\nu} = \tilde{\eta} = 7 \cdot 10^{-4}$ and $\tilde{\kappa} = 1.3 \cdot 10^{-4}$ which corresponds to $\mathsf{Pr_m} = 1$ and $\mathsf{Pr} \approx 5.4$. The nominal Rayleigh number of this run is $\mathsf{Ra} \approx 2 \cdot 10^6$, and the Reynolds numbers (see sections 1.2.2 and 3.1) achieved in the simulation are $\mathsf{Re} = \mathsf{Re_m} \approx 5 \cdot 10^4$. All spectral results presented in the following sections are obtained from this simulation.

Furthermore, since the investigated system exhibits a behavior with many unexpected features, one additional simulation with lower resolution is performed to verify the long-time character of the system. This simulation is performed with the resolution 1024^2. The dissipation coefficients are set to $\tilde{\nu} = 1.5 \cdot 10^{-3}$, $\tilde{\eta} = 7.5 \cdot 10^{-4}$, $\tilde{\kappa} = 4 \cdot 10^{-4}$. They correspond to $\mathsf{Pr_m} = 2$ and $\mathsf{Pr} = 3.75$. The nominal Rayleigh number is $\mathsf{Ra} \approx 9 \cdot 10^5$, and both Reynolds numbers are $\mathsf{Re} \approx \mathsf{Re_m} \approx 10^4$. This system is evolved for approximately 100 typical buoyancy times.

5.4 Quasi-oscillations between turbulent regimes

The most striking feature of the simulated 2D magnetoconvective system is the fact that the system does not operate only in one regime of turbulence, e.g. Iroshnikov-Kraichnan, Kolmogorov, Goldreich-Sridhar, Bolgiano-Obukhov, but it permanently changes its state between two turbulent regimes with different properties. This phenomenon can be described as quasi-oscillations between the Iroshnikov-Kraichnan (IK) regime where effects of buoyancy are negligible at inertial-range scales and the buoyancy dominated Bolgiano-Obukhov-like (BO-like) regime where buoyancy forces dominate the inertial-range dynamics. The

system evolves in a quasi-stationary manner with time intervals of IK turbulence and time intervals of a buoyancy dominated BO-like turbulence.

This configuration sets in after the initial exponentially growing convective instability saturates nonlinearly, and the system attains a quasi-stationary well-developed turbulent state. At this stage the magnetic potential exhibits steep gradients, and the levels of the magnetic and the kinetic energy are comparable. During the following nonlinear evolution, the magnetic potential decays only negligibly. The system remains in a quasi-stationary state, and performs quasi-oscillations between two turbulent regimes. Kinetic and magnetic energy as well as entropy remain at an approximately constant level.

5.4.1 Integral characteristics

In this section, the time evolution of total values of several important physical quantities is presented. This gives an overview of large-scale changes of the system, and provides an insight into the global character of the flow. These quantities are plotted in Fig. 5.1. The left column shows the results obtained from the simulation with the resolution 2048^2 whereas the right column demonstrates the long-time evolution obtained from the run with the resolution 1024^2.

The uppermost figures show the total values of the kinetic energy (see (3.4)), of the magnetic energy and of the entropy (defined analogously). The magnetic energy is in both simulations about 20% larger than the kinetic energy. The level of magnetic energy is governed by the magnetic Reynolds number which determines the "frozen in" property and thereby the amplification of the magnetic field by the turbulent dynamo (e.g. [MP89]). In both simulations the value of $\mathsf{Re_m}$ is similar (see above). The entropy, i.e. the energy of the temperature fluctuations, remains at a low level ($\approx 30\%$ of the kinetic energy). The energies in the simulation with the higher resolution increase slightly, but this behavior occurs at a time scale t that is larger than the typical buoyancy time t_b, $t \gg t_\mathrm{b}$. Thus it has a negligible effect on the instantaneous dynamics of turbulent fluctuations at inertial-range scales. In order to verify this fact, the simulation with the resolution 1024^2 is performed, and its results analyzed. A decrease of the magnetic energy ($\approx 30\%$ over 100 buoyancy times) is observed there, while the global (and spectral) properties of the system remain the same. This decrease is related to the diffusion of the mean-square magnetic potential, shown in the graphs in the second row, which becomes important at longer time scales t, $t \approx \tau_\mathrm{D} \gg \tau_\mathrm{b}$. Therefore, the magnetic potential in the high-resolution simulation which is followed for approximately 15 typical buoyancy times remains almost constant.

The plots in the third row display the time evolution of the total value of the turbulent heat flux $v_z\theta$. The total turbulent heat flux is positive, so it drives the velocity field and consequently magnetic field fluctuations. In both simulations it fluctuates on the time scale of the typical buoyancy time. This fact becomes important later when it is compared with the time scale of fluctuations of the cross-helicity.

The lowermost figures show the evolution of the total values of the cross-helicity H^C and of the correlation coefficient defined as the normalized value of the

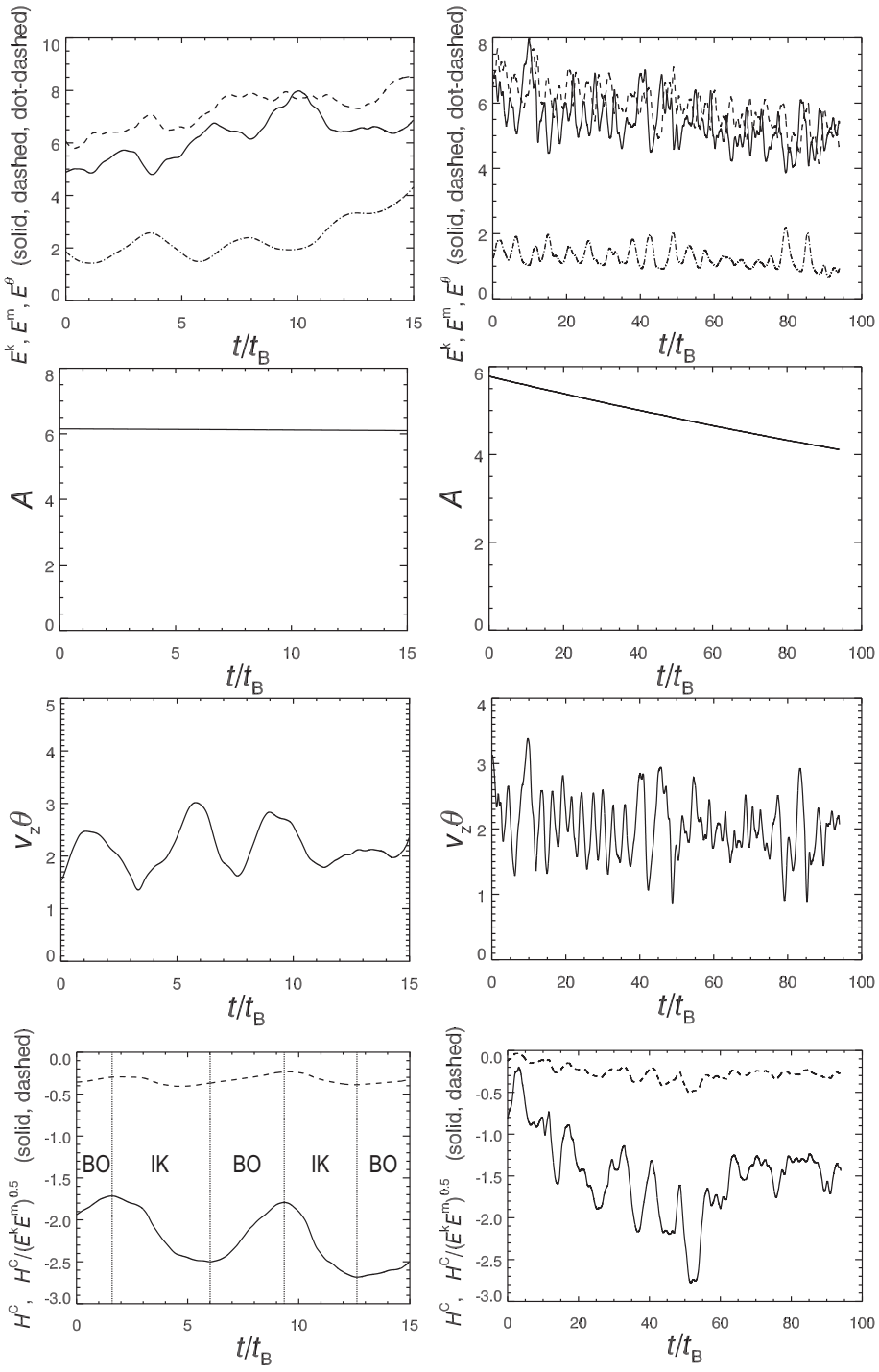

Figure 5.1: The time evolution of the total values of the kinetic energy, the magnetic energy and the entropy (top), of the mean-square magnetic potential (second row), of the vertical heat flux (third row) and of the cross-helicity and the correlation coefficient (bottom) in the performed simulations of 2D magnetoconvection. The left column displays the quantities obtained from the run with the resolution 2048^2. The right column shows the long-time evolution of the quantities obtained from the run with the resolution 1024^2. Vertical dotted lines in the l.h.s. plot of the cross-helicity indicate time intervals of the BO regime and the IK regime. Similar quasi-oscillations are present also in the low resolution simulation although not explicitly indicated.

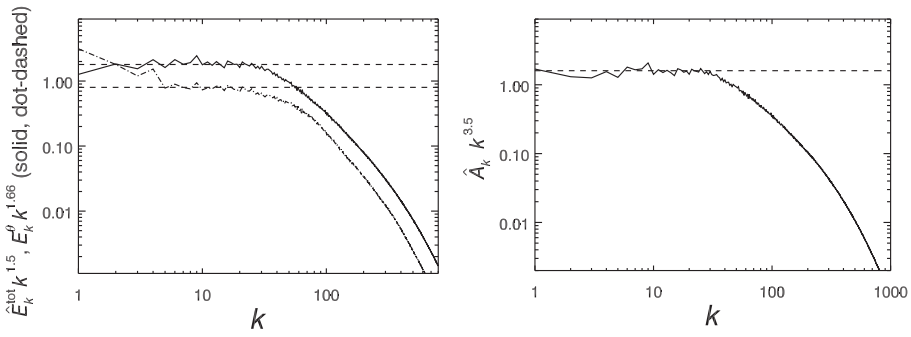

Figure 5.2: Left: The total energy spectrum $\hat{E}_k^{\rm tot}$ and the entropy spectrum E_k^θ obtained by time-averaging over the IK phases. The total energy spectrum is normalized by $(\varepsilon_{\rm tot} v_{\rm A})^{1/2}$ and compensated by $k^{1.5}$ (cf. (5.20)). The entropy spectrum is compensated by the Kolmogorov factor $k^{1.66}$. Horizontal lines indicate the scaling $k^{-1.5}$ and $k^{-1.66}$. Right: The mean-square magnetic potential spectrum obtained by time-averaging over the IK phases. The spectrum is normalized by the same factor as the total energy and compensated by $k^{3.5}$ (cf. (5.21)).

cross-helicity $H^{\rm C}/(E^{\rm k}E^{\rm m})^{1/2}$. The cross-helicity is in both cases always negative. The correlation coefficient varies around 30%. The cross-helicity seems to be of special importance in 2D magnetoconvective systems since it is found that the changes of the spectral properties (shown later) between the IK phase and the BO-like phase are time-correlated with the changes of the cross-helicity. The IK regime occurs when the absolute value of the cross-helicity increases, whereas the BO-like regime appears in time intervals when the absolute value of the cross-helicity decreases. Time intervals of the turbulent regimes are indicated by vertical dotted lines in the plot of the cross-helicity obtained from the high resolution simulation (see Fig. 5.1). Similar quasi-oscillations are present also in the low resolution simulation although corresponding time intervals are not explicitly indicated in the plot. It is important to mention that in the performed simulations the changes of the cross-helicity are slower than fluctuations of other physical quantities, e.g. of the turbulent heat flux or of the energies (see Fig. 5.1). These vary much quicker, so the quasi-oscillations are rather insensitive to them.

As a result of two different turbulent regimes, various spectral quantities averaged over the whole simulation time do not exhibit any scaling, whereas the averaging over these two phases separately leads to a surprisingly clear spectral scaling. Particular features of these two different regimes are discussed in the next two subsections.

5.4.2 Iroshnikov-Kraichnan phase

The Iroshnikov-Kraichnan (IK) phase occurs approximately when the absolute value of the cross-helicity increases as shown in the plot of the cross-helicity in Fig. 5.1. The total energy spectrum and the entropy spectrum obtained by time-averaging over the IK phases are depicted on the l.h.s. of Fig. 5.2. The

total energy spectrum $\hat{E}_k^{\rm tot}$ is compensated by $k^{3/2}$ (cf. (5.20)) which makes an inertial range that scales according to the IK prediction $k^{-3/2}$ horizontal. Moreover, the spectrum is normalized by the factor $(\varepsilon_{\rm tot} v_{\rm A})^{1/2}$ (cf. (5.20)). The total energy spectrum exhibits an inertial range extended over about one decade in wavenumber $3 \lesssim k \lesssim 30$. The nondimensional coefficient $C_{\rm IK}$ from the IK scaling relation (5.20) is determined as $C_{\rm IK} \approx 1.8$. This value agrees well with previously obtained values in 2D MHD turbulence ([BS01]).

The time-averaged entropy spectrum E_k^θ is compensated by the factor $k^{5/3}$ (cf. (1.32)). The spectrum scales in the inertial range with an exponent around -1.66. This exponent corresponds to the Obukhov-Corrsin-like scaling $k^{-5/3}$ (cf. (1.32)). Since the exponent -5/3 is predicted for a passive scalar turbulence, it is suggested that the temperature in the IK phase is passively advected by a IK turbulent flow, so it does not significantly influence the nonlinear dynamics of the system.

The r.h.s. of Fig. 5.2 displays the time-averaged spectrum of the mean-square magnetic potential. The spectrum is normalized by the same factor as the total energy, $(\varepsilon_{\rm tot} v_{\rm A})^{1/2}$, and compensated by $k^{3.5}$ (cf. (5.21)). The horizontal dashed line indicates the scaling $k^{-3.5}$. The scaling exponent is found close to the value -3.5. This is in agreement with the scaling prediction $k^{-7/2}$ (cf. (5.21)) derived in the framework of MHD turbulence for configurations with a large-scale energy input. This is also the case of turbulent convection since the vertical heat flux drives convective motions predominantly at the largest scales.

The fact that when the absolute value of the cross-helicity increases the system exhibits IK turbulence is confirmed by the analysis of spectral transfer functions computed from the various nonlinear terms in (5.1)–(5.5) that dominate the turbulence dynamics. Transfer functions are introduced and defined in section 3.3.

The total energy transfer function $\hat{T}_k^{\rm tot}$ and the entropy transfer function $\hat{T}_k^\theta$ are depicted in Fig. 5.3. Both transfer functions are normalized by the corresponding dissipation rates, $\varepsilon_{\rm tot}$ and ε_θ. The constant value of the transfer function $\hat{T}_k^{\rm tot}$ indicates the inertial region, where neither energy input nor energy dissipation is important, so the spectral energy flux is constant. The inertial range identified in this way occurs in the approximately same spectral region as that of the total energy spectrum (Fig. 5.2) though slightly shorter $4 \lesssim k \lesssim 20$. The level of the normalized energy flux is considerably smaller than unity. However, this feature is difficult to interpret since it depends on the particular selection of time intervals of the IK regime used for time-averaging (see later remarks in subsection 5.4.4), and therefore the level of the spectral energy flux might be influenced by the turbulent heat flux. The total energy transfer function $\hat{T}_k^{\rm tot}$ is everywhere positive which means that the energy is transported by a direct cascade from large to small scales. Also this fact is in agreement with the IK phenomenology. The entropy is transferred by a direct cascade because its transfer function $\hat{T}_k^\theta$ is everywhere positive as well. However, in contrast to $\hat{T}_k^{\rm tot}$ the entropy transfer function $\hat{T}_k^\theta$ does not exhibit any visible scaling at intermediate scales. The curve is at the transition from large to intermediate scales ($k \approx 5$) strongly irregular which is probably an effect of the large-scale driving by the mean temperature gradient.

It is possible to analyze the spectral energy flux in more detail by considering

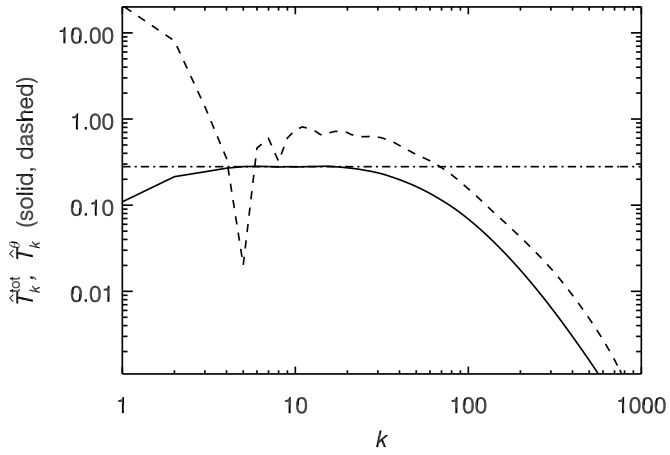

Figure 5.3: The total energy transfer function $\hat{T}_k^{\rm tot}$ and the entropy transfer function $\hat{T}_k^{\theta}$ obtained from the IK phases of 2D magnetoconvective turbulence. Both transfer functions are normalized by the corresponding dissipation rates, $\varepsilon_{\rm tot}$ and ε_{θ}. Both transfer functions are positive indicating a direct cascade of the total energy and the entropy.

the action of different nonlinear terms separately. The result of this analysis is depicted in Fig. 5.4. The picture on the l.h.s. shows the spectrum of the kinetic energy transfer function $\hat{T}_k^{\rm EV}$ and the spectrum of the absolute value of the magnetic energy transfer function $|\hat{T}_k^{\rm EM}|$. For $5 \lesssim k \lesssim 10$ the spectrum of $\hat{T}_k^{\rm EM}$ is negative. This part is denoted by the dotted line in the plot. The transfer functions are normalized by the total dissipation rate $\varepsilon_{\rm tot}$ (see section 5.3). Comparing both spectra it is evident that the major contribution to the total energy flux is caused by the nonlinear terms in the vorticity equation (5.1). Furthermore, the spectrum of $\hat{T}_k^{\rm EV}$ exhibits a constant region at intermediate scales. However, this feature does not imply that the kinetic energy is conserved during the cascade transfer because the Lorentz force exchanges the energy between the magnetic and the velocity field, i.e. it extracts and supplies the energy from/to the kinetic energy cascade. The spectrum of the magnetic energy transfer function $|\hat{T}_k^{\rm EM}|$ assumes at all scales values that are several orders of magnitude smaller than that of $\hat{T}_k^{\rm EV}$, and therefore the impact on the total energy transfer caused by the nonlinear terms in the magnetic field equation (5.2) is negligible.

The picture on the r.h.s. of Fig. 5.4 displays two parts of the kinetic energy transfer function, namely $|\hat{T}_k^{\rm adv}|$ computed from the advective term $\mathbf{v} \cdot \nabla\omega$ and $\hat{T}_k^{\rm Lor}$ computed from the Lorentz term $-\mathbf{b}\cdot\nabla j$. The plot shows the absolute value of $\hat{T}_k^{\rm adv}$ because the spectrum of $\hat{T}_k^{\rm adv}$ contains a negative part at $1 \lesssim k \lesssim 90$ denoted by the dotted line which corresponds to an inverse cascade of the kinetic energy. The same normalization as in the previous cases is used. It is evident that the Lorentz force dominates the spectral transfer of the kinetic energy.

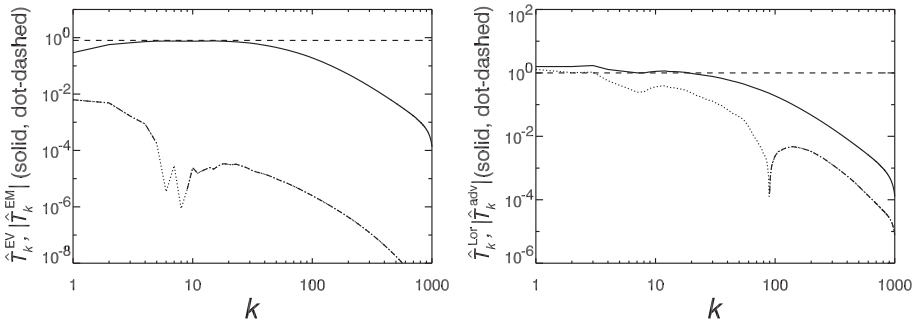

Figure 5.4: Left: The kinetic $\hat{T}_k^{\mathrm{EV}}$ and the absolute value of the magnetic $|\hat{T}_k^{\mathrm{EM}}|$ part of the total energy transfer function obtained from the IK phases. The negative part of $\hat{T}_k^{\mathrm{EM}}$ ($5 \lesssim k \lesssim 10$) is denoted by the dotted line. Right: The absolute value of the advective part $|\hat{T}_k^{\mathrm{adv}}|$ and the Lorentz part $\hat{T}_k^{\mathrm{Lor}}$ of the kinetic energy spectral transfer. In the interval $1 \lesssim k \lesssim 90$ the function $\hat{T}_k^{\mathrm{adv}}$ assumes negative values. All four transfer functions are normalized by the total energy dissipation rate $\varepsilon_{\mathrm{tot}}$.

Moreover, its contribution to the flux is approximately constant in the inertial region. The transfer function $\hat{T}_k^{\mathrm{adv}}$ computed from the velocity advection is at the intermediate and large scales negative, i.e. an inverse cascade of the kinetic energy, which is typical for 2D hydrodynamic turbulence. However, the total transport of the kinetic energy is still direct since the Lorentz force affects the kinetic energy transfer as well.

5.4.3 Buoyancy dominated phase

The buoyancy dominated BO-like phase occurs approximately when the absolute value of the cross-helicity decreases as shown in the plot of the cross-helicity in Fig. 5.1. The total energy spectrum E_k^{tot} and the entropy spectrum E_k^{θ} obtained by time-averaging over the BO-like phases are depicted on the l.h.s. of Fig. 5.5. There exist no scaling predictions for the energy spectra in this regime of MHD turbulence, so both spectra are left without normalization. However, they are compensated by the factor k^2 since it is found that the spectra at intermediate scales follow approximately a slope with an exponent around -2. Despite the fact that the total energy spectrum does not exhibit a clear scaling, it deviates significantly from the behavior predicted in the frame of the IK phenomenology, $k^{-3/2}$ (cf. (5.20)). The compensated spectrum of temperature fluctuations displays a short horizontal plateau around the wavenumber $k = 10$. This part of the spectrum coincides with the horizontal dashed line that indicates a slope k^{-2}. Although the determination of an exact value of the exponent is difficult, the entropy spectrum in the inertial range scales also close to k^{-2}. The scaling exponent of the entropy spectrum differs also considerably from the IK value -1.66 detected in the IK phases (cf. Fig. 5.2). These facts indicate that the system operates in a different dynamical regime.

The r.h.s. picture shows the kinetic energy spectrum and the magnetic energy spectrum plotted individually. Although kinetic and magnetic energy separately

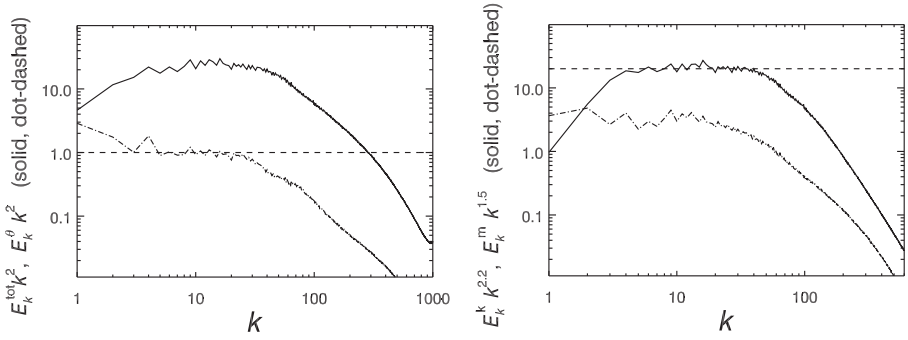

Figure 5.5: Left: The total energy spectrum $E_k^{\rm tot}$ and the entropy spectrum E_k^θ obtained by time-averaging over the BO-like phases. Both spectra are compensated by the factor k^2. Right: The spectrum of the kinetic and the magnetic energy, $E_k^{\rm k}$ and $E_k^{\rm m}$. The kinetic energy spectrum is compensated by the BO factor $k^{2.2}$. The horizontal dashed line indicates the slope $k^{-2.2}$. The magnetic energy spectrum is compensated by the factor $k^{1.5}$.

are not ideally conserved quantities, and therefore no scaling in their spectra is a priori expected, it can be still interesting to analyze them. Both spectra are computed by time-averaging over the BO-like phases. The kinetic energy spectrum is compensated by the BO factor $k^{2.2}$ in order to make the inertial range that scales with the exponent -2.2 horizontal. The inertial interval of the spectrum coincides with the horizontal dashed line that indicates the slope $k^{-2.2}$. The kinetic energy spectrum exhibits a very good scaling in the range of wave numbers $4 \lesssim k \lesssim 40$. The observed scaling exponent almost ideally fits the value -2.2 predicted by the Bolgiano-Obukhov phenomenology for hydrodynamic turbulent convection (see subsection 1.3.2). On the contrary, the magnetic energy spectrum compensated by the IK scaling factor $k^{1.5}$ does not show any visible inertial range. This is not surprising since the magnetic energy separately is not conserved during the inertial-range transport. However, the shape of the spectrum suggests that it does not differ considerably from the IK case.

The spectra shown in Fig. 5.5 indicate that the system in the BO-like phase is strongly influenced by the convective heat flux, and that buoyancy forces play a dominant role in the nonlinear dynamics. The energy spectra in the BO-like phases differ significantly from the energy spectra in the IK phases (cf. Fig. 5.2, Fig. 5.5).

In order to obtain more detailed information about nonlinear processes in the BO-like phase, several transfer functions are plotted in Fig. 5.6. The l.h.s. graph displays the total energy transfer function $\hat{T}_k^{\rm tot}$ and the absolute value of the entropy transfer function $|\hat{T}_k^\theta|$. Both are normalized by the corresponding dissipation rates, $\varepsilon_{\rm tot}$ and ε_θ. The spectrum of $\hat{T}_k^{\rm tot}$ is compensated by the factor $k^{0.21}$ to emphasize the difference of the scaling compared to the IK case ($\hat{T}_k^{\rm tot} \sim k^0 \sim$ const.). Indeed, the total energy transfer function is not constant in the inertial range, but it scales approximately with the exponent -0.21. This value deviates significantly from both the IK prediction $k^0 \sim$ const. and from the Bolgiano-Obukhov prediction $k^{-4/5}$ as well (cf. 3.14). So far there is no

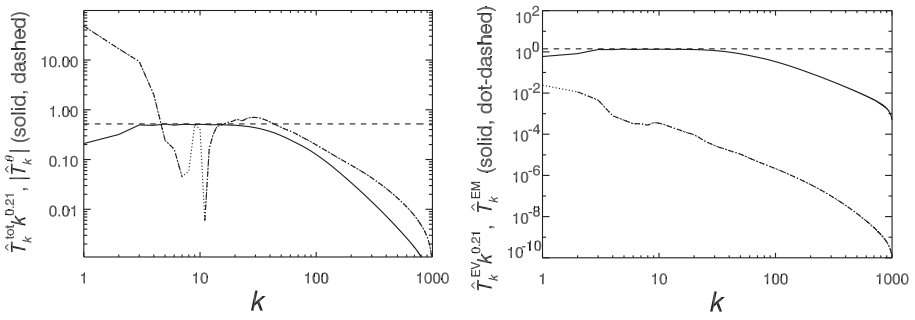

Figure 5.6: Left: The total energy transfer function $\hat{T}_k^{\mathrm{tot}}$ and the absolute value of the entropy transfer function $|\hat{T}_k^{\theta}|$ in the BO-like regime. For $7 \lesssim k \lesssim 11$ the spectrum of $\hat{T}_k^{\theta}$ assumes negative values. Both functions are normalized by the corresponding dissipation rates, $\varepsilon_{\mathrm{tot}}$ and ε_{θ}. The transfer function $\hat{T}_k^{\mathrm{tot}}$ is compensated by $k^{0.21}$. Right: The kinetic $\hat{T}_k^{\mathrm{EV}}$ and the magnetic $\hat{T}_k^{\mathrm{EM}}$ contribution to the total spectral flux. Both functions are normalized by the dissipation rate $\varepsilon_{\mathrm{tot}}$. Moreover, $\hat{T}_k^{\mathrm{EV}}$ is compensated by $k^{0.21}$.

available theory that explains the inertial-range scaling of T_k^{tot} with such an exponent. This issue is discussed further in the following subsection. The spectrum of the entropy transfer function $\hat{T}_k^{\theta}$ assumes in the interval $7 \lesssim k \lesssim 11$ negative values. However, it is difficult to interpret this feature since it depends on time-averaging, and is therefore largely influenced by the particular selection of time intervals of the BO regime (see later remarks in subsection 5.4.4).

The r.h.s. graph in Fig. 5.6 displays individual contributions to the spectral flux of the total energy. While the normalized magnetic energy transfer function $\hat{T}_k^{\mathrm{EM}}$ assumes at all scales smaller values than the normalized kinetic energy transfer function $\hat{T}_k^{\mathrm{EV}}$, and does not show any clear inertial range, the function $\hat{T}_k^{\mathrm{EV}}$ exhibits a region that scales as $k^{-0.21}$. Thus the scaling of the spectral flux of the total energy is caused by the nonlinear interactions in the vorticity equation (5.1). It should be kept in mind that the amount of energy is not conserved in the individual transfers.

5.4.4 Dynamical model of quasi-oscillations

According to the results presented in the last two subsections, the simulated 2D magnetoconvective system changes its turbulent regime in time in an oscillatory way. The aim of this subsection is to explore the dynamics more deeply and try to develop a dynamical model that is able to explain the observed quasi-oscillations.

It is found and supported by the presented spectra that the changes of the turbulent states are time-correlated with changes of the cross-helicity (see Fig. 5.1), i.e. with the total time derivative of the cross-helicity. Thus it is necessary at first to understand the cross-helicity dynamics and the source of these relatively slow (compared to total values of other quantities, see Fig. 5.1) cross-helicity fluctuations. The full equation governing the time evolution of cross-helicity in

2D magnetoconvection can be derived from the equation for velocity fluctuations

$$\frac{\partial \mathbf{v}}{\partial t} + (\mathbf{v}\cdot\nabla)\mathbf{v} - (\mathbf{b}\cdot\nabla)\mathbf{b} + \nabla P = \theta \mathbf{e}_z + \tilde{\nu}\Delta\mathbf{v}, \tag{5.22}$$

where $P = p + B^2/2$ is the total pressure, and the equation for magnetic field fluctuations (5.2). The equation for the time evolution of the cross-helicity reads (cf. (5.9))

$$\frac{\partial H^{\mathrm{C}}}{\partial t} + \int_S [-\mathbf{v}\cdot(\mathbf{b}\cdot\nabla)\mathbf{v} + \mathbf{v}\cdot(\mathbf{v}\cdot\nabla)\mathbf{b} + \mathbf{b}\cdot(\mathbf{v}\cdot\nabla)\mathbf{v} -$$
$$-\mathbf{b}\cdot(\mathbf{b}\cdot\nabla)\mathbf{b} + \mathbf{b}\cdot\nabla P]dS = \int_S \theta b_z dS - (\tilde{\nu}+\tilde{\eta})\int_S j\omega dS. \tag{5.23}$$

The nonlinear terms appearing in the first integral are the nonlinear terms from the equation for magnetic field (5.2) multiplied by $\mathbf{v}$ and the nonlinear terms from the equation for velocity (5.22) multiplied by $\mathbf{b}$. The two terms on the r.h.s. of (5.23) represent sources and sinks. In general, each of these terms can be positive or negative which means that it can sometimes inject and sometimes reduce the cross-helicity in the system. However, there is a difference between these two terms. The second term contains partial derivatives, so it has a larger effect at small scales, whereas the first term has a similar structure as the hydrodynamic turbulent heat flux $v_z\theta$, so it injects the cross-helicity predominantly at large scales (cf. section 1.3.2). The nonlinear terms in the first integral in (5.23) can be expressed in divergence form, and therefore conserve the total amount of the cross-helicity in a volume with periodic boundaries. These terms cause nonlinear interactions that redistribute the cross-helicity over different spatial scales. The cross-helicity undergoes a direct cascade and is nonlinearly transported from large to small scales where it is eventually dissipated (e.g. [Bis03]).

The time evolution of the quantities on the r.h.s. of (5.23) in the high resolution simulation is plotted in Fig. 5.7. The dashed line denotes the term $\int_S \theta b_z dS$. The dot-dashed line shows the contribution of the term $-(\tilde{\nu}+\tilde{\eta})\int_S j\omega dS$. The sum of both terms, i.e. the total time derivative of the cross-helicity, is represented by the solid line. The cross-helicity in the performed simulation is always negative. Thus when the absolute value of the cross-helicity increases, the total time derivative of the cross-helicity is negative. On the contrary, when the absolute value of the cross-helicity decreases, the total time derivative is positive. Therefore, the phases of the IK turbulence can be identified with negative parts of the solid line, whereas the phases of the BO-like turbulence can be identified with its positive parts. Time intervals associated with both turbulent regimes are indicated by vertical dotted lines in the plot. The term $\int_S \theta b_z dS$ is always negative, so it permanently injects negative cross-helicity into the system. Fig. 5.7 demonstrates that if the small scale dissipation $-(\tilde{\nu}+\tilde{\eta})\int_S j\omega dS$ becomes larger than the amount of the cross-helicity injected by the term $\int_S \theta b_z dS$, the system switches from the IK phase to the BO-like phase and vice versa.

Nonlinear interactions govern the dynamics at inertial-range scales. At these scales the nonlinear terms in (5.23) represent the difference between the spectral fluxes ϵ^+ and ϵ^- of the Elsässer energies E^+ and E^-. The effect of the dissipation and the source term are negligible at inertial-range scales. The spectral

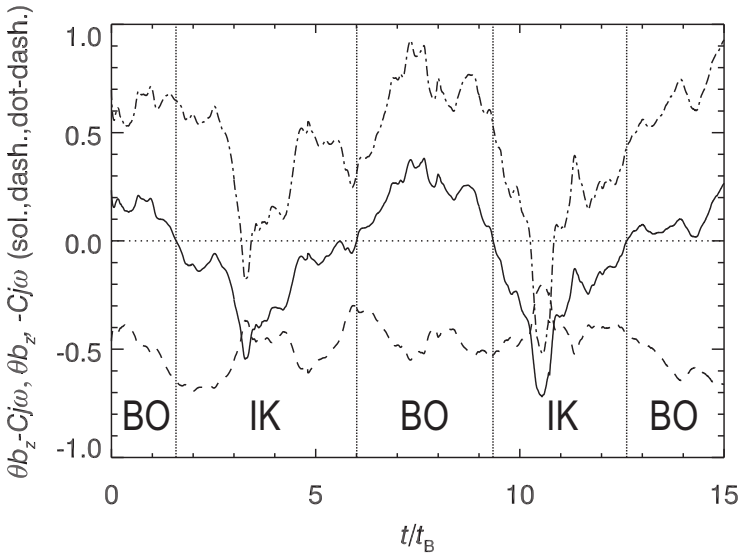

Figure 5.7: The time evolution of the total time derivative of the cross-helicity (the solid line) and its two contributions separately: $\int_S \theta b_z dS$ (the dashed line) and $-(\tilde{\nu}+\tilde{\eta})\int_S j\omega dS$ (the dot-dashed line) obtained from the high resolution simulation of 2D magnetoconvection. Time intervals of the BO regime and the IK regime are indicated by vertical dotted lines.

flux of cross-helicity $\epsilon^{\mathrm{C}} \sim vbv/l$ in a stationary state can be therefore expressed in the form

$$\epsilon^{\mathrm{C}} \approx \epsilon^{+} - \epsilon^{-} \tag{5.24}$$

as can be seen from (5.14) which relates the cross-helicity to the Elsässer fields. The spectral energy fluxes ϵ^{+} and ϵ^{-} are approximately equal in the IK regime. This is one of the implicit assumptions of the IK phenomenology (see section 5.3). The nonlinear transfer of the cross-helicity is therefore strongly reduced. On the contrary, if the Elsässer fluxes differ, the cross-helicity transport works efficiently.

Furthermore, it is important to remember that cross-helicity can be interpreted as the difference of Elsässer energies (cf. (5.14)). From this point of view the Iroshnikov-Kraichnan phenomenology describes balanced MHD turbulence (for definition see e.g. [LGS07]) since it assumes a scale-by-scale equality of Elsässer energies and their spectral fluxes. It is known that an increasing level of cross-helicity, i.e. an increasing difference between Elsässer energies E^{+} and E^{-}, reduces the efficiency of nonlinear MHD interactions. This process leads asymptotically to an Alfvénic state of MHD turbulence with perfectly aligned fields $\mathbf{v} = \pm\mathbf{b}$ where nonlinear MHD interactions are completely switched off (e.g. [Bis03][GFP82]). This is an extreme case of imbalanced MHD turbulence (for definition see e.g. [LG03][LGS07][GLP83]). Imbalanced MHD interactions are considered as scattering of large amplitude Alfvén packets of one Elsässer field with counter-propagating small amplitude Alfvén packets of the other Elsässer field. In this view, a difference between Elsässer energies modifies the nonlinear time $\tau_{\pm} \approx l/z^{\mp}$, and thereby also the time required for the deformation of

a larger packet by a smaller one. It is noteworthy that decaying MHD turbulence with a large initial alignment tends to a pure Alfvénic state (e.g. [Bis03]). This process is called dynamic alignment, and follows from different dissipation rates of total energy and cross-helicity. The dynamic alignment is characterized by an increase of the correlation coefficient, i.e. by an increase of the normalized value of the cross-helicity, $H^{\mathrm{C}}/(E^{\mathrm{k}}E^{\mathrm{m}})^{1/2}$ (e.g. [GLP83]).

In the following, a dynamical model that explains quasi-oscillations between the two turbulent states in 2D magnetoconvection is proposed.

It is assumed that at the beginning the system operates in the IK regime. This choice is not essential for the validity of the model, but only provides a convenient starting point for following considerations. The IK regime implies that energies and fluxes of Elsässer variables are approximately equal. Consequently, the total cross-helicity is small (see (5.14)), and the nonlinear transfer of the cross-helicity is very inefficient (nearly switched off, see (5.24)). Since almost no cross-helicity is supplied to small scales by a direct cascade, and moreover a qualitatively similar structure of $\mathbf{z}^+$ and $\mathbf{z}^-$ in the IK regime can be expected (balanced MHD turbulence), the small-scale dissipation of cross-helicity $-(\tilde{\nu}+\tilde{\eta})\int_S j\omega dS$ is very small as can be seen also from

$$-(\tilde{\nu}+\tilde{\eta})\int_S j\omega dS = (\tilde{\nu}+\tilde{\eta})\,\frac{1}{4}\int_S [(\nabla\times\mathbf{z}^-)^2-(\nabla\times\mathbf{z}^+)^2]dS \tag{5.25}$$

which is negligible in the IK regime. This fact is also supported by pinning effect (e.g. [LG03][Bis97][GLP83]). The pinning effect which manifests itself by equality of Elsässer energy spectra at dissipation scales is caused by the fact that the IK nonlinear transfer time of the Elsässer energy $E^+ \approx {z^+}^2$ depends on $E^- \approx {z^-}^2$ and vice-versa

$$\tau^{\pm}_{\mathrm{IK}} = \frac{v_{\mathrm{A}}l}{z^{\mp 2}} \tag{5.26}$$

Thus the IK nonlinear time of the field with higher energy is longer than the IK nonlinear time of the field with lower energy. Since at the dissipation scale $\tau_{\mathrm{D}} \approx \tau^{\pm}_{\mathrm{IK}}$ small-scale dissipation effects influence primarily the field with longer τ_{IK}, i.e. with higher energy, which energy is consequently more efficiently dissipated. This effect remains significant until the energies of both fields are at the dissipation scale approximately equal. The pinning effect can be seen on the l.h.s of Fig. 5.8 that shows the Elsässer energy spectra obtained by time-averaging over the IK phases. They are compensated by the IK factor $k^{1.5}$ (cf. (5.19)). The spectra coincide already from the wavenumber $k \approx 70$.

Interacting Alfvén packets are of similar amplitude in the IK regime, and nonlinear MHD interactions are dominant at inertial-range scales. Buoyancy forces play at inertial-range scales a dynamically negligible role in the IK regime. However, the source term $\int_S \theta b_z dS$ continuously pumps negative cross-helicity at large scales into the system. Since the dissipation of the cross-helicity is inefficient, and there is no other process that extracts the cross-helicity from the system, it accumulates at large scales, and consequently the absolute value of total cross-helicity increases. The growth of the cross-helicity breaks the balance between E^+ and E^-; the Elsässer energy E^- becomes larger than E^+. As a consequence, amplitudes of counter-propagating Alfvén wave packets differ as well as their Alfvén crossing times. This leads to a weakening of the nonlinear

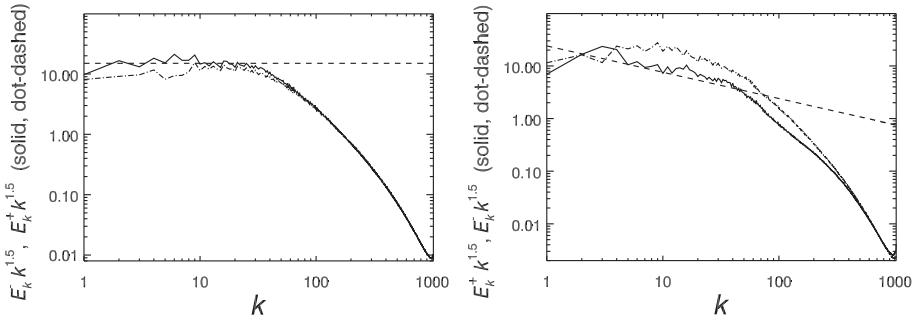

Figure 5.8: Spectra of E^+ and E^- in the IK phase (left) and in the BO-like phase (right). All spectra are compensated by the factor $k^{1.5}$. The dashed line in the BO-like case indicates the slope k^{-2}.

MHD interaction. Since the dissipation and large-scale effects are assumed to be negligible at intermediate scales, only buoyancy and nonlinear forces compete there. However, at this time the nonlinear MHD interactions are weak, so the inertial-range dynamics is dominated by buoyancy. Therefore, the dynamics of the system switches to the buoyancy dominated BO-like regime of turbulence.

In the BO-like regime, the spectral energy fluxes ϵ^+ and ϵ^- are different which implies that the spectral flux of cross-helicity ϵ^{C} (cf. (5.24)) begins to transport the cross-helicity efficiently. Moreover, the pinning effect is weak in the BO-like regime because the Elsässer energies cascade on the buoyancy time scale. Thus the difference between the spectra of E^+ and E^- penetrates to the smallest scales. This fact is demonstrated on the r.h.s. of Fig. 5.8 where the Elsässer energy spectra obtained by time-averaging over the BO-like phases are shown. Both spectra are compensated by the factor $k^{1.5}$ for comparison with the same spectra in the IK regime shown in Fig. 5.8 on the left. The slope of the inertial range of the spectrum of E^+ in the BO-like regime is found to be roughly k^{-2}, and it is indicated by the dashed line. This scaling exponent deviates from the BO value -2.2. Although there is no explanation for this deviation, it can be caused by measurements errors that are related to the absence of a pure BO state (see later remarks in subsection 5.4.4). In the spectrum of E^- no visible inertial range is detected. The Elsässer energy spectra are distinct even at very small scales around the wavenumber $k \approx 400$. This implies, according to the relation (5.25), that the small-scale dissipation of the cross-helicity increases, noteworthy, in accordance with the increase of the spectral transfer of the cross-helicity ϵ^{C}. Since the energy E^- dominates, the dissipation becomes positive. In this way, the BO-like regime allows an efficient dissipation of the accumulated cross-helicity. As the cross-helicity decreases, the energies E^+ and E^- become comparable again, so the effect of nonlinear MHD interactions is amplified, and the system returns into the IK regime of 2D magnetoconvective turbulence.

The proposed dynamical model is able to explain quasi-oscillations between the IK phases and the BO-like phases in two-dimensional magnetoconvection. All features of this model are successfully tested in the simulation with the resolution 2048^2 as well as in the simulation with the resolution 1024^2. In the following, several additional remarks are made in order to comment particular

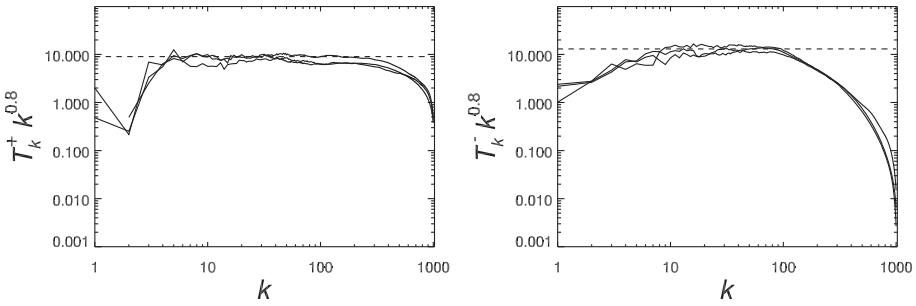

Figure 5.9: The scatter plot of transfer functions T_k^+ (left) and T_k^- (right) of Elsässer energy fluxes $\epsilon^\pm$ taken in several instants of time during the BO-like phases. All transfer functions are compensated by the Bolgiano-Obukhov factor $k^{4/5}$ predicted for hydrodynamic turbulent convection. Dashed lines indicate the ideal BO scaling $k^{-4/5}$.

aspects of the proposed model.

Remarks on the model

It is noteworthy that only nonlinear MHD interactions and buoyancy forces dominate the dynamics at inertial-range scales, and furthermore they compete at these scales. Therefore, although variations of the nonlinear MHD terms seem to play a crucial role, fluctuations of the vertical heat flux can intensify or weaken a particular turbulent regime.

Due to the dynamic development of the system, it is not possible to distinguish time intervals of the turbulent regimes exactly. Thus values obtained by time-averaging can be affected by errors coming from transition between the time intervals. It is therefore difficult to determine exactly a slope of energy spectra, especially in the BO-like phase for which no phenomenological prediction exists. It is observed that the inertial range of the kinetic energy spectrum can be slightly flatter than in Fig. 5.5, with a slope of k^{-2} instead of $k^{-2.2}$. This value would correspond to the slope of the inertial range of the E^+ spectrum in the BO-like phase (Fig. 5.8). The performed simulations do not have a sufficient resolution to solve this uncertainty.

Although the transfer functions in the BO-like phase shown in Fig. 5.6 follow the slope $k^{-0.2}$ at inertial-range scales, it is possible that due to the aforementioned reasons the time-averaging process could introduce errors. In fact, several particular instants of time are found when the spectra of both T_k^+ and T_k^- exhibit an inertial range with the scaling exponent $-4/5$ that would correspond to the BO prediction (cf. (3.14)). The spectra at these particular times are depicted in Fig. 5.9. The plot on the l.h.s. and the plot on the r.h.s. represent a scatter plot of T_k^+ and T_k^- in the BO-like phase, respectively. All transfer functions are compensated by the BO factor $k^{4/5}$. In contrast to T_k^-, the compensated transfer functions T_k^+ exhibit at intermediate scales a very extended interval of a constant value, $5 \lesssim k \lesssim 300$, that penetrates to the smallest scales. This is in approximate agreement with the calculated spectra of E^+ and E^- (Fig. 5.8)

where both curves coincide from $k \approx 300$ at very small scales. At inertial-range scales, on the contrary, the energy spectra, the transfer functions and also the structure functions (see later) of E^+ and E^- differ in the BO-like regime considerably. This fact can be explained by unequal impacts of buoyancy forces on the Elsässer fields. The particular form of the buoyancy term influencing the evolution of E^+ is $\theta z_z^+ = \theta(v_z + b_z)$ (cf. (5.12)), whereas in the case of E^- the buoyancy term reads $\theta z_z^- = \theta(v_z - b_z)$. Therefore, although the turbulent heat flux θv_z affects both Elsässer fields similarly, its effect on E^+ and E^- can be largely modified at locations of strong vertical magnetic fields. This effect is also related to different amplitudes of the Elsässer fields in the BO-like regime, in contrast to the IK regime where these amplitudes are comparable and buoyancy effects negligible. However, all transfer functions in Fig. 5.9 are positive at all scales, so both E^+ and E^- are transported by a direct cascade from large to small scales.

The quasi-oscillations between both turbulent regimes occur approximately on the time scale of several typical buoyancy times, i.e. on the typical dynamical time scale. This is in agreement with the fact that the transition from the IK regime to the BO-like regime reduces the cross-helicity, and therefore immediately weakens the newly establishing BO-like regime. Thus a time interval of the BO-like regime is no longer than several units of the typical dynamical time. The situation is similar for the transition from the BO-like regime to the IK regime. Therefore, none of both turbulent regimes has enough time to establish itself for a time interval longer than several units of the typical buoyancy time.

The proposed model represents only one plausible explanation. It is not excluded that the quasi-oscillations are caused by a different mechanism. However, the permanent growth of the total cross-helicity in the IK regime and the depletion of the total cross-helicity in the BO-like regime should be taken into account by any other model.

Finally, one interesting picture in DNS turbulence research obtained from the performed high resolution simulation is presented in Fig. 5.10. It shows the kinetic energy spectrum taken at a particular time during the transition from the BO-like regime to the IK regime. The spectrum at intermediate scales resembles two inertial subranges observable at the same time. A BO-like inertial subrange with the scaling exponent -2.2 is visible at larger intermediate scales, while smaller intermediate scales have been already adjusted to the IK dynamics, so the spectrum at these scales resembles an inertial subrange with the scaling exponent -1.6. Generally, inertial-range scaling begins to change always at small scales first because their dynamical time is shorter compared to larger scales. It is noteworthy that the calculated Bolgiano length L_B given by (1.25) is about one order of magnitude larger than the size of the computational box, so it is located outside of the resolved spectral region. Therefore, it is supposed that relation (1.25) valid for hydrodynamic convection is not an appropriate estimate of the Bolgiano scale for magnetohydrodynamic systems where the impact of magnetic fields should be taken in account as well. The slope of the IK inertial subrange is very close to the value -1.66 rather than to the IK value -1.5. It is unclear what kind of scaling, if any, the kinetic energy spectrum should exhibit in MHD simulations. The IK phenomenology predicts the scaling for the total energy spectrum since it is a conserved quantity in the ideal case, whereas

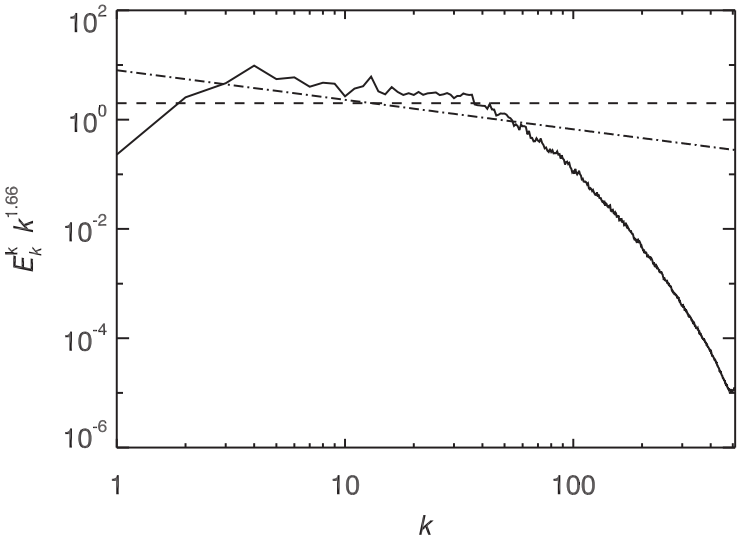

Figure 5.10: The compensated kinetic energy spectrum E^{k}_k taken at a particular time during the transition from the BO-like regime to the IK regime. The spectrum resembles two inertial subranges observed simultaneously. The skewed dashed line indicates the slope $k^{-2.2}$ whereas the horizontal dashed line indicates the slope $k^{-1.66}$.

the kinetic energy is not. However, both subranges with different slopes are clearly visible. This spectrum is presented only for curiosity since in numerical simulations due to insufficient computational power it is usually difficult to observe a clear inertial range at all, and the more so two inertial subranges at the same time.

The proposed model does not depend on the specific realization of the driving force that injects the cross-helicity. A similar mechanism based on amplifying and weakening of nonlinear MHD interactions in two-dimensional MHD turbulence due to some driving force might be applicable in cases where quasi-oscillations between different turbulent regimes are observed or in cases where an implementation of these quasi-oscillations would be useful. The two-dimensional MHD approximation can be applied e.g. for three-dimensional MHD systems with strong mean magnetic fields.

5.5 Structure functions

Another possibility how to determine scaling properties of individual fields is to analyze the behavior of their structure functions at inertial-range scales (see section 3.4, 4.4). The time-averaged second order structure functions $\hat{S}_2^+$, $\hat{S}_2^-$ and $\hat{S}_2^\theta$ obtained from the performed simulation are depicted in Fig. 5.11. The results obtained by time-averaging over the IK phases are plotted on the l.h.s. of the figure, whereas the results obtained by time-averaging over the BO-like phases are plotted on the r.h.s. of the same figure. Inserts in each figure

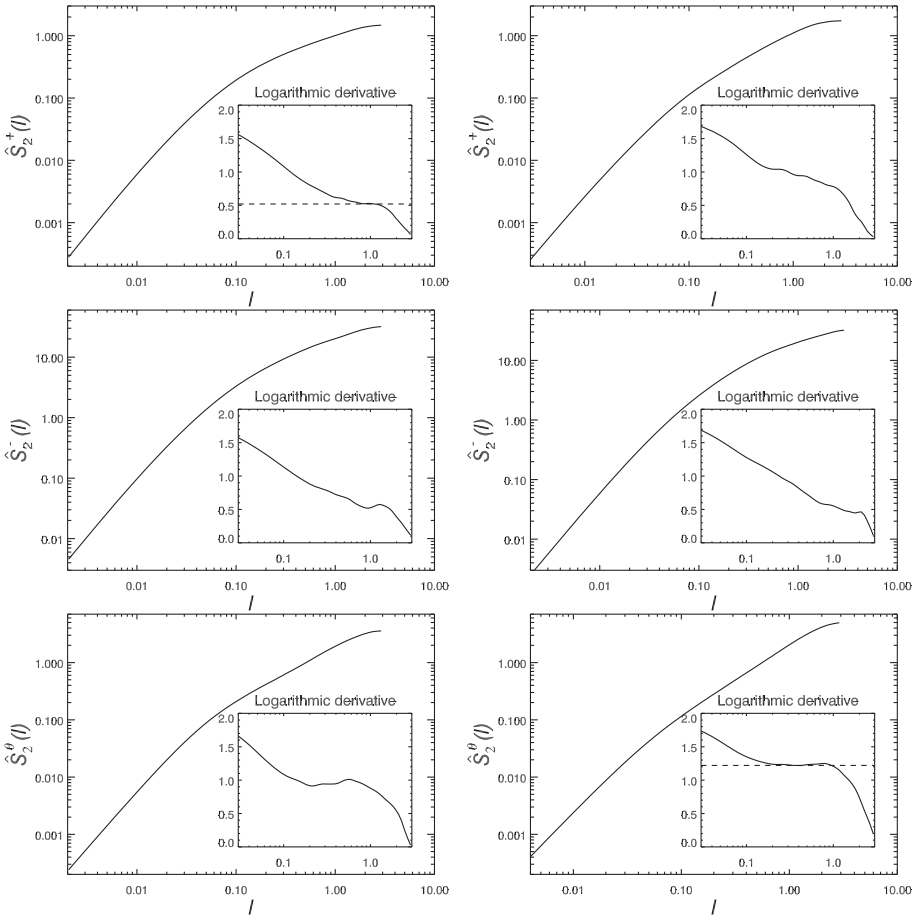

Figure 5.11: Time-averaged second order structure functions $\hat{S}_2^+$, $\hat{S}_2^-$ and $\hat{S}_2^\theta$ obtained from the IK regime (left) and from the BO-like regime (right) of 2D turbulent magnetoconvection. All structure functions are normalized by the corresponding energy, $E^{+,-,\theta}$. Inserts display the logarithmic derivatives of the corresponding structure functions. The uppermost pictures show the structure functions $\hat{S}_2^+(l)$ of the Elsässer field $\mathbf{z}^+$. In the middle, the structure functions $\hat{S}_2^-(l)$ of the field $\mathbf{z}^-$ are depicted. The lowermost plots show the structure functions $\hat{S}_2^\theta(l)$ of the temperature field θ.

display the logarithmic derivatives of the corresponding structure functions. All structure functions are normalized by the corresponding energy, $E^{+,-,\theta}$.

The uppermost figures show the structure functions $\hat{S}_2^+(l)$ of the Elsässer field $\mathbf{z}^+$. The functions $\hat{S}_2^+(l)$ in the IK case exhibits a short self-similar range at intermediate scales, $0.7 \lesssim l \lesssim 1.5$. The logarithmic derivative displays a short plateau in front of the large-scale fall-off. The horizontal dashed line indicates this region. The scaling exponent of this range is estimated as $\zeta_2^+ = 0.52 \pm 0.1$. This value is in agreement with the IK prediction for 2D MHD turbulence.

The situation in the BO-like regime is less clear. The structure function $\hat{S}_2^+(l)$ is at intermediate scales noisy, so it does not allow to determine any self-similar range. This is confirmed by the plot of the logarithmic derivative. No evident plateau can be found there, and no unique scaling exponent can be associated with it. However, a small horizontal interval located at $0.15 \lesssim l \lesssim 0.25$ that suggests a scaling exponent $\zeta_2^+ \approx 1$ would be in agreement with the computed spectrum of E^+ in the BO-like regime (Fig. 5.8) which exhibits inertial-range scaling k^{-2}. Moreover, a comparison between $\hat{S}_2^+(l)$ in both regimes gives an impression of the qualitative difference between both turbulent regimes.

The middle row displays plots of structure functions $S_2^-(l)$ of the Elsässer field $\mathbf{z}^-$. Both functions are quite similar. This holds for their logarithmic derivatives as well. Although they do not exhibit any plateau, a sharp transition from intermediate to large scales, especially in the BO-like regime, suggest that the scaling exponent has in both cases a value $\zeta_2^- \approx 0.5$. While such a exponent is foreseen for the IK regime, the same exponent is unexpected in the BO-like case. Moreover, the difference between $S_2^+(l)$ and $S_2^-(l)$ in the BO-like case is evident. In fact, this feature can be detected throughout the obtained results, e.g. in the spectra (Fig. 5.8) or in the transfer functions (Fig. 5.9), in both performed simulations. It is probably related to different amplitudes of both Elsässer fields and different impacts of buoyancy effects on these fields (see remarks in subsection 5.4.4). Furthermore, difficulties to determine exact time intervals of both regimes might play a role in the averaging process (see the same remarks in 5.4.4).

The lowermost plots show the second order structure functions $S_2^\theta(l)$ of the temperature field. Despite the fact that $S_2^\theta(l)$ in the IK case seems to exhibit a self-similar range extended over about one decade, its logarithmic derivative shows that this range is significantly deformed. Despite the fact that no exact scaling exponent can be associated with it, a value close to 1 seems to be very probable (cf. Fig. 5.2). On the contrary, the structure $S_2^\theta(l)$ in the BO-like case shows a clearly visible self-similar range in the region $0.2 \lesssim l \lesssim 1$. The scaling exponent can be identified from the plot of the logarithmic derivate, $\zeta_2^\theta = 1.2 \pm 0.19$. Although this value is larger than that determined from the entropy spectrum (≈ 1, see Fig. 5.5), the difference is with respect to the measurement errors acceptable.

All higher order structure functions are largely affected by statistical noise, and are therefore not shown here. The only exception is structure functions $S_p^+(l)$ of $\mathbf{z}^+$ obtained from the IK regime. Hence they are used to evaluate intermittency effects in the IK regime of 2D magnetoconvective turbulence.

Order p	ζ_p^+/ζ_2^+
2	1
3	1.31 ± 0.04
4	1.49 ± 0.05
5	1.60 ± 0.07
6	1.68 ± 0.09
7	1.72 ± 0.12
8	1.75 ± 0.14

Table 5.1: Relative scaling exponents ζ_p^+/ζ_2^+ of the structure functions $S_p^+(l)$ in the performed simulation of 2D magnetohydrodynamic convection up to the order $p = 8$. The exponents are obtained via ESS.

Generally, it is difficult to determine exact values of scaling exponents of structure functions in simulations of 2D magnetohydrodynamic convection. This behavior is given by the dynamic character of the flow. In every time step the instantaneous BO-like turbulent regime is influenced by the IK regime and vice versa (see remarks in subsection 5.4.4).

5.6 Intermittency

The higher order structure functions $S_p^+(l)$ of the Elsässer field $\mathbf{z}^+$ in the IK regime are used to compute intermittency corrections to the Iroshnikov-Kraichnan scaling $l^{p/4}$. The relative scaling exponents are evaluated via extended self-similarity up to the order $p = 8$. The values of the relative scaling exponents are summarized in Tab. 5.1.

In Fig. 5.12 they are plotted as a function of order p. The values obtained from the performed simulation are denoted by diamonds. The solid line indicates the nonintermittent IK scaling $l^{p/4}$ (cf. (5.19)). The dashed line shows the prediction of the She-Lévêque model modified for IK turbulence (e.g. [PP95], see also subsection 6.4.3)

$$\zeta_p^{\mathrm{IK}} = \frac{p}{8} + 1 - \left(\frac{1}{2}\right)^{p/4}. \tag{5.27}$$

The dot-dashed line displays the prediction of the She-Lévêque model modified for 3D MHD turbulence (e.g. [MB00], see also subsection 6.4.3)

$$\zeta_p^{\mathrm{MHD}} = \frac{p}{9} + 1 - \left(\frac{1}{3}\right)^{p/3}. \tag{5.28}$$

Other depicted values are results obtained from numerical simulations of 2D MHD turbulence: triangles and squares are relative exponents of $S_p^+(l)$ and $S_p^-(l)$, respectively, ([PPC98], $\mathsf{Re} \approx 4400$), crosses are results of Lagrangian averaged 2D MHD simulations ([GHM06], $\mathsf{Re} \approx 2200$, $\mathsf{Pr_m} = 1$).

The computed exponents do not coincide with any of the presented phenomenological intermittency models. They exhibit larger deviations from the predicted

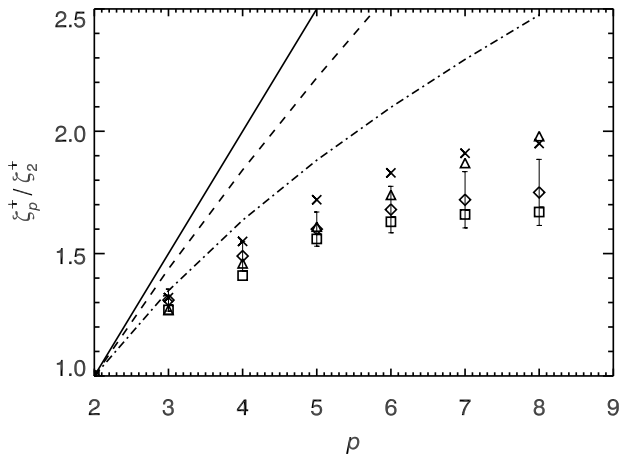

Figure 5.12: Relative scaling exponents ζ_p^+/ζ_2^+ (diamonds) of the structure functions S_p^+ obtained from the IK regime. The solid line corresponds to the non-intermittent IK scaling $l^{p/4}$ (cf. (5.19)). The dashed line and the dot-dashed line show predictions of She-Lévêque models (5.27) and (5.28), resp. Triangles and squares denote relative exponents of $S_p^+(l)$ and $S_p^-(l)$, resp., obtained from numerical simulations of 2D MHD turbulence ([PPC98]). Crosses denote results from Lagrangian averaged 2D MHD turbulence simulations ([GHM06]).

models already at the order $p = 4$. No other phenomenological models for IK turbulence are currently available. On the contrary, the values from different numerical simulations display a quite similar behavior, although a small difference between them can be detected for orders larger than $p = 6$.

Generally, a calculation of higher order exponents is affected by increasing statistical errors (see Tab. 5.1) since higher order structure functions are more sensitive to statistical noise. However, with respect to the computed error bars, the $\mathbf{z}^+$ field in the IK regime of 2D magnetoconvection behaves in approximate agreement with other 2D MHD systems. This fact supports the identification of this regime as the Iroshnikov-Kraichnan MHD turbulence.

5.7 Spatial structure

In this section the real space structure of several physical quantities in both regimes of two-dimensional magnetoconvective turbulence is visualized in order to allow for a comparison between them. Figures from the IK regime are taken at $t = 4$. They are shown always in the left column. Figures from the BO-like regime are taken at $t = 8$. They are shown always in the right column.

Fig. 5.13 displays pictures of several large-scale quantities. The uppermost plots display the temperature field (light color – high values, dark color – low values) together with the velocity field (black arrows) and the magnetic field (green

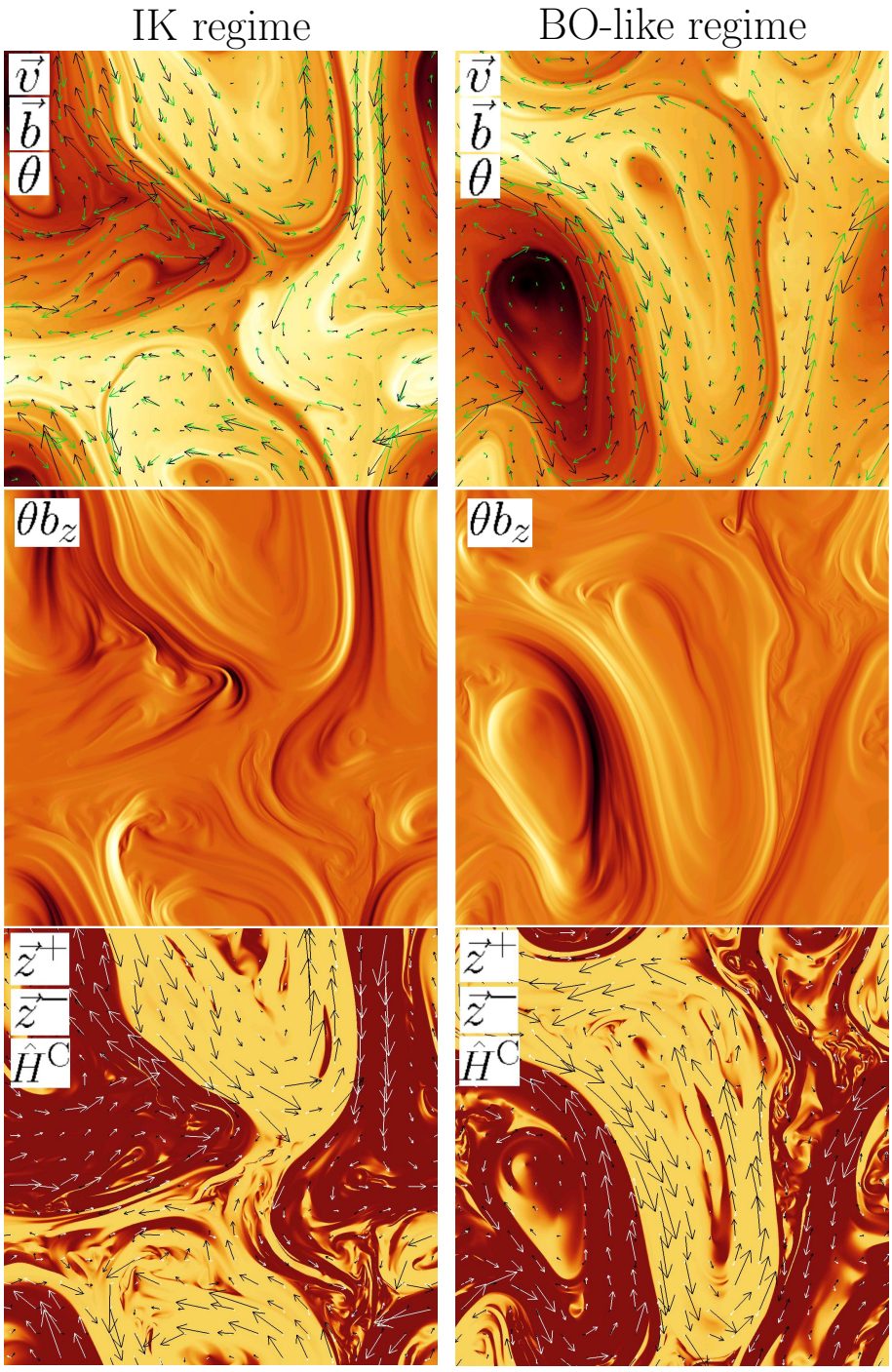

Figure 5.13: Top: The temperature field, the velocity field (black arrows) and the magnetic field (green arrows). Middle: The driving term of the cross-helicity θb_z. Bottom: The normalized correlation coefficient $\widehat{H}^{\mathrm{C}} = H^{\mathrm{C}}/(E^{\mathrm{k}}E^{\mathrm{m}})^{1/2}$ together with Elsässer fields $\mathbf{z}^+$ (black arrows) and $\mathbf{z}^-$ (white arrows). Magnitudes of the scalar fields are denoted by color (light – high values, dark – low values. Columns correspond to the quantities in the IK regime (left) and in the BO-like regime (right).

arrows). In hot rising blobs of the fluid both vector fields are highly aligned. On the contrary, in cold sinking blobs the vector fields point almost exactly in opposite directions. Furthermore, both vector fields assume the largest values on borders of blobs close to transition regions where strong shearing motions between individual blobs appear.

The plots in the middle display the spatial distribution of the cross-helicity driving term θb_z (cf. (5.23)). Regions with the highest amplitudes are located in the outer parts of the blobs where the magnetic field assumes the largest values.

In the lowermost figures the correlation coefficient $\widehat{H}^{\mathrm{C}} = H^{\mathrm{C}}/(E^{\mathrm{k}}E^{\mathrm{m}})^{1/2}$ is depicted (light color – high values, dark color – low values) together with the Elsässer fields $\mathbf{z}^+$ (black arrows) and $\mathbf{z}^-$ (white arrows). The flow is divided into two principal parts. Hot blobs of the fluid are dominated by the field $\mathbf{z}^+$ and high positive correlations, whereas cold blobs are dominated by the field $\mathbf{z}^-$ and high negative correlations. The system seems to be in both regimes well ordered. The normalized correlation coefficient computed from absolute values of the cross-helicity, $< |\mathbf{v} \cdot \mathbf{b}| > /(E^{\mathrm{k}}E^{\mathrm{m}})^{1/2}$, remains quasi-stationary during the simulation time, and fluctuates around 90%. This observation is in good agreement with the proposed model of the quasi-oscillations since such a high level of correlation is required to weaken the nonlinear MHD interactions in MHD systems (e.g. [GLP83][GFP82]).

Fig. 5.14 shows spatial structures of three small-scale quantities. These are the vorticity, the current density and the term $j\omega$. All quantities are shown in gray scale representation (white – high values, black – low values). They indicate places where dissipation of different fields primarily occurs. In the uppermost pictures the vorticity field is depicted. It forms thin elongated quasi-one-dimensional filaments close to transitions between individual blobs. There, the most of the kinetic energy is dissipated. The plots in the middle show the current density. The largest values of the current density are distributed also in elongated quasi-one-dimensional filaments. They represent places where the magnetic energy is dissipated. High current density is located at similar places as high vorticity which is caused by strong shearing motions between individual blobs. In contrast to that, inner part of blobs are characterized by an almost uniform distribution of the velocity field and of the magnetic field (see Fig. 5.13). Therefore, only a smart part of the associated energies is dissipated there. For comparison purposes, the lowermost pictures display the product of both fields, $j\omega$, i.e. the term that is responsible for the dissipation of cross-helicity (cf. (5.23)).

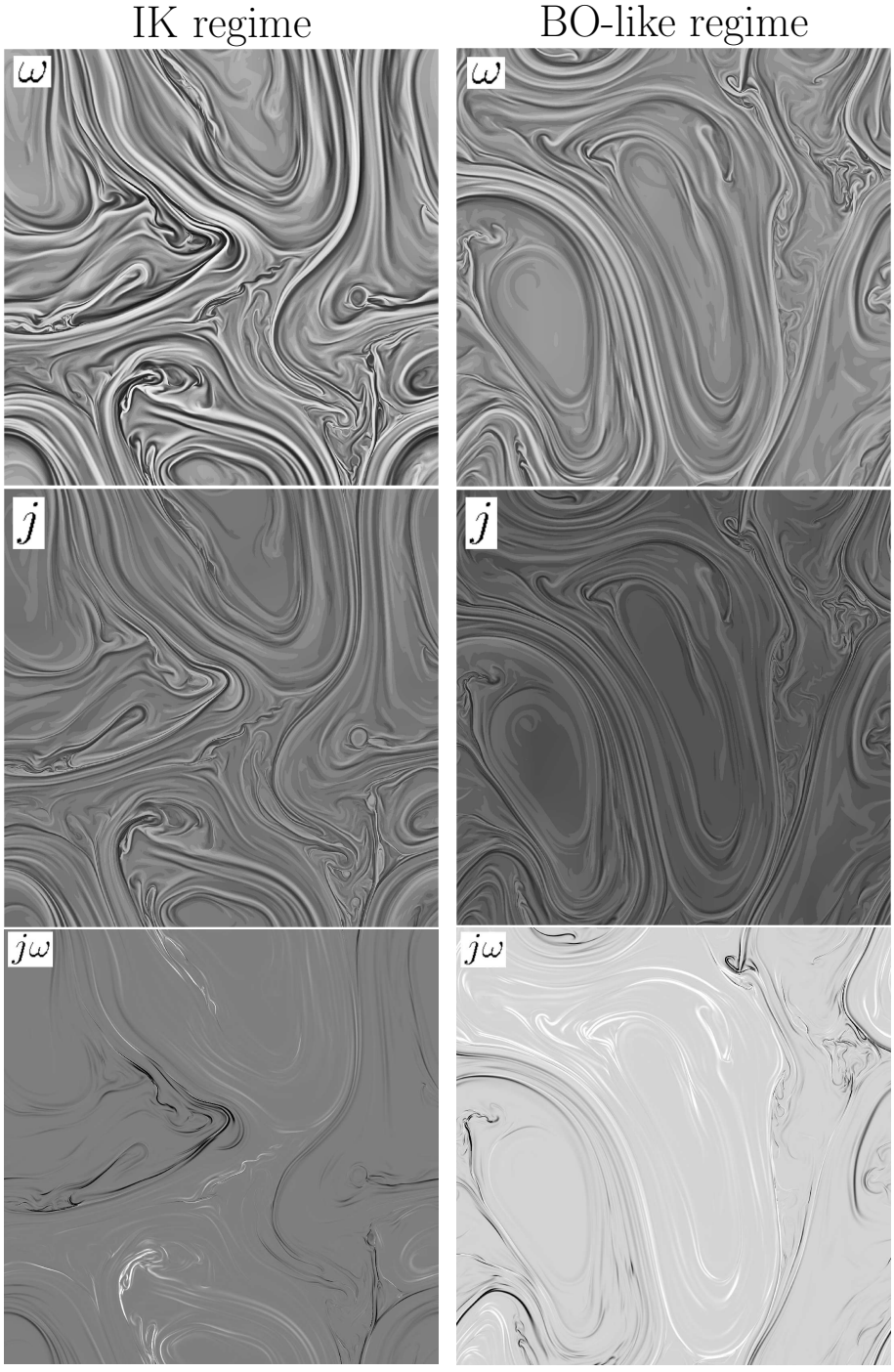

Figure 5.14: Top: the vorticity field, i.e. locations of the kinetic energy dissipation. Middle: the current density, i.e. locations of the magnetic energy dissipation. Bottom: the term $j\omega$ responsible for the cross-helicity dissipation. All quantities are shown in gray scale representation (white – high values, black – low values). Columns correspond to the quantities in the IK regime (left) and in the BO-like regime (right).

Chapter 6

3D magnetohydrodynamic convection

Three-dimensional magnetoconvection describing fully three-dimensional convective flows in plasmas exhibits a high level of complexity, especially when compared to the previously studied cases. The velocity field experiences, apart from inertial and buoyancy forces, the Lorentz force that affects its dynamics. At the same time the velocity field reacts back influencing the evolution of the magnetic field. This leads to a complicated nonlinear interplay between all three fields, i.e. temperature, velocity and magnetic field, as well as to a continuous exchange of energy between them. The nonlinear dynamics of such a system is difficult to analyze, especially when a nonlocal transport of energies in spectral space cannot be ruled out. Motions of plasma in three-dimensional magnetoconvection are not restricted to a two-dimensional plane as in the setup studied in the previous chapter, so the convective flow is able to explore the third direction dragging the magnetic field with it. Thus magnetic field become twisted and stretched receiving energy from the velocity field. Such motions are supposed to be responsible for an amplification of magnetic energy, a process called small-scale turbulent dynamo. However, this work does not focus on the amplification process itself, but investigates the resulting nonlinearly saturated turbulent state and the effects of the driving of turbulence by mean temperature gradient.

Direct numerical simulations of three-dimensional magnetoconvection deal with the evolution of 7 nonlinear partial differential equations in the three-dimensional space. Therefore, they require an enormous computational effort that explores limits of modern supercomputers. Since the maximal Rayleigh number achieved in the computationally less expensive 3D hydrodynamic convection studied in chapter 4 is approximately $\mathsf{Ra} \approx 2 \cdot 10^7$, it can be expected that the maximal Rayleigh number in a computationally more expensive simulation of 3D magnetoconvection with the same computational resources will be lower. However, as the interesting results of the previous chapter indicate, the nonlinear dynamics of turbulent convection in electrically conducting fluids differ from that of hydrodynamic convection significantly. Therefore, it is very important to numerically analyze three-dimensional magnetoconvection and understand

consequences of convective motions in plasmas.

6.1 Role of the magnetic field

6.1.1 Ideal invariants

The dynamical evolution of three-dimensional magnetoconvection is governed by the set of equations (1.16)–(1.20) already introduced in subsection 1.2.2. In the case of pure magnetohydrodynamics, i.e. without buoyancy effects, there exist three ideal invariants

$$E^{\mathrm{tot}} = \int_V \frac{1}{2}(v^2 + b^2) dV, \tag{6.1}$$

$$H^{\mathrm{C}} = \int_V \mathbf{v} \cdot \mathbf{b}\, dV, \tag{6.2}$$

$$H^{\mathrm{M}} = \int_V \mathbf{a} \cdot \mathbf{b}\, dV \tag{6.3}$$

where E^{tot} is the total (kinetic and magnetic) energy, H^{C} is the cross helicity, H^{M} is the magnetic helicity, and $\mathbf{a}$ is the vector potential of magnetic field fluctuations. The total energy and the cross-helicity are transferred by a direct cascade from large to small scales, whereas the magnetic helicity is subject to an inverse cascade, and is transferred in the opposite direction from small to large scales (e.g. [Mof78][Bis97]).

Since buoyancy forces do not excite magnetic field fluctuations, but only drive the velocity field, the driving by a mean temperature gradient does not inject magnetic helicity into the system. Thus a value of magnetic helicity, if small initially, stays at a negligible level, so the ideal conservation of magnetic helicity does not constrain the evolution of the system. Despite the fact that E^{tot} and H^{C} are due to the driving not ideally conserved in a magnetoconvective system, based on the results of the previous chapter it is still reasonable to expect that the direction of their spectral transfer in the inertial range remains unaffected by buoyancy, i.e. direct. This assumption is verified later in the following sections. Furthermore, since it is predicted in the frame of MHD turbulence as well as of buoyancy dominated turbulence that the total energy spectrum exhibits scaling in the inertial range (e.g. [MB00][MG01][Bis03]), it is expected that the total energy spectrum preserves its scaling property also in three-dimensional magnetoconvection. However, energy spectra of individual fields are analyzed as well.

6.1.2 Conservative forms of the nonlinear terms

It follows from the structure of the individual equations in the set (1.16)–(1.20) that the nonlinear dynamics, especially of the magnetic field, differs in three-dimensional magnetoconvection considerably from the two-dimensional case. It is therefore important from the point of view of nonlinear dynamics to recall

the main consequence of this difference. The nonlinear terms from the equation for velocity fluctuations (cf. (1.16), (5.22)) multiplied by $\mathbf{v}$ can be expressed as

$$\mathbf{v} \cdot (-(\mathbf{v} \cdot \nabla)\mathbf{v} + \mathbf{j} \times \mathbf{b}) = -\mathbf{v} \cdot [(\mathbf{v} \cdot \nabla)\mathbf{v}] - \frac{1}{2}\nabla \cdot (b^2\mathbf{v}) + \mathbf{v} \cdot [(\mathbf{b} \cdot \nabla)\mathbf{b}] \quad (6.4)$$

where

$$-\mathbf{v} \cdot [(\mathbf{v} \cdot \nabla)\mathbf{v}] = -\frac{1}{2}\nabla \cdot (v^2\mathbf{v}), \quad (6.5)$$

$$\mathbf{v} \cdot [(\mathbf{b} \cdot \nabla)\mathbf{b}] = \nabla \cdot (\mathbf{v} \cdot \mathbf{bb}) - \mathbf{b} \cdot [(\mathbf{b} \cdot \nabla)\mathbf{v}]. \quad (6.6)$$

Similarly, the nonlinear term from the equation for magnetic field fluctuations (1.17) multiplied by $\mathbf{b}$ can be also reformulated, and reads

$$\mathbf{b} \cdot [\nabla \times (\mathbf{v} \times \mathbf{b})] = \mathbf{b} \cdot [(\mathbf{b} \cdot \nabla)\mathbf{v}] - \mathbf{b} \cdot [(\mathbf{v} \cdot \nabla)\mathbf{b}] \quad (6.7)$$

where

$$\mathbf{b} \cdot [(\mathbf{b} \cdot \nabla)\mathbf{v}] = \nabla \cdot (\mathbf{v} \cdot \mathbf{bb}) - \mathbf{v} \cdot [(\mathbf{b} \cdot \nabla)\mathbf{b}], \quad (6.8)$$

$$-\mathbf{b} \cdot [(\mathbf{v} \cdot \nabla)\mathbf{b}] = -\frac{1}{2}\nabla \cdot (b^2\mathbf{v}). \quad (6.9)$$

These relations imply an important difference with respect to the two-dimensional case. During the long-term evolution, the magnetic field can gain energy from the velocity field via the magnetic field stretching term on the l.h.s. of (6.8). This means that the equation for the magnetic potential contains a source term, so it cannot be expressed in the form of an advection-diffusion equation as in the two-dimensional case (cf. (5.6)). The stretching term is necessary for the operation of a turbulent magnetic dynamo. It is noteworthy that the second term on the r.h.s. of (6.8) is identical to the term on the l.h.s. of (6.6). Therefore, the terms that exchange energy, i.e. the terms on the l.h.s. of (6.6) and (6.8), summed together can be expressed in a divergence form. This means that the energy is exchanged between the velocity and the magnetic field, and is conserved during this process. Moreover, in the limit of infinite electrical conductivity the magnetic flux through a surface moving with the fluid remains constant, i.e. magnetic field is "frozen" into the velocity field (e.g. [Mof78][Mes99]).

The results in the following sections are computed from a direct numerical simulation of a three-dimensional magnetoconvective system driven by a mean horizontal temperature gradient in a cubic box with resolution 512^3. Dissipation coefficients of this run are $\tilde{\nu} = \tilde{\eta} = \tilde{\kappa} = 1.5 \cdot 10^{-3}$. They correspond to a nominal Rayleigh number $\mathsf{Ra} \approx 4.5 \cdot 10^5$. The Prandtl number and the magnetic Prandtl number are equal to 1. Since the dissipation coefficients have the same value, the Reynolds number and the magnetic Reynolds number are equal, $\mathsf{Re} = \mathsf{Re_m} \approx 870$. The system is evolved for approximately 4 typical buoyancy times. This value might seem to be small, but it is given by limited computational resources. However, such a time interval is large enough to obtain reasonable statistical averages of physical quantities at intermediate and small scales.

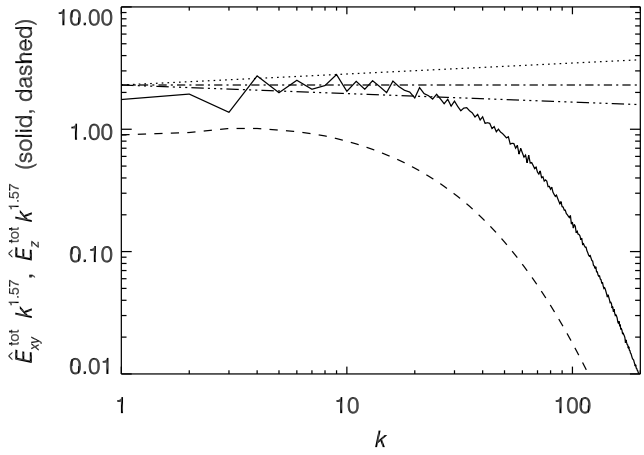

Figure 6.1: Time-averaged horizontal and vertical spectra of the total energy, $\hat{E}_{xy}^{\rm tot}$ and $\hat{E}_{z}^{\rm tot}$, respectively. The spectra are normalized by the total energy dissipation rate $\varepsilon_{\rm tot}^{2/3}$, and are compensated by the factor $k^{1.57}$. The horizontal dot-dashed line indicates a spectral slope $k^{-1.57}$. The dotted line denotes Iroshnikov-Kraichnan scaling $k^{-1.5}$. The triple-dot-dashed line indicates Kolmogorov scaling $k^{-1.66}$.

6.2 Spectra

6.2.1 Energy spectra

Fig. 6.1 shows time-averaged horizontal and vertical spectra of the total energy, $\hat{E}_{xy}^{\rm tot}$ and $\hat{E}_{z}^{\rm tot}$, respectively. The horizontal spectrum of the total energy is defined as

$$E_{xy}^{\rm tot}(k) \equiv \int_{\forall \mathbf{k}} E^{\rm tot}(\mathbf{k})|_{k=k_x^2+k_y^2} d\mathbf{k}. \tag{6.10}$$

The vertical spectrum $E_z^{\rm tot}$ is defined analogously to one-dimensional spectra in chapter 4 (see (4.4)). Both total energy spectra are normalized by the total energy dissipation rate $\varepsilon_{\rm tot}^{2/3}$ according to the predictions for a Kolmogorov-like regime of turbulence (cf. (1.29)). The total energy dissipation rate consists of contributions from the kinetic and the magnetic energy, $\varepsilon_{\rm tot} = \varepsilon_v + \varepsilon_m = \tilde{\nu} \int_V \omega^2 dV + \tilde{\kappa} \int_V j^2 dV$. The spectra are compensated by the factor $k^{1.57}$ which makes the inertial range of the horizontal total energy spectrum almost horizontal, and thereby clearly visible. The horizontal dot-dashed line denotes the slope $k^{-1.57}$. The dotted line indicates Iroshnikov-Kraichnan scaling $k^{-1.5}$. The triple-dot-dashed line shows Kolmogorov scaling $k^{-1.66}$. The spectra demonstrates that the investigated system exhibits a high level of anisotropy between the vertical and horizontal directions. The spectrum $\hat{E}_z^{\rm tot}$ shows that in the vertical direction nonlinear MHD interactions are largely damped by dissipation, so the associated inertial range is not observed. On the contrary, the

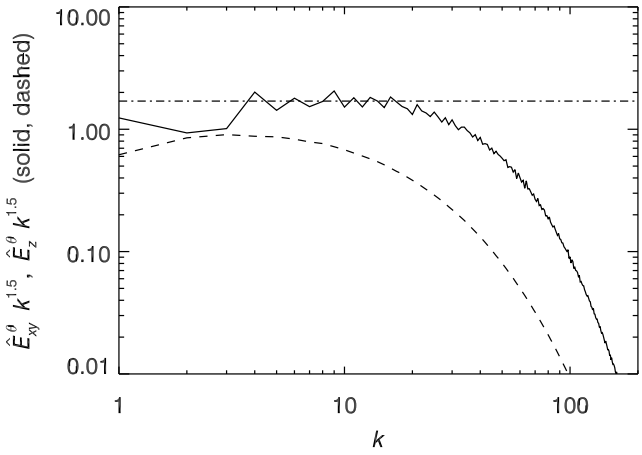

Figure 6.2: Time-averaged horizontal and vertical spectra of the temperature energy, $\hat{E}^{\theta}_{xy}$ and $\hat{E}^{\theta}_{z}$, respectively. The spectra are normalized by the factor $\varepsilon_\theta \varepsilon_v^{-1/3}$, and are compensated by $k^{1.5}$. The horizontal dot-dashed line indicates a spectral slope $k^{-1.5}$.

horizontal spectrum $\hat{E}^{\rm tot}_{xy}$ exhibits an inertial range extended over about half a decade in wavenumber $4 \lesssim k \lesssim 18$. The difference between the horizontal and the vertical spectrum penetrates to dissipation scales, and there is no tendency to isotropy at intermediate scales due to nonlinear turbulent mixing as in the previously studied 3D hydrodynamic convection (cf. Fig. 4.1). The scaling exponent -1.57 of the inertial range of the horizontal total energy spectrum is between the Iroshnikov-Kraichnan value of $-3/2$ (cf. (5.20), the scaling indicated by the dotted line in the plot) and the Kolmogorov value of $-5/3$ (the scaling indicated by the triple-dot-dashed line in the plot). However, the extension of the inertial range is very short, so the uncertainty by determining the scaling exponent is relatively large. It should be kept in mind that both predicted scaling exponents differ only by $1/6 \approx 0.17$. Furthermore, there is no general agreement on the inertial-range scaling of the total energy spectrum in 3D MHD turbulence. Results of simulations of isotropic MHD turbulence as well as solar wind measurements suggest Kolmogorov-like scaling $k^{-5/3}$ (e.g. [BM00][HBD03][MG05][BKM05]), whereas numerical simulations of anisotropic MHD turbulence favor Iroshnikov-Kraichnan scaling $k^{-3/2}$ (e.g. [MG01]). More recently, several works have appeared that provide a consistent explanation of this discrepancy (e.g. [Bol06][Gog06]).

A similar level of anisotropy between the vertical and horizontal directions can be observed also in Fig. 6.2 which shows time-averaged horizontal and vertical spectra of the temperature energy, $\hat{E}^{\theta}_{xy}$ and $\hat{E}^{\theta}_{z}$, respectively. Both temperature energy spectra are normalized by the factor $\varepsilon_\theta \varepsilon_v^{-1/3}$ according to the passive scalar scaling (cf. (1.32)), and are compensated by the factor $k^{1.5}$ which makes the inertial range of the spectrum $\hat{E}^{\theta}_{xy}$ horizontal. Also in this case the

anisotropy prevails to the smallest scales, and the nonlinear interactions in the vertical direction are largely damped. The scaling exponent of the inertial range of the horizontal temperature spectrum is determined approximately as -1.5. This value differs from the expected exponent -1.66 predicted for inertial-range scaling of passively advected scalars (cf. (1.32)). However, there is no straightforward explanation of this difference available. Thus the additional analysis in the later sections is necessary to elucidate the picture of 3D magnetoconvective turbulence.

Although the proposed mechanism of quasi-oscillations between different turbulent regimes that is described in section 5.4.4 in the previous chapter can be applied also to the three-dimensional case, no such phenomenon is observed in the performed simulation of 3D magnetoconvective turbulence. This fact can be caused by several reasons. The nominal Rayleigh number of the 3D simulation is smaller than that of the 2D simulation, $\mathsf{Ra_{3D}} \approx 10^5 < \mathsf{Ra_{2D}} \approx 10^6$, leading to weaker buoyancy effects in the 3D simulation compared to the 2D simulation. The 3D system evolves for only 4 typical buoyancy times compared to 15 typical buoyancy times in the 2D case, so the quasi-oscillations might not be detected. The nonlinear processes of MHD turbulence can differ in 3D and 2D. Probably the most important is the fact that a sufficient alignment between velocity and magnetic field can be more easily achieved in two dimensions than in three dimensions because the dynamics in 2D is restricted only to the two-dimensional plane.

6.2.2 Individual fields

Although inertial-range scaling in MHD turbulence is predicted for the spectrum of the total energy because the total energy is in nonlinear MHD interactions conserved, it is interesting to study energy spectra of individual fields. In Fig. 6.3 time-averaged horizontal and vertical kinetic energy spectra, $\hat{E}^{\mathrm{k}}_{xy}$ and $\hat{E}^{\mathrm{k}}_{z}$ are depicted, respectively. The spectra are normalized by the kinetic energy dissipation rate $\varepsilon_v^{2/3}$ (cf. (1.29)), and are compensated by the factor $k^{1.5}$. The horizontal dot-dashed line in the plot indicates a spectral slope $k^{-1.5}$. Additionally, time-averaged horizontal and vertical magnetic energy spectra, $\hat{E}^{\mathrm{m}}_{xy}$ and $\hat{E}^{\mathrm{m}}_{z}$, respectively, are plotted in Fig. 6.4. The magnetic energy spectra are normalized by the magnetic energy dissipation rate $\varepsilon_m^{2/3}$ (cf. (1.29)), and are compensated by the factor $k^{1.66}$. The horizontal dot-dashed line in the plot shows a spectral slope $k^{-1.66}$. Both plots suggest that the anisotropy influences the kinetic as well as the magnetic part of the total energy spectrum. In contrast to the vertical spectra of both energies, the horizontal spectra exhibit a short inertial range that is extended over about half a decade in wavenumber $4 \lesssim k \lesssim 18$. While the horizontal kinetic energy spectrum displays the inertial interval with a scaling exponent approximately -1.5 which is the Iroshnikov-Kraichnan value, a scaling exponent of the inertial range of the horizontal magnetic energy spectrum is close to the Kolmogorov value -1.66. Thus the horizontal spectra indicate a qualitative difference in the spectral behavior of the velocity and the magnetic field. It is interesting that the inertial intervals of the horizontal spectra of individual fields resemble the phenomenologically predicted scaling, namely $k^{-5/3}$ and $k^{-3/2}$ (cf. (1.29) and (5.20)). However, there is no direct relation

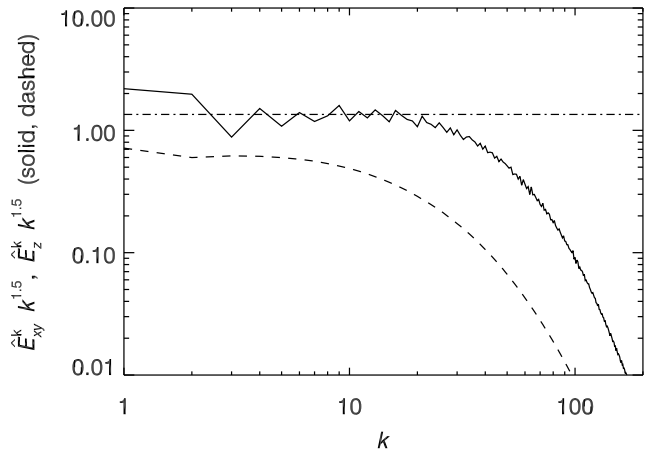

Figure 6.3: Time-averaged horizontal and vertical spectra of the kinetic energy, $\hat{E}^{\rm k}_{xy}$ and $\hat{E}^{\rm k}_{z}$, respectively. Both spectra are normalized by the kinetic energy dissipation rate $\varepsilon_v^{2/3}$, and are compensated by the factor $k^{1.5}$. The horizontal dot-dashed line indicates a spectral slope $k^{-1.5}$.

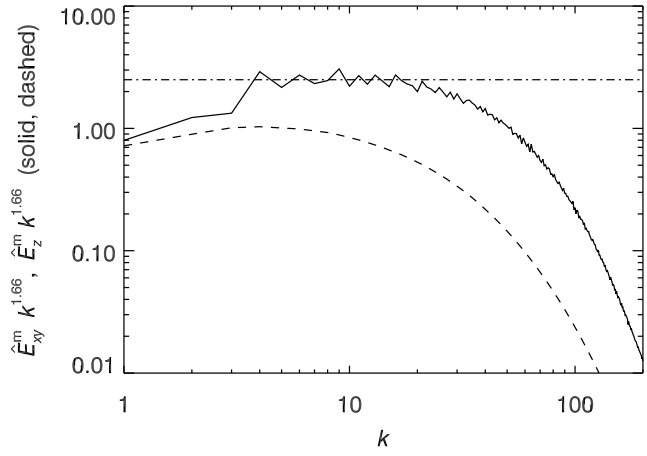

Figure 6.4: Time-averaged horizontal and vertical spectra of the magnetic energy, $\hat{E}^{\rm m}_{xy}$ and $\hat{E}^{\rm m}_{z}$, respectively. Both spectra are normalized by the magnetic energy dissipation rate $\varepsilon_m^{2/3}$, and are compensated by the factor $k^{1.66}$. The horizontal dot-dashed line indicates a spectral slope $k^{-1.66}$.

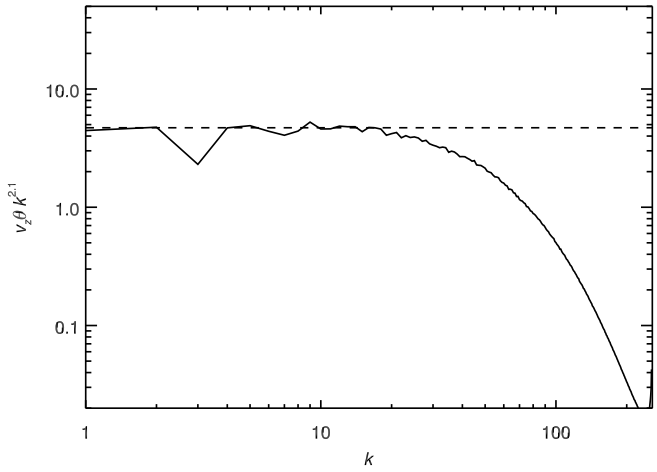

Figure 6.5: The time-averaged spectrum of the vertical heat flux $v_z\theta$ compensated by the factor $k^{2.1}$. The horizontal dashed line indicates a spectral slope $k^{-2.1}$.

between the observed scaling exponents and the phenomenologically predicted exponents since these are originally derived for the spectrum of the total energy.

The time-averaged spectrum of the vertical heat flux $v_z\theta$ is plotted in Fig. 6.5. In this case the determination of an exact scaling exponent is very difficult. The horizontal dashed line in the figure indicates a spectral slope $k^{-2.1}$ to which the spectrum at intermediate scales, $4 \lesssim k \lesssim 18$, tends. However, this inertial interval is very short. The detected exponent -2.1 is larger than the value predicted for the case of BO hydrodynamic convection $-9/5 = -1.8$ (cf. (3.11), [GL93]), but at the same time somewhat smaller than the scaling exponent predicted for passive scalar regime of hydrodynamic turbulence $-7/3 \approx -2.3$ (cf. (4.7), [GL93]). The detected slope of the inertial range is closer to the passive scalar scaling $\sim k^{-2.3}$, which would be in agreement with the total energy spectra where a Kolmogorov-like scaling is observed and not a Bolgiano-Obukhov one.

6.3 Inertial-range dynamics

6.3.1 Spectral energy transfer

To determine the direction and other spectral properties of energy and entropy cascades in the performed simulation of 3D magnetoconvection, transfer functions of individual fields are plotted in Fig. 6.6. The depicted transfer functions are defined analogously to the expression (3.12) in chapter 3. The kinetic energy transfer function $\hat{T}_k^{\mathrm{EV}}$ and the magnetic energy transfer function $\hat{T}_k^{\mathrm{EM}}$ are constructed from the nonlinear terms (6.4) and (6.7), respectively. The entropy

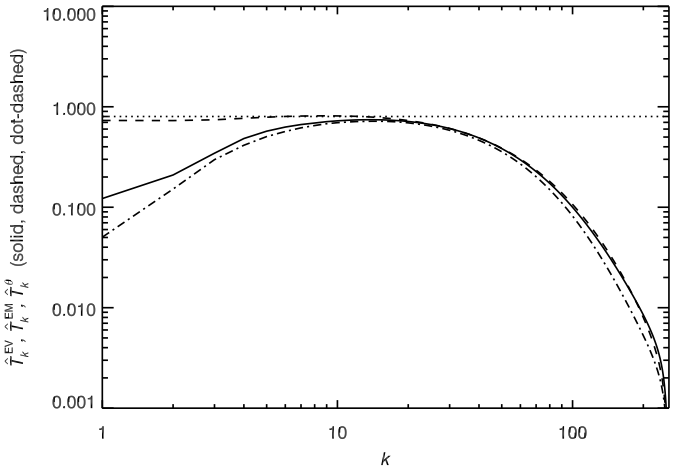

Figure 6.6: The kinetic energy transfer function $\hat{T}_k^{\mathrm{EV}}$ (solid), the magnetic energy transfer function $\hat{T}_k^{\mathrm{EM}}$ (dashed) and the entropy transfer function $\hat{T}_k^{\theta}$ (dot-dashed) in the performed simulation of 3D magnetoconvection. All transfer functions are normalized by the corresponding dissipation rates.

transfer function $\hat{T}_k^{\theta}$ has the same structure as in the previous cases (see section 3.3). All functions are normalized by the corresponding dissipation rates.

The spectrum of $\hat{T}_k^{\mathrm{EM}}$ at intermediate scales is almost horizontal approaching a constant value of 0.8. However, a part of this range that is located at very large scales, i.e. $k \lesssim 4$, is probably significantly influenced by applied boundary conditions. The spectra of $\hat{T}_k^{\mathrm{EV}}$ and $\hat{T}_k^{\theta}$ tend to the value of 0.8 as well, but only in the vicinity of the wavenumber $k \approx 14$. Thus no inertial-range transfers are observed there. However, the plot suggests that the energy at large scales is transported primarily by the magnetic nonlinear terms (6.7) while the velocity field receives energy from buoyancy, and consequently pumps it to the magnetic field. All transfer functions are positive, i.e. the energies are subject to direct cascades. The obtained spectra of the transfer functions suggest that the applied resolution 512^3 is the lower limit for a detection of inertial ranges in the 3D magnetoconvection. Additionally, a comparison of the extension of inertial ranges obtained from the energy spectra in the previous section and of that obtained from the plot of the transfer functions demonstrates a quantitative difference between both diagnostic tools.

A more detailed view of the spectral energy transport caused by the magnetic nonlinear terms can be obtained from Fig. 6.7. It shows contributions to the energy transport due to the individual terms on the r.h.s. of (6.7). The transfer functions T_k^{str} and T_k^{adv} represent the spectral energy transport by the terms (6.8) and (6.9), respectively. The transfer function T_k^{EM} is their sum, so it displays the simultaneous action of both individual terms. Both T_k^{str} and T_k^{adv} assume only positive values. Therefore, the individual nonlinear terms transfer the magnetic energy from large to small scales, i.e. by a direct cascade. However,

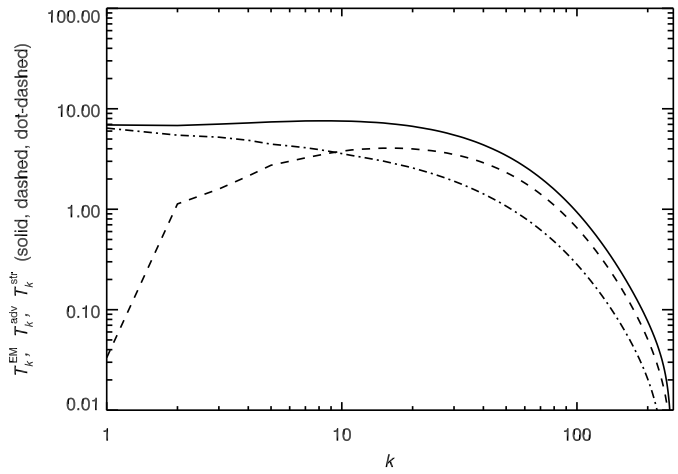

Figure 6.7: Detailed view of the spectral energy transport caused by the magnetic nonlinear terms (6.7). Transfer functions T_k^{adv} (the dashed line) and T_k^{str} (the dot-dashed line) represent contributions to the transport due to the stretching term (6.8) and the advective term (6.9), respectively. The transfer function T_k^{EM} is their sum showing a combined action of both individual terms.

T_k^{str} representing effects of the stretching term (6.8) is far more dominant at scales $k \lesssim 10$ than T_k^{adv}, indicating that primarily this term processes the energy received from the velocity field at large scales. On the contrary, T_k^{adv}, which represents effects of the advection of the magnetic field, dominates at scales $k \gtrsim 10$. Thus the energy is transported mainly by this term to the smallest scales where it is eventually dissipated by magnetic diffusivity.

6.3.2 Detailed energy exchange

An important question concerning the spectral transport of magnetic energy is whether this transport occurs locally in spectral space or not. In order to answer this question, it is necessary to understand the role of the separated terms in (6.7) participating in the transfer of magnetic energy.

The advection term $\mathbf{b}\cdot(\mathbf{v}\cdot\nabla)\mathbf{b}$ transfers the energy only between two magnetic Fourier modes with the third velocity Fourier mode being a mediator of this transfer. This follows from the fact that it is possible to recast this term in divergence form (see (6.9)), i.e. the magnetic field neither gains nor loses energy. The advection term conserves the magnetic energy irrespective of the kinetic energy dynamics. In other words, the kinetic energy of the system does not change directly due to effects of this term, i.e. there is no exchange of energy between the velocity and the magnetic field caused by this term.

The behavior of the stretching term $\mathbf{b}\cdot(\mathbf{b}\cdot\nabla)\mathbf{v}$ is more complex. Since it is a complementary term to the Lorentz force (see (6.8)), it participates in the exchange of energy between the velocity and the magnetic field. It follows

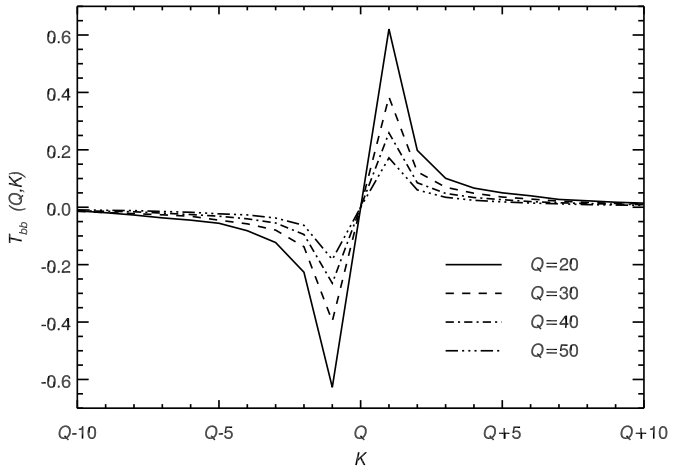

Figure 6.8: The spectral transfer of magnetic energy $T_{bb}(Q, K)$ caused by the advection term between different shells in Fourier space. The interaction between velocity and magnetic field Fourier modes in the shell Q results in the redistribution of the magnetic energy over different shells K. The spectral transport caused by the advection term is essentially direct and local.

from its structure that all three, i.e. two magnetic and one velocity, Fourier modes are active in the spectral transfer of energy. Hence this term is capable, apart from the energy exchange between both fields, to transport the magnetic energy in spectral space as well. It is verified that the change of the energy in the velocity shell K caused by the Lorentz force $\int_V \mathbf{v}_K \cdot (\mathbf{b} \cdot \nabla)\mathbf{b} dV$ does not correspond to the change of the energy in the magnetic field shell K caused by the stretching term $\int_V \mathbf{b}_K \cdot (\mathbf{b} \cdot \nabla)\mathbf{v}_K dV$, i.e. not only magnetic field Fourier modes in the shell K, but also magnetic field Fourier modes in other shells, contribute to the change of the energy in the particular velocity shell K. In other words, the stretching term does not only exchange the energy between the velocity and the magnetic field, but it changes the energy content of all magnetic field Fourier modes as well. Thus an analysis that has a clear interpretation should consider the impact of this term on the entire magnetic wavenumber range. It is important to note that the energy originating in magnetic and velocity Fourier modes in this term cannot be distinguished, i.e. they are from the point of view of the nonlinear MHD interactions equivalent. Therefore, several published results ([AMP05][MAP05]) demonstrating a possible nonlocal spectral transfer of magnetic energy might be misleading. The overall impact of the stretching term in the performed simulation of 3D magnetoconvective turbulence was shown in Fig. 6.7 that displays the transfer function T_k^{str}.

The spectral transfer of magnetic energy between different wavenumber shells Q and K that is caused by the advection term (6.9) is plotted in Fig. 6.8. The spectral transport is evaluated as (see section 3.3.2)

$$T_{bb}(Q, K) \equiv \int -\mathbf{b}_K (\mathbf{v} \cdot \nabla)\mathbf{b}_Q dV. \tag{6.11}$$

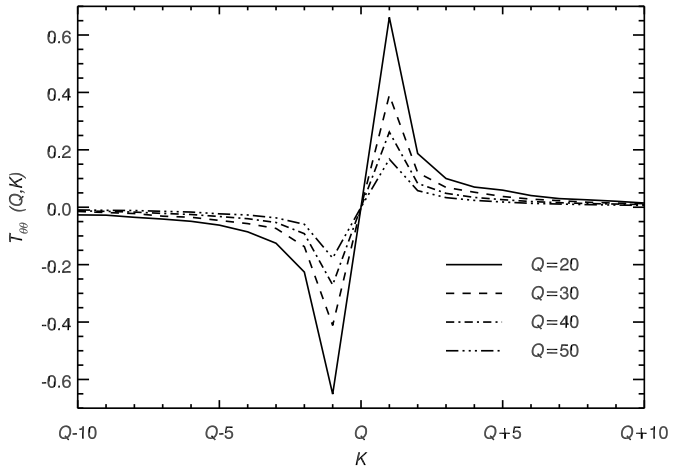

Figure 6.9: The spectral transfer of entropy $T_{\theta\theta}(Q, K)$ between different shells in Fourier space obtained from the performed simulation of 3D magnetoconvective turbulence. The spectral transport of entropy is essentially direct and local.

The incidental shells $Q = 20, 30, 40, 50$ are chosen close to inertial-range scales $7 \lesssim k \lesssim 20$. The picture suggests a direct cascade where the magnetic energy is predominantly transferred from the immediately preceding wavenumber shell $K = Q - 1$ to the consecutive shell $K = Q + 1$. The energy transfer to the shells $K < Q - 10$ and $K > Q + 10$ is negligibly small. Hence this plot confirms that the spectral transfer of magnetic energy due to the advection term is essentially direct and local.

The result of the same analysis of the spectral transport of entropy is shown in Fig. 6.9. It displays a qualitatively same behavior as the previous graph. Hence all main characteristic features of the spectral transfer of entropy are the same as in the previous case, i.e. the transfer is essentially direct and local.

Both analyses of spectral transfer indicate that advection terms generally transport a particular energy locally in spectral space from large to small scales.

6.4 Statistical results

On one hand, (one-dimensional) structure functions exhibit usually a somewhat shorter extension of the inertial interval compared to angle-integrated energy spectra because they use less data points than the angle-integrated spectra. On the other hand, it is well tested that spurious oscillations and statistical noise in inertial intervals of structure functions are largely suppressed when extended self-similarity is used (e.g. [Bis03][CH06]). Thus relative scaling exponents of structure functions can be better determined. In the previous chapters, ESS applied to the individual fields has been already verified to hold also in the case of turbulent convection.

6.4.1 Structure functions

Structure functions computed from the performed simulation of 3D magnetoconvective turbulence are depicted in Fig. 6.10. The left column displays structure functions $S_p^+(l) = \langle(\delta z^+)^p\rangle$ of the Elsässer variable z^+ (see section 5.2) of the order $p = 2, 3, 4$ (from top to bottom). The structure function $S_2^+(l)$ is a real space counterpart of the total energy spectrum, if the level of alignment between the velocity and the magnetic field in the system is small, $S_2^+ \sim l^\alpha \leftrightarrow E_k^{\rm tot} \sim k^{-\alpha-1}$. The right column shows structure functions $S_p^\theta(l)$ of the temperature field ordered analogously. Both $S_p^+(l)$ and $S_p^\theta(l)$ are normalized by the corresponding powers of energies, $(E^{+,\,\theta})^{p/2}$. In order to avoid cancellation effects in calculations of structure functions of odd order, these functions are evaluated from absolute values of field increments. Inserts in the figures show logarithmic derivatives of the structure functions in order to reveal their slope at inertial-range scales. Horizontal dashed lines indicate estimated values of scaling exponents $\zeta_p^{+,\,\theta}$.

The curves of the second order structure functions $S_2^+(l)$ and $S_2^\theta(l)$ do not show any clear self-similar interval. The large-scale part almost continuously merges with the dissipation range. In addition, the logarithmic derivatives display very smooth monotonously decreasing profiles with no easily detectable plateaux. The scaling exponent of $S_2^+(l)$ is therefore determined with a relatively large error, $\zeta_2^+ = 0.57 \pm 0.07$. For the better readability, the horizontal dashed line indicating a scaling exponent of ζ_2^θ is omitted in the plot of the logarithmic derivative of $S_2^\theta(l)$. However, the scaling exponent of ζ_2^θ is determined as $\zeta_2^\theta = 0.51 \pm 0.06$. This exponent is in approximate agreement with the exponent of the entropy spectra in Fig. 6.1.

The situation is slightly different for higher orders of the structure functions. In the case of $S_3^+(l)$ and $S_4^+(l)$ the plateau in the profile of the logarithmic derivatives is more pronounced compared to the logarithmic derivative of $S_2^+(l)$ leading to estimates of scaling exponents of inertial intervals $\zeta_3^+ = 0.77 \pm 0.04$ and $\zeta_4^+ = 0.91 \pm 0.03$. The temperature field structure functions of the third and the fourth order and their logarithmic derivatives suggest $\zeta_3^\theta = 0.62 \pm 0.03$ and $\zeta_4^\theta = 0.71 \pm 0.02$.

Structure functions of the Elsässer field z^- differ only negligibly from that of z^+ since the system exhibits only an insignificant level of alignment, and are therefore not shown here.

6.4.2 Probability density functions

Probability density functions (pdfs) p^+ of the z^+ field increments and the pdf p^θ of the temperature field increments are depicted on the l.h.s. and on the r.h.s of Fig. 6.11, respectively. The top and bottom pictures show pdfs taken at large ($l \approx L$) and small ($l \approx 10^{-2}L$) scales, respectively. In all figures the dashed line corresponds to a Gaussian pdf with the same variance. The curve of p^+ at large scales does not coincide with the Gaussian pdf exactly showing a significant departure in the tails. In contrast to that the pdf of temperature fluctuations, p^θ, is at large scales almost perfectly Gaussian. The observed departure of the

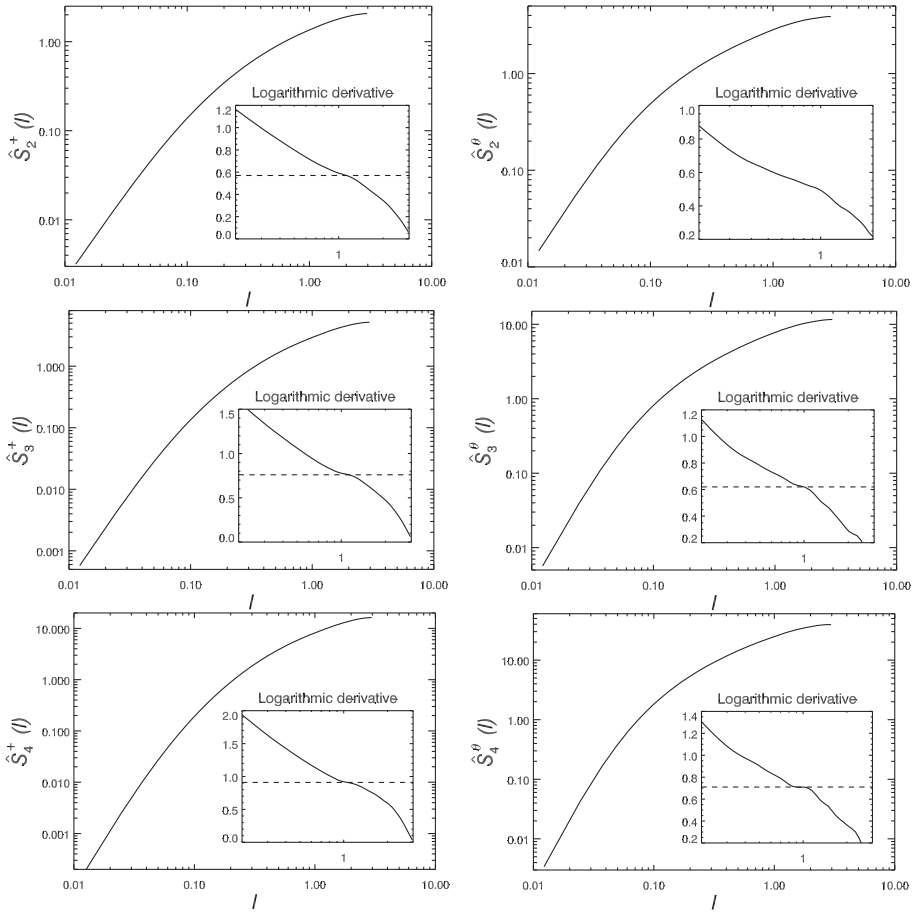

Figure 6.10: Structure functions $S_p^+(l)$ of the Elsässer variable z^+ (left) and temperature structure functions $S_p^\theta(l)$ (right) of the order $p = 2, 3, 4$ (from top to bottom) in the performed simulation of 3D magnetoconvective turbulence. The structure functions are normalized by the corresponding powers of energies, $(E^{+,\,\theta})^{p/2}$. Inserts show logarithmic derivatives of the structure functions. Dashed lines indicate the estimated values of scaling exponents $\zeta_p^{+,\,\theta}$.

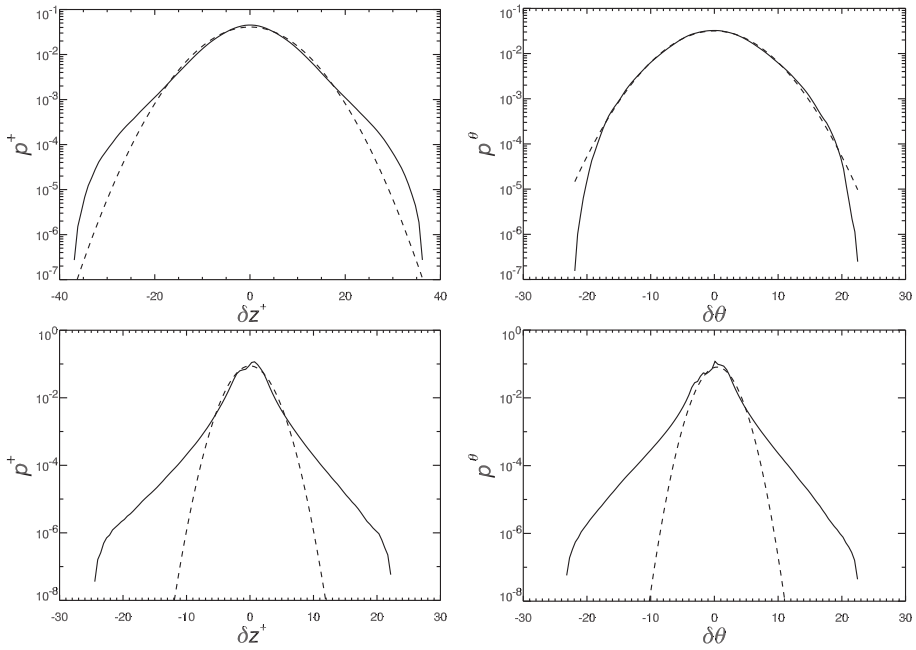

Figure 6.11: Probability density functions p^+ (left) and p^θ (right) at large ($l \approx L$) and small ($l \approx 10^{-2}L$) scales (top and bottom) obtained from the performed simulation of 3D magnetoconvective turbulence. Dashed lines denote the corresponding Gaussian pdfs with the same variance.

tails of p^+ is probably caused by the averaging procedure since the analyzed system is evolved for approximately 4 typical buoyancy times, and is therefore not perfectly relaxed at the largest scales, i.e. a decorrelation time is longer than the buoyancy time at the temperature gradient scale L. The small-scale pdfs display the presence of non-Gaussian wings. These imply intermittency effects in the investigated system, i.e. corrections to ideal scaling. The wings of p^θ are more pronounced than that of p^+, but this feature needs to be quantitatively better specified.

A useful tool for that is the evaluation of the flatness parameter F of the probability density functions as a function of spatial scale l (see (3.25)). The result of this calculation is shown in Fig. 6.12. Both $F^+(l)$ and $F^\theta(l)$ at large scales tend approximately to the Gaussian value $F = 3$. The behavior of F^+ and F^θ at small scales confirms that dissipative structures of the temperature field are in real space more intermittent than dissipative structures of the velocity and the magnetic field. The flatness F^θ assumes at small scales values around 16 while F^+ assumes values around 12. The temperature field is less intermittent than in the pure hydrodynamic case studied in chapter 4 ($F^\theta \approx 26$, see Fig. 4.10). The level of a small-scale intermittency of z^+ is similar to that of the velocity field in the simulation of 3D hydrodynamic convection ($F^v \approx 12$, see Fig. 4.10).

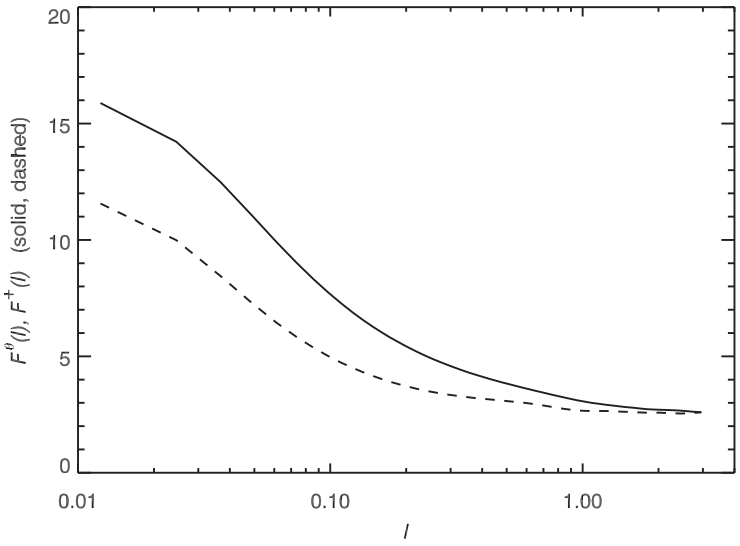

Figure 6.12: The flatness $F^+(l)$ and $F^\theta(l)$ of probability density functions p^+ and p^θ, respectively, as a function of l in the performed simulation of 3D magnetoconvective turbulence.

Order p	ζ_p^+/ζ_2^+	$\zeta_p^\theta/\zeta_2^\theta$
2	1	1
3	1.33 ± 0.06	1.25 ± 0.09
4	1.60 ± 0.08	1.42 ± 0.11
5	1.85 ± 0.10	1.52 ± 0.13
6	2.10 ± 0.13	
7	2.35 ± 0.15	

Table 6.1: Relative scaling exponents of temperature and z^+ structure functions calculated from the simulation of 3D magnetoconvective turbulence. The exponents ζ_p^+/ζ_2^+ up to the order $p = 7$ as well as the exponents $\zeta_p^\theta/\zeta_2^\theta$ up to the order $p = 5$ are obtained via ESS.

6.4.3 Intermittency models

In order to investigate intermittency effects in 3D magnetoconvective turbulence, relative scaling exponents of higher order structure functions are calculated. The obtained values are summarized in Tab. 6.1. The relative scaling exponents $\zeta_p^\theta/\zeta_2^\theta$ are determined only up to the order $p = 5$ due to the increasing level of statistical noise. Beyond this order fitting uncertainties are too large.

Fig. 6.13 shows the graph of the relative scaling exponents ζ_p^+/ζ_2^+ of the z^+ field. The computed values are denoted by diamonds. Triangles stand for numerical results of 3D MHD turbulence ([MB00], $\mathsf{Re_m} \approx 3000$, $\mathsf{Pr_m} = 1$). The dashed line corresponds to the nonintermittent Kolmogorov scaling $l^{p/3}$. The dotted line and the dot-dashed line denote the Iroshnikov–Kraichnan She-Lévêque model and the modified She-Lévêque model, respectively.

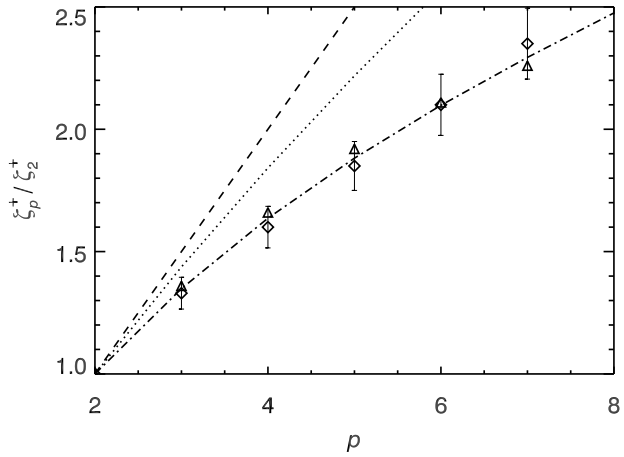

Figure 6.13: Relative scaling exponents ζ_p^+/ζ_2^+ (diamonds) of the z^+ structure functions in the simulation of 3D magnetoconvective turbulence computed up to the seventh order as a function of order p. The dashed line corresponds to the nonintermittent Kolmogorov scaling $l^{p/3}$. The dot-dashed line is the prediction according to the modified She-Lévêque model (6.13). The dotted line is the prediction of the IK-She-Lévêque model (6.14). Triangles denote numerical values obtained from simulations of 3D MHD turbulence ([MB00]).

The two latter models are based on the phenomenological log-Poison model proposed by She and Lévêque ([SL94]) which has the general form

$$\zeta_p^{\mathrm{SL}} = \frac{p}{g}\left(1-\frac{2}{g}\right) + C_0\left[1-\left(1-\frac{2}{gC_0}\right)^{p/g}\right] \tag{6.12}$$

where C_0 is a codimension of the most intermittent structures, and g is determined from the underlying nonintermittent scaling law, $l^{1/g}$. In MHD turbulence the relation (6.12) under the assumption of the Kolmogorov scaling $l^{p/3}$ and $C_0 = 1$ which corresponds to dissipative structures in a form of two-dimensional sheets (e.g. [MB00]) leads to the modified She-Lévêque model

$$\zeta_p^{\mathrm{MHD}} = \frac{p}{9} + 1 - \left(\frac{1}{3}\right)^{p/3}. \tag{6.13}$$

If instead of the Kolmogorov scaling $l^{p/3}$ the nonintermittent Iroshnikov-Kraichnan scaling $l^{p/4}$ is assumed, the generalized She-Lévêque model (6.12) yields (e.g. [MB00])

$$\zeta_p^{\mathrm{IK}} = \frac{p}{8} + 1 - \left(\frac{1}{2}\right)^{p/4}. \tag{6.14}$$

The relative scaling exponents ζ_p^+/ζ_2^+ of the z^+ structure functions shown in the plot deviate from the nonintermittent Kolmogorov scaling $l^{p/3}$ significantly. On

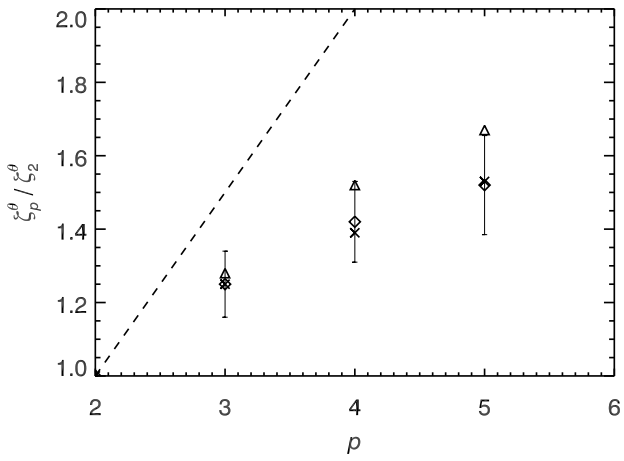

Figure 6.14: Relative scaling exponents $\zeta_p^\theta/\zeta_2^\theta$ (diamonds) of the temperature structure functions in the simulation of 3D magnetoconvective turbulence up to the fifth order as a function of order p. The dashed line corresponds to the non-intermittent scaling $l^{p/3}$. Triangles denote temperature fluctuations measurements in wind tunnel turbulence ([RBC96]). Crosses stand for the numerical results of 3D passive scalar hydrodynamic convection obtained in chapter 4.

the contrary, the exponents coincide surprisingly well with the values obtained from numerical simulations of 3D MHD turbulence ([MB00]). Both numerical results are well approximated by the modified She-Lévêque formula (6.13) leading to the conclusion that the simulated system operates in the Kolmogorov regime of MHD turbulence. This fact is supported by the relatively small nominal Rayleigh number achieved in the performed simulation, $\mathsf{Ra} \approx 4.5 \cdot 10^5$. This value corresponds to the Bolgiano length that is about one order larger than the largest resolved scale in the simulation. Thus temperature fluctuations in the investigated system play the role of a passive scalar. Comparing the fact that the intermittency of the z^+ field which follows the She-Lévêque prediction (6.13) is based on the Kolmogorov scaling $l^{p/3}$ with the computed energy spectra (Fig. 6.1), it seems plausible that the system operates in the Kolmogorov regime and not in the Iroshnikov-Kraichnan regime of MHD turbulence. However, due to the lack of sufficient resolution it is not possible to verify this conclusion directly.

The level of intermittency of the temperature field is shown in Fig. 6.14. It displays values of the relative scaling exponents $\zeta_p^\theta/\zeta_2^\theta$ evaluated via ESS. The computed values are denoted by diamonds. The dashed line corresponds to the nonintermittent scaling of passive scalars $l^{p/3}$ (cf. (1.31)). Triangles stand for results of passive temperature fluctuations in a wind tunnel turbulence ([RBC96], $\mathsf{Re} \approx 4.5 \cdot 10^5$, $\mathsf{Pr} \approx 1$). Crosses denote the result of 3D passive scalar hydrodynamic turbulent convection from chapter 4 ($\mathsf{Ra} \approx 2 \cdot 10^7$, $\mathsf{Re} \approx 2 \cdot 10^3$). The temperature field exhibits a more intermittent character than the z^+ field. The computed values of the relative exponents $\zeta_p^\theta/\zeta_2^\theta$ are in very good agreement

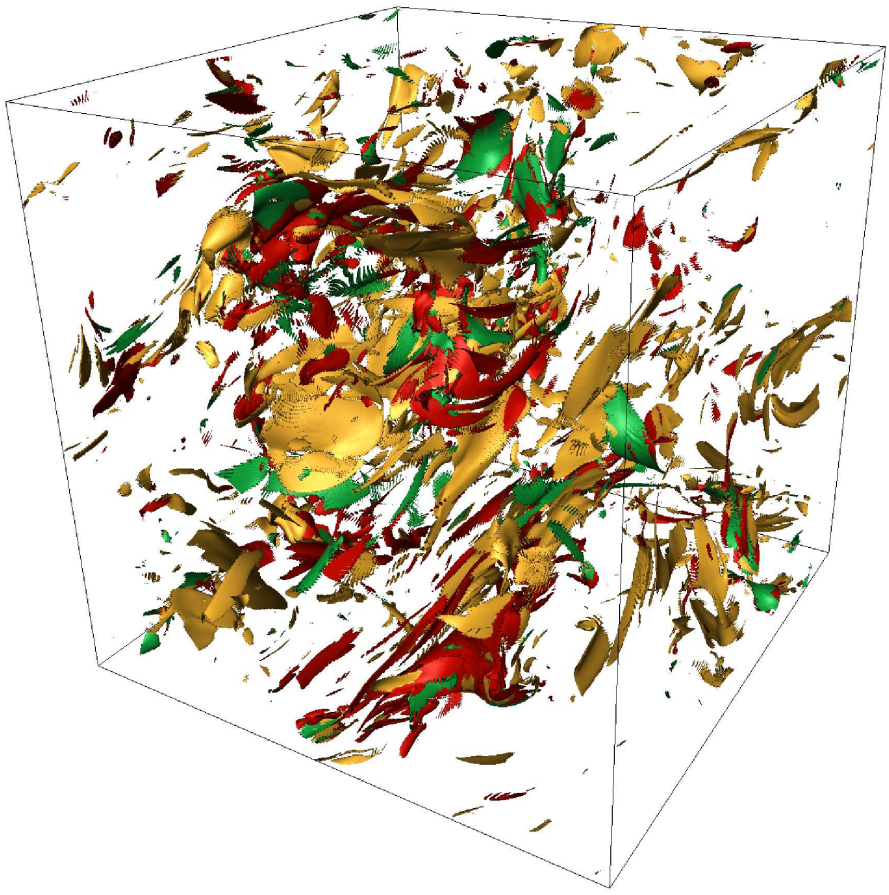

Figure 6.15: Dissipative structures represented by isosurfaces obtained from the performed simulation of 3D magnetoconvective turbulence. Different dissipations are labeled by color: vorticity – yellow, current density – green, temperature gradient – red.

with the passive scalar intermittency of the 3D hydrodynamic convection. Furthermore, the values do not differ much from the experimental measurements of a passive scalar in the wind tunnel turbulence. The passive character of the temperature field in the performed simulation of 3D magnetoconvective turbulence is therefore supported.

6.5 Visualization of fields

In order to obtain an impression of the real space configuration of the flow, several pictures showing the spatial structure of different important physical quantities are presented in this section. Fig. 6.15 displays various dissipative structures. These are represented by isosurfaces, and labeled by color: the dissipation of the kinetic energy – vorticity (yellow), of the magnetic energy –

current density (green), of the entropy – temperature gradient (red). All dissipative structures take the form of quasi-two-dimensional sheets. This is in agreement with the codimension $C_0 =$ (dimension of the system) $-$ (dimension of the most intermittent structures) $= 3-2 = 1$ suggested for the modified She-Lévêque model (6.13) in the previous section. The quasi-two-dimensional sheets occur locally close to each other, e.g. in the lower right corner. This configuration is caused by the fact that all three energies are predominantly dissipated at places of large gradients of the individual fields. These large gradients are localized at transitions between regions of significantly different temperatures, i.e. coherent parts of the fluid. On the contrary, inner parts of this regions are quite smooth, and exhibit only small variations of the fields.

This interpretation is confirmed by Fig. 6.16 that displays the velocity field, the magnetic field and the temperature field (l.h.s., from top to bottom) together with the corresponding dissipations (r.h.s., from top to bottom) in a horizontal slice through the system. The velocity field and the magnetic field, both projected onto the horizontal slice, are represented by lines. The magnitude of the fields is denoted by color (light – high values, dark – low values). The plots on the r.h.s. show structures of associated dissipations ω^2, j^2 and $(\nabla\theta)^2$. Indeed, two large regions of significantly different temperatures in the center of the horizontal cross-section can be identified, separated by a very narrow transition region where the dissipation of all three fields is largely amplified. Especially, the hot region can be well recognized in the lower right picture showing the magnitude of the temperature energy dissipation which is amplified on the boundary of this region. The dissipation of the kinetic and the magnetic energy exhibits a similar structure as well.

Fig. 6.17 displays the global structure of the magnetic field represented by three perpendicular slices. The magnitude of the magnetic field is denoted by color (red – high values, blue – low values). The system exhibits more elongated structures in the vertical direction than in horizontal directions. They correspond to rising and sinking blobs of the fluid of different temperature with their horizontal movements constrained by the magnetic field. Several magnetic field lines are depicted in the center of the plot indicating the spatial configuration of the magnetic field.

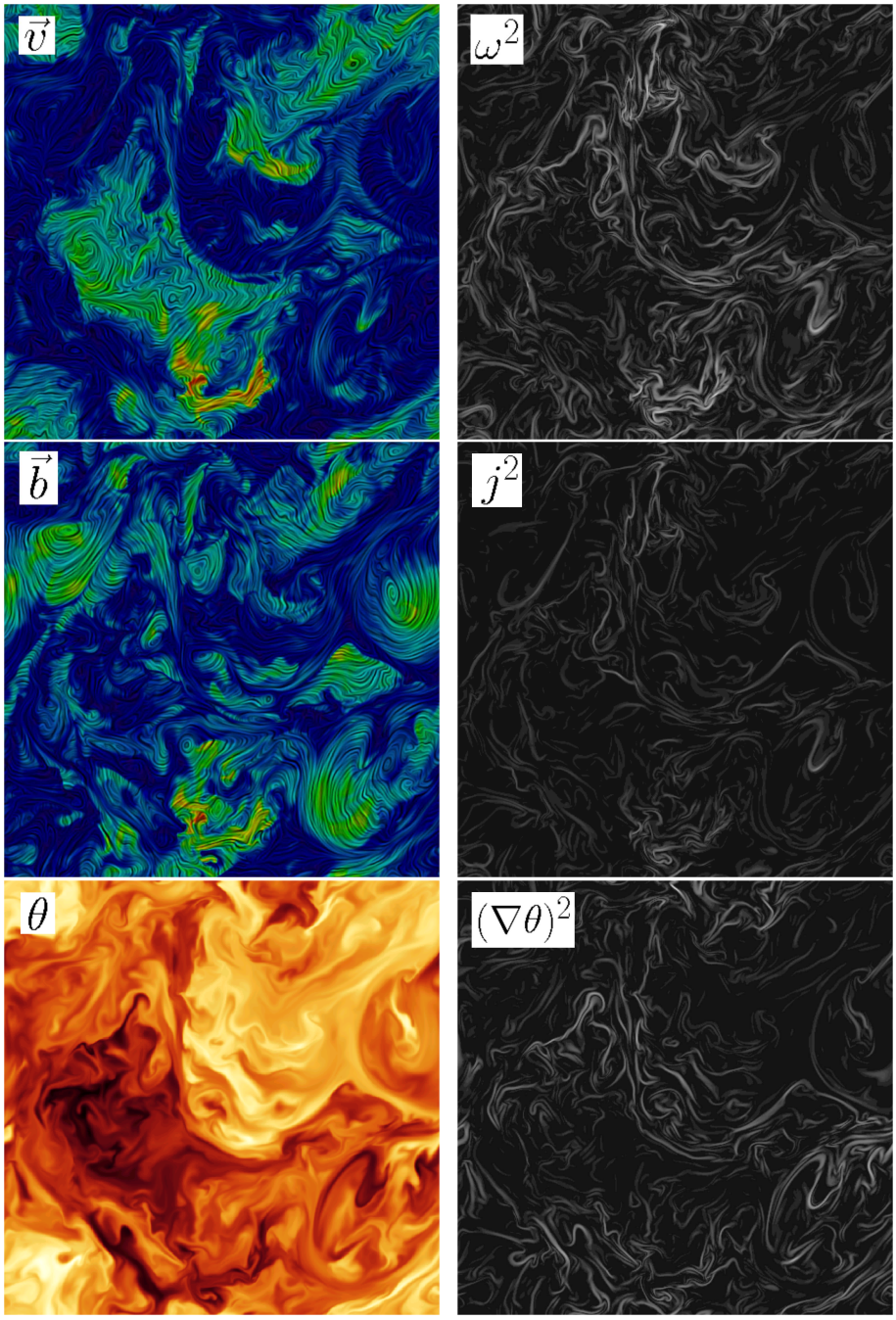

Figure 6.16: Left: Structure of the velocity field, the magnetic field and the temperature field (from top to bottom) in the horizontal slice through the 3D magnetoconvective system. Vector fields are represented by lines. Magnitudes are denoted by color (light – high values, dark – low values). Right: Structure of the vorticity, the current density and the temperature gradient (from top to bottom) in the same slice.

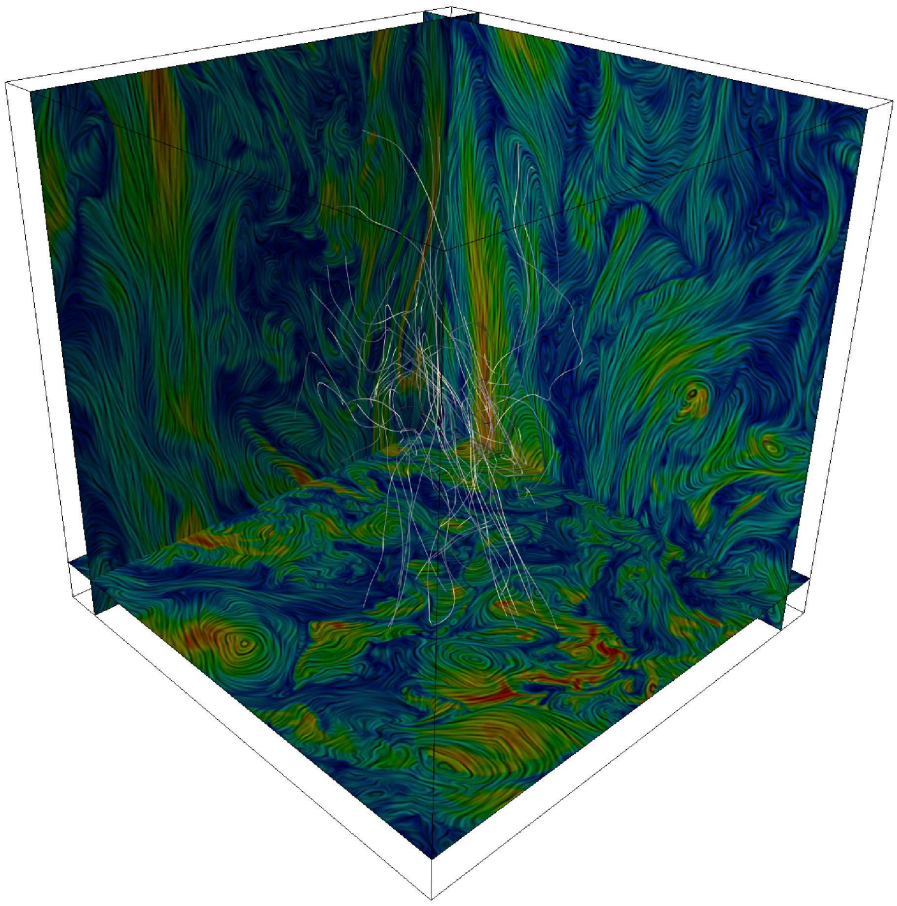

Figure 6.17: Global structure of the magnetic field represented by three perpendicular slices in the performed simulation of 3D magnetoconvective turbulence. The magnitude of the field is denoted by color (red – high values, blue – low values). Magnetic field structures are more elongated in the vertical direction than in horizontal directions. Several magnetic field lines are depicted in the center of the figure.

Conclusions

This thesis presents extensive numerical studies of turbulent convection. Within the frame of the thesis, turbulent convection is investigated by means of several large-scale direct numerical simulations. The main advantage of the numerical approach is the possibility of comprehensive diagnostics since calculated turbulent fields are known at all grid points of a computational box at all time steps. A similarly detailed diagnostics is inaccessible in experimental studies. The main disadvantage is that the computational power of present-day supercomputers limits maximal values of physical parameters, e.g. the Rayleigh number, in numerical simulations to moderate levels compared to laboratory experiments. Four particular systems are analyzed in the work, namely: two- and three-dimensional hydrodynamic and magnetohydrodynamic (MHD) turbulent convection. Due to capabilities of the supercomputer facility of the Rechenzentrum Garching at the Max-Planck-Institute for Plasma Physics, convective systems are simulated for the first time with very high resolutions, e.g. the 3D hydrodynamic convection (1024^3, $\mathsf{Ra} \approx 2 \cdot 10^7$) or the 3D magnetoconvection (512^3, $\mathsf{Ra} \approx 4.5 \cdot 10^5$). Such resolutions are necessary in order to resolve an inertial range of a turbulent flow, and allow for a direct comparison between different phenomenological theories of turbulence.

All four convective systems are investigated using a pseudospectral code previously developed for studies of MHD turbulence that is extended to account for Boussinesq convection. The modified version of the code is tested by employing a Rayleigh-Bénard setup with closed vertical boundaries. The results of the performed tests are in good agreement with available theoretical and numerical predictions. Furthermore, the code is optimized for use on massively parallel supercomputers. Its very good scalability and performance are confirmed using up to 512 processors.

Since one of the main interests of this work is to analyze statistical properties of turbulent convection, the closed vertical boundaries are after the tests replaced by fully periodic geometry. Such a numerical setup excludes effects caused by specific boundaries, so the approximate statistical homogeneity of a system is preserved. This setup is therefore suitable for statistical analysis. All investigated convective systems are driven by a horizontal temperature gradient because it ensures stability of the fully periodic configuration which is shown by linear analysis.

At first hydrodynamic turbulent convection in two dimensions is considered. Such a system with a mean temperature gradient in the vertical direction has

been previously analyzed by several authors, and therefore the influence of the mean temperature gradient that is in the horizontal direction can be examined. However, no qualitative difference of statistical properties of the turbulent dynamics is found. The nonlinear dynamics is largely affected by buoyancy forces, so the temperature field plays a role of an active scalar. This is in agreement with the calculated energy spectra which follow predictions of the Bolgiano-Obukhov phenomenology. One of the basic assumptions of this phenomenology, a local transfer of entropy in spectral space, is verified for the first time. Moreover, the statistics of velocity increments at small scales suggest that the velocity field is slightly intermittent, similarly as it is observed in studies of two-dimensional hydrodynamic turbulence. This intermittency is well described by a log-Poisson model that is known from investigations of intermittency in fully developed hydrodynamic turbulence. At dissipation scales the temperature field exhibits ramp-and-cliff structures typical for passive scalar turbulence.

The next step to better understand convective turbulence in real observable systems is to consider three-dimensional hydrodynamic convection. This configuration is of a special interest since experimental and numerical studies favor different phenomenologies of turbulent convection, namely the ones by Bolgiano-Obukhov and Kolmogorov. The analyzed three-dimensional system is found to operate in the Kolmogorov regime known from studies of isotropic hydrodynamic turbulence. This fact is in agreement with a relatively low Rayleigh number achieved due to limited computational resources, $\mathsf{Ra} \approx 2 \cdot 10^7$, compared to laboratory experiments with Ra up to 10^{17}. The temperature field drives velocity fluctuations at the largest scales, but it does not affect the nonlinear dynamics at inertial-range scales where the temperature is passively advected by the velocity.

Probably the simplest model that involves the effects of magnetic fields on turbulent convection is magnetoconvective turbulence in two dimensions. This configuration is particularly attractive because it allows to apply higher Rayleigh and Reynolds numbers than in the three-dimensional case. Moreover, plasma dynamics in two dimensions can be seen as an approximation to fully three-dimensional systems with strong mean magnetic fields where the turbulent dynamics is largely restricted to two-dimensional planes perpendicular to the mean field. For such systems the results of the study of this configuration are particularly relevant. The investigated two-dimensional magnetoconvective turbulence is found to exhibit a new feature, namely quasi-oscillations between the Iroshnikov-Kraichnan regime of turbulence where buoyancy influences the nonlinear dynamics negligibly and the buoyancy dominated regime of turbulence. The different character of the flow in the individual regimes results in differences of the observed energy spectra. A new phenomenological model of the quasi-oscillations is proposed that is based on cross-helicity dynamics and on the effect of dynamical alignment known from decaying 3D MHD turbulence.

Since the turbulent convection examined in the previous chapters shows a different behavior in different setups, it is very interesting to analyze also fully three-dimensional magnetoconvection, especially with respect to the quasi-oscillations observed in the two-dimensional case. However, no such quasi-oscillations are found. This fact can be caused by several reasons, for instance: a) the nonlinear dynamics underlying MHD turbulence is still not fully understood and can be

different in 3D and 2D, b) it is difficult to achieve a sufficient alignment between velocity and magnetic field in three dimensions because of more degrees of freedom compared to the 2D case. The computed energy spectra indicate that the investigated system is strongly anisotropic, and operates in a Kolmogorov-like regime of MHD turbulence. This fact is given by numerical constraints since in the performed simulation only moderate values of Rayleigh and Reynolds numbers are achieved. By analyzing the spectral flux of magnetic energy and entropy, it is verified that both quantities are transferred predominantly locally in spectral space. The statistics of spatial increments of Elsässer fields suggest that these fields are intermittent at small scales. The calculated level of intermittency is in good agreement with the modified She-Lévêque model that successfully describes also the intermittency of isotropic MHD turbulence.

In the presented work, several others more specific issues are addressed:

- All nonlinear terms analyzed in the work transport energy predominantly locally in spectral space. No nonlocal transport of energy between far-distant Fourier modes in spectral space is detected. The validity of the assumption of local transfer of energy is supported.
- The horizontal orientation of a mean temperature gradient does not affect the nonlinear dynamics of turbulent convection significantly in the sense that the Bolgiano-Obukhov picture remains unaffected. The gradient provides energy for velocity fluctuations predominantly at the largest scales.
- The hypothesis about an extension of the Bolgiano-Obukhov scaling over all scales in turbulent convection with a horizontal mean temperature gradient ([LF92]) is not confirmed.
- A large impact of magnetic fields on the nonlinear dynamics of convection is observed, especially in two dimensions.
- Regarding scaling contradictions between laboratory and numerical results in 3D hydrodynamic convection, it seems that the presence of the inverse cascade of kinetic energy is not crucial for turbulent convection to operate in the Bolgiano-Obukhov regime of turbulence. Indeed, the buoyancy dominated regime is detected also in the investigated 2D magnetoconvective turbulence where due to the action of the Lorentz force the energy is transferred from large to small scales. Furthermore, there is no evident reason why the buoyancy term could not dominate the nonlinear dynamics at very high Rayleigh numbers, irrespective of the orientation of the kinetic energy cascade and the dimension of the system. However, an additional computational effort is required to clarify this issue directly.

From all four configurations of turbulent convection investigated in the presented work, two-dimensional magnetoconvective turbulence turns out to be the most interesting. This system is particularly attractive since it exhibits quasi-oscillations between two turbulent regimes, so it represents a useful model for a detailed study of the interplay between buoyancy and nonlinear forces in convective turbulence. Additionally, the investigation of three-dimensional hydrodynamic convection is very important since this configuration can be analyzed not only by numerical simulations but in laboratory experiments as well.

Consequently, the results can be directly compared. Therefore, further investigations especially of two-dimensional magnetoconvection and three-dimensional hydrodynamic convection are the most promising for the improvement of our understanding of turbulent convection.

Bibliography

[AMP05] A. Alexakis, P. D. Mininni, and A. Pouquet. Shell-to-shell energy transfer in magnetohydrodynamics. I. Steady state turbulence. *Phys. Rev. E*, 72:046301, 2005.

[Ben01] H. Bénard. The cellular whirlpools in a liquid sheet transporting heat by convection in a permanent regime. *Ann. Chim. Phys.*, 23:62–101, 1901.

[BHS01] D. Biskamp, K. Hallatschek, and E. Schwarz. Scaling laws in two-dimensional turbulent convection. *Phys. Rev. E*, 63:045302, 2001.

[Bis97] D. Biskamp. *Nonlinear Magnetohydrodynamics*. Cambridge University Press, Cambridge, UK, 1997.

[Bis03] D. Biskamp. *Magnetohydrodynamic turbulence*. Cambridge University Press, Cambridge, UK, 2003.

[BKM05] S. D. Bale, P. J. Kellogg, F. S. Mozer, T. S. Horbury, and H. Reme. Measurement of the electric fluctuation spectrum of magnetohydrodynamic turbulence. *Phys. Rev. Lett.*, 94:215002, 2005.

[BM00] D. Biskamp and W.-C. Müller. Scaling properties of three-dimensional isotropic magnetohydrodynamic turbulence. *Phys. Plasmas*, 7:4889–4900, 2000.

[Bol59] R. Bolgiano. Turbulent spectra in a stably stratified atmosphere. *J. Geophys. Res.*, 64:2226–2229, 1959.

[Bol06] S. Boldyrev. Spectrum of magnetohydrodynamic turbulence. *Phys. Rev. Lett.*, 96:115002, 2006.

[Bra92] A. Brandenburg. Energy spectra in a model for convective turbulence. *Phys. Rev. Lett.*, 69:605–608, 1992.

[Bri74] E. O. Brigham. *The fast Fourier transform*. Prentice-Hall, Inc., Englewood Cliffs, US, 1974.

[BS01] D. Biskamp and E. Schwarz. On two-dimensional magnetohydrodynamic turbulence. *Phys. Plasmas*, 8:3282–3292, 2001.

[BSC98] D. Biskamp, E. Schwarz, and A. Celani. Nonlocal Bottleneck Effect in Two-Dimensional Turbulence. *Phys. Rev. Lett.*, 81:4855–4858, 1998.

[BTT98] R. Benzi, F. Toschi, and R. Tripiccione. On the Heat Transfer in Rayleigh-Bénard Systems. *J. Stat. Phys.*, 93:901–918, 1998.

[BW89] D. Biskamp and H. Welter. Dynamics of decaying two-dimensional magnetohydrodynamic turbulence. *Phys. Fluids B*, 1:1964–1979, 1989.

[CCI93] F. Chillá, S. Ciliberto, C. Innocenti, and E. Pampaloni. Boundary-layer and scaling properties in turbulent thermal-convection. *Nuovo Cimento D*, 15:1229–1249, 1993.

[CCM04] A. Celani, M. Cencini, A. Mazzino, and M. Vergassola. Active and passive fields face to face. *New J. Phys.*, 6:72, 2004.

[CH06] S. C. Chapman and B. Hnat. Kolmogorov and irosnikov-kraichnan scaling in the anisotropic turbulent solar wind. *ArXiv e-prints*, physics/0606106, 2006.

[Cha61] S. Chandrasekhar. *Hydrodynamic and hydromagnetic stability.* Clarendon Press, Oxford, US, 1961.

[Che03] M. Chertkov. Phenomenology of Rayleigh-Taylor Turbulence. *Phys. Rev. Lett.*, 91:115001, 2003.

[CHQ88] C. Canuto, M. Y. Hussaini, A. Quarteroni, and T. A. Zang. *Spectral methods in fluid dynamics.* Springer-Verlag, New York, US, 1988.

[CK98] S. Chen and R. H. Kraichnan. Simulations of a randomly advected passive scalar field. *Phys. Fluids*, 10:2867–2884, 1998.

[CLM00] A. Celani, A. Lanotte, A. Mazzino, and M. Vergassola. Universality and saturation of intermittency in passive scalar turbulence. *Phys. Rev. Lett.*, 84:2385–2388, 2000.

[CLT05] E. Calzavarini, D. Lohse, F. Toschi, and R. Tripiccione. Rayleigh and Prandtl number scaling in the bulk of Rayleigh-Bénard turbulence. *Phys. Fluids*, 17:5107, 2005.

[CMM02] A. Celani, T. Matsumoto, A. Mazzino, and M. Vergassola. Scaling and universality in turbulent convection. *Phys. Rev. Lett.*, 88:054503, 2002.

[CMV01] A. Celani, A. Mazzino, and M. Vergassola. Thermal plume turbulence. *Phys. Fluids*, 13:2133–2135, 2001.

[Cow55] T. G. Cowling. Dynamo theories of cosmic magnetic fields. *Vistas Astr.*, 1:313–322, 1955.

[CTT02] E. Calzavarini, F. Toschi, and R. Tripiccione. Evidences of Bolgiano-Obhukhov scaling in three-dimensional Rayleigh-Bénard convection. *Phys. Rev. E*, 66:016304, 2002.

[DR81] P. G. Drazin and W. H. Reid. *Hydrodynamic Stability.* Cambridge University Press, Cambridge, UK, 1981.

[Dub94] B. Dubrulle. Intermittency in fully developed turbulence: Log-Poisson statistics and generalized scale covariance. *Phys. Rev. Lett.*, 73:959–962, 1994.

[DVE01] G. Dar, M. K. Verma, and V. Eswaran. Energy transfer in two-dimensional magnetohydrodynamic turbulence: formalism and numerical results. *Phys. D*, 157:207–225, 2001.

[Els50] W. M. Elsässer. The hydromagnetic equations. *Phys. Rev.*, 79:183–183, 1950.

[FFT] http://www.fftw.org/.

[Fri95] U. Frisch. *Turbulence. The legacy of A.N. Kolmogorov*. Cambridge University Press, Cambridge, UK, 1995.

[GFP82] R. Grappin, U. Frisch, A. Pouquet, and J. Leorat. Alfvénic fluctuations as asymptotic states of MHD turbulence. *Astron. Astrophys.*, 105:6–14, 1982.

[GHM06] J. P. Graham, D. D. Holm, P. Mininni, and A. Pouquet. Inertial range scaling, Kármán-Howarth theorem, and intermittency for forced and decaying Langrangian averaged magnetohydrodynamic equations in two dimensions. *Phys. Fluids*, 18:045106, 2006.

[GL91] S. Grossmann and D. Lohse. Fourier-Weierstrass mode analysis for thermally driven turbulence. *Phys. Rev. Lett.*, 67:445–448, 1991.

[GL92] S. Grossmann and D. Lohse. Scaling in hard turbulent Rayleigh-Bénard flow. *Phys. Rev. A*, 46:903–917, 1992.

[GL93] S. Grossmann and V. S. L'vov. Crossover of spectral scaling in thermal turbulence. *Phys. Rev. Lett.*, 47:4161–4168, 1993.

[GLP83] R. Grappin, J. Leorat, and A. Pouquet. Dependence of MHD turbulence spectra on the velocity field-magnetic field correlation. *Astron. Astrophys.*, 126:51–58, 1983.

[Gog06] G. Gogoberidze. On the nature of incompressible magnetohydrodynamic turbulence. *ArXiv Astrophysics e-prints*, astro-ph/0611894, 2006.

[HB06] N. E. L. Haugen and A. Brandenburg. Hydrodynamic and hydromagnetic energy spectra from large eddy simulations. *Phys. Fluids*, 18:5106, 2006.

[HBD03] N. E. L. Haugen, A. Brandenburg, and W. Dobler. Is nonhelical hydromagnetic turbulence peaked at small scales? *Astrophys. J.*, 597:L141–L144, 2003.

[HDF] http://hdf.ncsa.uiuc.edu/HDF5/.

[Iro64] P. S. Iroshnikov. Turbulence of a Conducting Fluid in a Strong Magnetic Field. *Sov. Astron.*, 7:566, 1964.

[KH00] R. M. Kerr and J. R. Herring. Prandtl number dependence of Nusselt number in direct numerical simulations. *J. Fluid Mech.*, 419:325–344, 2000.

[KIY03] Y. Kaneda, T. Ishihara, M. Yokokawa, K. Itakura, and A. Uno. Energy dissipation rate and energy spectrum in high resolution direct

numerical simulations of turbulence in a periodic box. *Phys. Fluids*, 15:L21–L24, 2003.

[KM80] R. H. Kraichnan and D. Montgomery. Two-dimensional turbulence. *Reports of Progress in Physics*, 43:547–619, 1980.

[Kra59] R. H. Kraichnan. The structure of isotropic turbulence at very high Reynolds numbers. *J. Fluid Mech.*, 5:497–543, 1959.

[Kra62] R. H. Kraichnan. Turbulent Thermal Convection at Arbitrary Prandtl Number. *Phys. Fluids*, 5:1374–1389, 1962.

[Kra65] R. H. Kraichnan. Inertial-Range Spectrum of Hydromagnetic Turbulence. *Phys. Fluids*, 8:1385–1387, 1965.

[Les97] M. Lesieur. *Turbulence in fluids*. Kluwer Academic Publishers, Dordrecht, The Netherlands, 1997.

[LF92] V. S. L'vov and G. E. Falkovich. Conservation laws and two-flux spectra of hydrodynamic convective turbulence. *Phys. D*, 57:85–95, 1992.

[LG03] Y. Lithwick and P. Goldreich. Imbalanced Weak Magnetohydrodynamic Turbulence. *Astrophys. J.*, 582:1220–1240, 2003.

[LGS07] Y. Lithwick, P. Goldreich, and S. Sridhar. Imbalanced Strong MHD Turbulence. *Astrophys. J.*, 655:269–274, 2007.

[Lvo91] V. S. L'vov. Spectra of velocity and temperature fluctuations with constant entropy flux of fully developed free-convective turbulence. *Phys. Rev. Lett.*, 67:687–690, 1991.

[MAP05] P. Mininni, A. Alexakis, and A. Pouquet. Shell-to-shell energy transfer in magnetohydrodynamics. II. Kinematic dynamo. *Phys. Rev. E*, 72:046302, 2005.

[MB00] W.-C. Müller and D. Biskamp. Scaling Properties of Three-Dimensional Magnetohydrodynamic Turbulence. *Phys. Rev. Lett.*, 84:475–478, 2000.

[Mes99] L. Mestel. *Stellar magnetism*. Clarendon Press, Oxford, US, 1999.

[MG01] J. Maron and P. Goldreich. Simulations of incompressible magnetohydrodynamic turbulence. *Astrophys. J.*, 554:1175–1196, 2001.

[MG05] W.-C. Müller and R. Grappin. Spectral energy dynamics in magnetohydrodynamic turbulence. *Phys. Rev. Lett.*, 95:114502, 2005.

[Mof78] H. K. Moffatt. *Magnetic field generation in electrically conducting fluids*. Cambridge University Press, Cambridge, UK, 1978.

[MP89] M. Meneguzzi and A. Pouquet. Turbulent dynamos driven by convection. *J. Fluid Mech.*, 205:297–318, 1989.

[MPIa] http://www.mpi-forum.org/docs/mpi-20-html/mpi2-report.html.

[MPIb] http://www-new.mcs.anl.gov/mpi/.

[MTM04] T. Mashiko, Y. Tsuji, T. Mizuno, and M. Sano. Instantaneous measurement of velocity fields in developed thermal turbulence in mercury. *Phys. Rev. E*, 69:036306, 2004.

[MW98] B. Martin and X. L. Wu. Double-diffusive convection in freely suspended soap films. *Phys. Rev. Lett.*, 80:1892–1895, 1998.

[MY75] A. S. Monin and A. M. Yaglom. *Statistical fluid mechanics.* The MIT Press, Cambridge, US, 1975.

[Obu59] A. M. Obukhov. O vliyanii arkhimedovykh sil na struktury temperaturnogo polya v turbulentnom potoke. *Dokl. Akad. Nauk SSSR*, 125:1246–1248, 1959.

[Ors74] S. A. Orszag. *Fluid Dynamics: Les Houches 1973.* Gordon and Breach, New York, US, 1974.

[Pop00] S. B. Pope. *Turbulent flows.* Cambridge University Press, Cambridge, UK, 2000.

[Pou78] A. Pouquet. On two-dimensional magnetohydrodynamic turbulence. *J. Fluid Mech.*, 88:1–16, 1978.

[PP95] H. Politano and A. Pouquet. Model of intermittency in magnetohydrodynamic turbulence. *Phys. Rev. E*, 52:636–641, 1995.

[PPC98] H. Politano, A. Pouquet, and V. Carbone. Determination of anomalous exponents of structure functions in two-dimensional magnetohydrodynamic turbulence. *Europhys. Lett.*, 43:516–521, 1998.

[PW82] M. R. E. Proctor and N. O. Weiss. Magnetoconvection. *Rep. Prog. Phys.*, 45:1317–1379, 1982.

[Ray83] Lord Rayleigh. Investigations of the Character of the Equilibrium of an Incompressible Heavy Fluid of Variable Density. In *Proc. Lond. math. Soc.*, volume 14, pages 170–177, 1883.

[Ray16] Lord Rayleigh. On convective currents in a horizontal layer of fluid when the higher temperature is on the under side. *Phil. Mag.*, 32:529, 1916.

[RBC96] G. Ruiz-Chavarria, C. Baudet, and S. Ciliberto. Scaling laws and dissipation scale of a passive scalar in fully developed turbulence. *Phys. D*, 99:369–380, 1996.

[Sig94] E. D. Siggia. High Rayleigh number convection. *Annu. Rev. Fluid Mech.*, 26:137–168, 1994.

[SL94] Z.-S. She and E. Leveque. Universal scaling laws in fully developed turbulence. *Phys. Rev. Lett.*, 72:336–339, 1994.

[SV06] M. Schüssler and A. Vögler. Magnetoconvection in a Sunspot Umbra. *Astrophys. J.*, 641:L73–L76, 2006.

[SX01] X.-D. Shang and K.-Q. Xia. Scaling of the velocity power spectra in turbulent thermal convection. *Phys. Rev. E*, 64:065301, 2001.

[TI00] S. Toh and M. Iima. Dynamical aspect of entropy transfer in free convection turbulence. *Phys. Rev. E*, 61:2626–2639, 2000.

[TS94] S. Toh and E. Suzuki. Entropy cascade and energy inverse transfer in two-dimensional convective turbulence. *Phys. Rev. Lett.*, 73:1501–1504, 1994.

[VC99] R. Verzicco and R. Camussi. Prandtl number effects in convective turbulence. *J. Fluid Mech.*, 383:55–73, 1999.

[VC03] R. Verzicco and R. Camussi. Numerical experiments on strongly turbulent thermal convection in a slender cylindrical cell. *J. Fluid Mech.*, 477:19–49, 2003.

[VY99] A. P. Vincent and D. A. Yuen. Plumes and waves in two-dimensional turbulent thermal convection. *Phys. Rev. E*, 60:2957–2963, 1999.

[VY00] A. P. Vincent and D. A. Yuen. Transition to turbulent thermal convection beyond Ra = 10^{10} detected in numerical simulations. *Phys. Rev. E*, 61:5241–5246, 2000.

[War00] Z. Warhaft. Passive scalars in turbulent flows. *Annu. Rev. Fluid Mech.*, 32:203–240, 2000.

[Zel57] Ya. B. Zeldovich. The Magnetic Field in the Two-dimensional Motion of a Conducting Turbulent Liquid. *Sov. Phys. JETP*, 4:460–462, 1957.

[ZW02] J. Zhang and X. L. Wu. Thermal convection in two-dimensional soap films. In *Sixth Microgravity Fluid Physics and Transport Phenomena Conference: Exposition Topical Areas 1-6, vol. 2*, pages 585–586, 2002.

Acknowledgments

I would like to thank Prof. Dr. S. Günter for supervising my thesis and for the possibility to submit the thesis at the Technical University of Munich. Special thanks to Dr. Wolf-Christian Müller for inviting me to Garching and for giving me the opportunity to become a member of the Max-Planck Junior Research Group "Computational Studies of Turbulence in Magnetized Plasmas". Thanks to him for the exceptional long-term guidance, the invaluable everyday support throughout my work and for answering my numerous questions. Also, I would like to thank all other members of our group, particularly Dr. Yuriy Zaliznyak for many useful discussions. I am deeply indebted to Dr. D. Biskamp for his suggestions and illuminative answers. I would like to acknowledge the stimulating environment of the Garching Campus with all its institutes. Also, I express my gratitude to the Max-Planck Society for opening the program of Junior Research Groups through which I was financially supported during my work. Last but not least, I would like to thank Prof. P. Kulhánek who motivated me to study physics and showed me its beauty.